THREE DIMENSIONAL DSMC MODELLING OF THE DYNAMICS OF IO'S ATMOSPHERE

Building a simulation setup for parameter studies of the effects and the interaction of different processes in Io's atmosphere

Inaugural dissertation
of the Faculty of Science,
University of Bern

Presented by

Lea Meera Klaiber
Heidenheim, Germany

Supervisor of the doctoral thesis:

Prof. Dr. Nicolas Thomas
Physics Institute

COPYRIGHT NOTICE

THREE DIMENSIONAL DSMC MODELLING OF THE DYNAMICS OF IO'S ATMOSPHERE

Building a simulation setup for parameter studies of the effects and the interaction of different processes in Io's atmosphere

Inaugural dissertation
of the Faculty of Science,
University of Bern

Presented by

Lea Meera Klaiber
Heidenheim, Germany

Supervisor of the doctoral thesis:

Prof. Dr. Nicolas Thomas
Physics Institute

Accepted by the Faculty of Science.

Bern, 27.02.2024

The Dean
Prof. Dr. Marco Herwegh

A scientist in his laboratory is not a mere technician,
he is also a child confronting natural phenomena that impress him as
though they were fairy tales.

— Marie Curie

ABSTRACT

This thesis deals with the construction of a simulation model of the atmosphere of Io and the testing of different atmospheric processes added to the model. A 3D Direct Simulation Monte Carlo method is applied to model the rarefied gas flows. Different processes such as the surface frost sublimation, volcanic surface features and plasma heating are implemented in the model and further studied.

In its final version, the model can compute the sublimation of SO_2 depending on the solar incidence angle and a surface frost distribution, the outburst of volcanic plumes, the influence of plasma heating on both, the ambient atmosphere and volcanic plumes and the presence of several species. With this model a closer look at the plume structure and at the influence of different plasma parameters is possible. It was found that volcanic plumes in combination with a sublimation surface create hot non-equilibrium regions at their sides and winds of up to $300\mathrm{m/s}$ have been determined. Further, the parameters of the plasma interaction are studied and compared regarding to their influence on the temperature distribution of the atmosphere.

In a second step dust particles are added to the model using the DRAG3D code originally developed for cometary research. The movement of the dust particles is calculated from the gas flow field result. In this process various dust sizes and properties are explored and synthetic images of the dust density and the reflectance are created and analysed.

In future this model can be further refined by adding different species and physical processes.

ACKNOWLEDGMENTS

CONTENTS

LIST OF FIGURES

LIST OF TABLES

ACRONYMS

DSMC Direct Simulation Monte Carlo

VHS Variable Hard Sphere

VSS Variable Soft Sphere

IPT Io Plasma Torus

ultraSPARTS ultra-fast Statistical Particle Simulation Package

TAS Transient adaptive sub-cell scheme

VTS Variable time-step scheme

VDF Velocity distribution function

NIMS the near-infrared mapping spectrometer on Galileo

HST Hubble Space Telescope

FOS Faint Object Spectrograph

GHRS Goddard High Resolution Spectrograph

IRAM Institut de Radio Astronomie Millimétrique

STIS Space Telescope Imaging Spectrograph

ALMA Atacama Large Millimeter/Submillitmeter Array

Part I

INTRODUCTION

INTRODUCTION

Io, Jupiter's innermost Galilean moon, is the most volcanically active body in the solar system and presents a fascinating environment for the study of the interaction between extreme volcanic activity and dynamic atmospheric processes. This thesis aims to construct a model of the atmosphere of Io, exploring the interaction between atmospheric processes and the resulting dynamics. In combination with future observations this research intends to support the understanding of Io's atmosphere, its behaviour and interaction with surface processes and Jupiter's magnetosphere.

1.1 LITERATURE REVIEW

Io's atmosphere has always been a subject of debate. It appears to be primarily composed of SO_2 ([69]) which is also one of the gases driving the moon's intense volcanic activity. However, it is not clear whether the volcanoes or a condensation-sublimation cycle of SO_2 is the main source of the atmospheric gas.

The first evidence of an atmosphere on Io was obtained in 1973 with the detection of ionospheric layers above Io's surface ([38]), though discussions about the existence of an atmosphere were already present in the literature ([5],[18], [66], [14]). In 1979, the first evidence of volcanic activity was found in the analysis of Voyager 1 data ([69], [60]), although it was not certain whether the observed SO_2 originated from the volcanic plume or the ambient atmosphere. Further, millimeter-wave observations at 222GHz enabled the observation of Io's global SO_2 atmosphere ([43], [42]) which revealed surface pressures of about $4 - 40 nbar$ and column densities of $2 \times 10^{17} - 2 \times 10^{18} cm^{-2}$. In the last thirty years several observations and studies were made to gain further insights into the dynamics of Io's atmosphere.

1.1.1 *Atmospheric and surface observations*

The atmospheric column density has been studied globally and locally. In the following abstract different observations are discussed which assume that the local day side SO_2 vertical column abundance ranges between $\sim 5 \times 10^{15} cm^{-2}$ and 6×10^{17} cm^{-2} due to variations in the insolation, the surface frost distribution and volcanic activity. The estimates can be divided in into spatially unresolved, disk-integrated values and spatially resolved values. For disk-integrated data, models were used to deduce equatorial densities.

In 1992 Hubble Space Telescope (HST) obtained disk integrated observations using the Faint Object Spectrograph (FOS) which were interpreted as column densities of $6 - 10 \times 10^{15} cm^{-2}$ [3] and $4 \times 10^{16} cm^{-2}$ [11] for uniform atmospheric distributions. For a spatially confined atmospheric model at the subsolar point Ballester et al. fitted their data to densities of $10^{16} - 3 \times 10^{17} cm^{-2}$. Further, UV spectra by the Goddard High Resolution Spectrograph (GHRS) inferred disk-averaged column densities of $5 \times 10^{15} cm^{-2}$ and $7 \times 10^{15} cm^{-2}$ for the leading and trailing hemispheres respectively ([91]). Institut de Radio Astronomie Millimétrique (IRAM) radiotelescope disk-averaged observations at millimetre wavelengths were best fit with densities of $\sim 10^{17}$ cm^{-2} and temperatures $> 600K$ [42]. Also, the NASA Infrared Telescope disk-integrated mid-infrared spectra inferred equatorial densities of $1.5 \times 10^{17} cm^{-2}$ near $180°W$ and $1.5 \times 10^{16} cm^{-2}$ near $300°W$ [84]. On the other hand, 1996 saw the first successful spatially resolved observations of Io's atmosphere with HST/FOS [56]. They were able to show spatial inhomogeneity in column densities between three locations: Pele volcano, Ra volcano and a control region a $45°S$ and $300°W$ with column densities at $3.25 \times 10^{16} cm^{-2}$, $1.5 \times 10^{16} cm^{-2}$ and $7 \times 10^{15} cm^{-2}$ respectively. In 1998 the Galileo UV spectrometer could observe column abundances of $4 \times 10^{17} cm^{-2}$ covering $\sim 25\%$ of the observed region and local column abundances at $1 \times 10^{19} cm^{-2}$. These values however were quite uncertain due to marginal disk resolution, a spectral resolution which was inadequate to resolve the $10Å$ SO_2 absorption bands and values which depended on assumptions about the reflectivity of surface materials. Further, HST Space Telescope Imaging Spectrograph (STIS) observations at Lyman$-\alpha$ showed column densities of $\sim 10^{16}$ cm^{-2} ([75], [20]) which were further analysed by Feaga et al. [19]. Other HST/STIS mid- to near UV observations obtained

column densities of about $10^{16} - 10^{17} cm^{-2}$ with a peak near the equator of $1.25 \times 10^{17} cm^{-2}$ and $5 \times 10^{16} cm^{-2}$ near Prometheus [32]. These obtained column densities are consistent with vapour pressure equilibrium (where SO_2 gas is in thermodynamic equilibrium with SO_2 frost) with a peak temperature at 117K for latitudes $< 30°$ or solar zenith angles $< 40°$. However, beyond that the atmospheric column densities do not follow the vapour pressure equilibrium. Jessup et al. cites the enhancement of the dynamical flow, warm areas which inhibit condensation or SO_2 plumes as possible explanations for the divergence. The first disk-resolved millimetre observations with the IRAM Plateau de Bure Interferometer ([62]) revealed that the atmosphere covers $\sim 80\%$ of the leading side and $\sim 60\%$ of the trailing side. They also found limb-to-limb velocity differences of 330 ± 100 m/s which do not agree with models by Ingersoll et al. ([30], [29]) that predict uniform flow away from subsolar point for uniform frost coverage. Moullet hypothesized that it could be due to plume near limb or geographical variations in surface pressure due to either thermal inertia or inhomogeneous surface frost coverage. Observations performed with the NASA Infrared Telescope Facility on Mauna Kea from 2001, 2002 and 2004 obtained disk-averaged data from emission in the $SO_2 \nu_2$ vibrational band at 19.3µm [84]. The vertical atmosphere structure was modelled including the main production and loss mechanisms assuming non-LTE. Uncertainties in the interpretations were possible because of the dependence of the absorption strength on the vertical thermal structure. The best fit was found for an atmosphere with modified latitudinal dependence with inferred column densities at $1.5 \times 10^{17} cm^{-2}$ at $180°W$ and $1.5 \times 10^{16} cm^{-2}$ at $300°W$. Feaga et al. [19] reinterpreted the HST Lyman-α spectroscopic data and was able to indicate information about the spatial extent and column density of the SO_2 atmosphere. The vertical column densities derived had very low temporal variation, except for certain locations, typically in close proximity to established volcanic centres. Additionally, a globally smoothed SO_2 distribution map was generated which illustrates the imbalance in the SO_2 distribution between the sub-Jovian and anti-Jovian hemispheres as seen in figure 1. The highest column density was found in the anti-Jovian hemisphere at $5 \times 10^{16} cm^{-2}$. At high latitudes above $45°$ the measurements indicated low SO_2 column densities at around $1 \times 10^{14} cm^{-2}$.
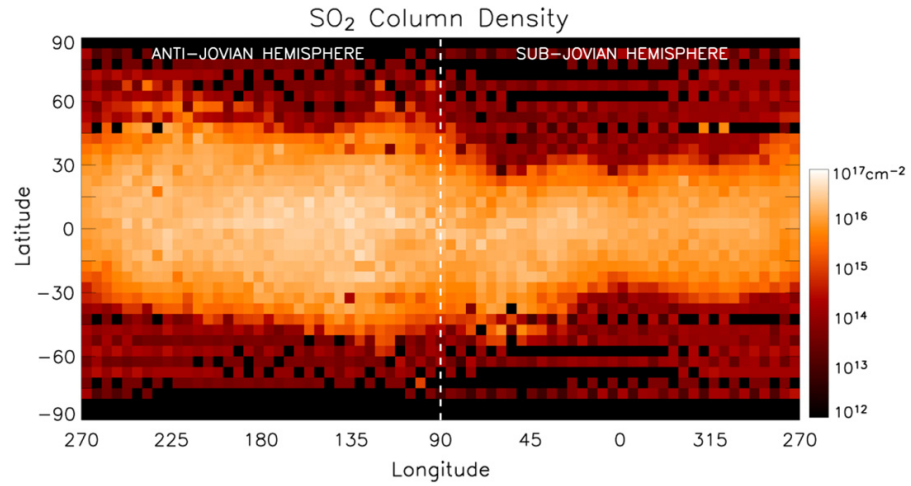
Figure 1: Io's average daytime column density distribution from a set of Lyman-α observations by [19].

SO$_2$ frost abundance maps were also created by McEwen et al. ([54]) based on Voyager multispectral mosaics, by Carlson et al. ([10]) with data from the near-infrared mapping spectrometer on Galileo (NIMS), by Douté et al. ([17]) with hyperspectral data cubes from Galileo NIMS as seen in figure 2 and others ([63], [65], [28], [77], [23])
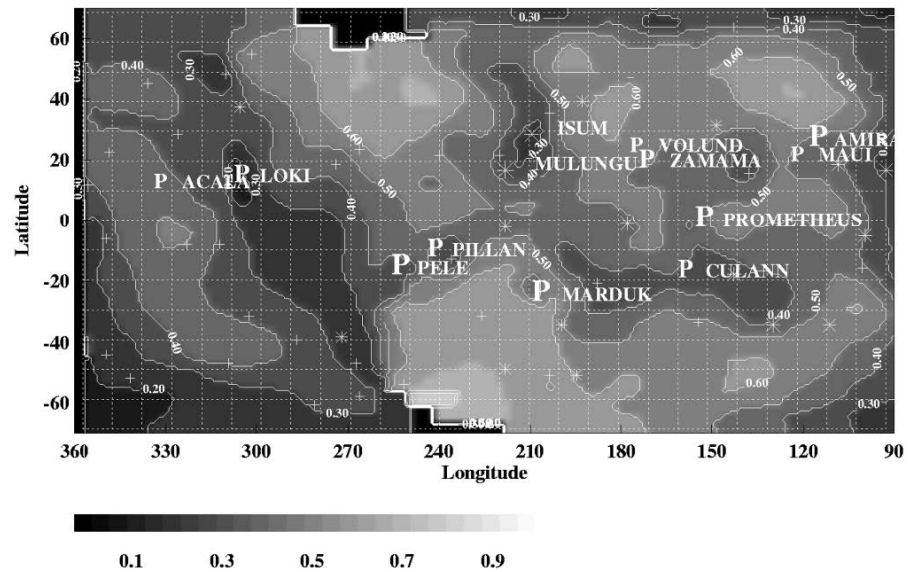
Figure 2: The SO$_2$ frost coverage in a global mosaic of Io based on the analysis of NIMS hyperspectral images by Doute et al. [17].

More recently Laver and de Pater ([41], [40]) mapped SO$_2$ abundances finding closer correlation with maps by McEwen et al. ([54]) than with data by Douté et al. ([17]). Further, maps

of the SO_2 abundance have been constructed by de Pater et al. ([68]).

1.1.2 *Volcanic observations*

The extreme volcanism on Io which is driven by tidal dissipation makes it unique in the solar system. The first observations of the large SO_2 plumes which are distributed over the entire surface of Io were made by Voyager ([83]) and the umbrella like shape of the plumes was first suggested to result from a large canopy shock by Strom and Schneider in 1982 ([73]). Further, McEwen and Soderblom ([55]) divided plumes into larger Pele-type plumes which would erupt over days and smaller Prometheus-type plumes which remain active for much longer periods of time. They also suggested Pele-type plumes to be produced by eruptions of sulphurous gas and Prometheus-type plumes by lava flows impinging on the surface frost. This theory was later also supported in studies by Spencer et al. ([85]) and Jessup et al. ([33]). Also, several plume source observations have been done. Tvashtar has been found to erupt from a thin fissure ([57], Prometheus is assumed to be formed by slow lava flow subliming surface frost ([16]) and Pele is suggested to be sourced by a lava lake([53], [15], [74]). Particle size distributions in plumes were constrained by studies of scattered or absorbed light. From Galileo observations it was found that small Prometheus-type plumes can contain $\sim 10^6$kg of 100nm particles ([24]). The same study showed in comparison to Voyager data of Pele, that particles in those plumes are smaller than in Prometheus-type plumes. However, later Hubble observations at 0.24μm and 0.42μm lead to the assumption of mean particles sizes between $50 - 110$nm at Pele ([31]).

1.1.3 *Plasma Torus observations*

Jupiter has the largest and most powerful magnetosphere in the solar system. This magnetosphere is populated by heavy ions originating at Io which results in mass loss from Io's atmosphere. These ions, which mainly consist of O^+, S^+ and electrons, accumulate around Io's orbit and form the Io Plasma Torus (IPT). The material in the torus is accelerated to corotate with Jupiter and overtakes Io at a velocity of about 57km/s. Therefore, Io's atmosphere is in constant interaction with the

plasma flow. More detailed reviews of the torus can be found in Thomas et al. [89] and Saur et al. [80].

In 1973 Pioneer 10 detected Io's ionosphere with a peak day side electron density of about $6 \times 10^{10} \mathrm{m}^{-3}$ and first indications of an atmosphere - IPT interaction ([38]). Further, in 1979 Voyager 1 flew through the IPT and measured number densities of ions and electrons. Their UV spectra were also measured ([8], [9], [81], [96], [2]). It was discovered that the number density in the torus increased by six orders of magnitude between the outermost magnetopause ($\sim 47 R_J$) and closest approach ($\sim 5 R_J$) and indicated electron temperatures of about $10^5 \mathrm{K}$ in the torus. Further, the Galileo and Cassini spacecraft performed new measurements of the Jovian system, Io and the plasma torus and refined the knowledge about it. Galileo flybys have shown that Io does not have an intrinsic magnetic field ([37], [79].) Additionally, Galileo observations indicated an electron number density in the torus of about $3.6 \times 10^3 \mathrm{cm}^{-3}$ and an ion temperature of $\sim 1.2 \times 10^6 \mathrm{K}$ ([22]). But these are only nominal values which can vary on a large scale depending on the position relative to Io. In general the ion temperature in the IPT can reach temperatures of $\sim 100 eV$ and is maintained by a combination of processes including ionization of neutral particles, interaction with high-energy particles and wave-particle interactions. When crossing Io's orbit, the ion temperature can fluctuate. Near Io, the interaction with Io's atmosphere and volcanic ejecta can cause localized changes in temperature. The density of the ions in the torus is highest near Io and decreases with distance from Io, since Io is the primary source of the ions. The density is also influenced by centrifugal forces dues to Jupiter's rapid rotation, which causes the plasma to be more spread out and less dense at larger distances from Io. The electron density in the torus is closely related to the ion density, as the plasma strive to maintain charge neutrality. However, the electron temperature can be different from the ion temperature due to different heating and cooling mechanisms. As the ion density, the electron density is higher near Io and decreases with distance from Io.

1.1.4 *Computational Studies*

Despite the extensive previous work, it has not been possible to determine the dominant atmosphere production mechanism and to explain the immense mass loss of Io. The whole system is highly complex and one individual model is usually re-

stricted to a part of the system. One can address the volcanic input, the atmosphere, the IPT-atmosphere interaction, the atmosphere photo-chemistry, the mass loss to the neutral clouds and the IPT and the IPT mass and energy balance. However, a comprehensive generalised model of the system is still some way off. Here the atmospheric dynamics are addressed.

So far, different modelling approaches have been taken for this problem, starting with Ingersoll et al. ([30]). They vertically integrated the conservation equations and argued for a sublimation atmosphere. Assuming turbulent atmospheric flow, a minimal impact of planetary rotation and uniform frost coverage maintained by the surface being in instantaneous radiative equilibrium with solar radiation, they found pressure driven supersonic flows from warm subsolar regions to colder regions close to the terminator. Similar results were obtained in an atmospheric model by Moreno et al. ([61]). The first indication of the importance of plasma heating was made by Strobel et al. ([86]) in a model of the vertical structure of Io's atmosphere which compared the influence of solar, Joule heating and plasma heating effect and found Joule and plasma heating as the predominant heating processes of the upper atmosphere. Wong and Johnson ([100], [101]) also studied the effect of plasma heating and found it inflating the upper atmosphere. Further, in combination with studies by Wong and Smyth ([99]), they found SO_2 being the main atmospheric species and significant drops in the column density on the night side of Io with a ratio of $\sim 1/10^3$ to the subsolar point.

There have been many approaches modelling the plasma torus and its interaction with Io's atmosphere. The modelling methods of the Jovian magnetosphere can be divided in two concepts. On the one hand, it can be modelled by solving the magnetohydrodynamic (MHD) equations ([44], [12], [34]) or on the other by using an electrodynamic model ([78], [79], [80]). Further, modelling of the surface thermal distribution has been done by Kerton et al. ([36]) including processes as the latent heat sublimation and condensation, thermal inertia, internal heat flow and solid state green house effect. They found almost all processes having an effect of decreasing the surface temperature besides the internal heat flow (which was assumed to be zero for most simulations) and with thermal inertia having the largest effect of $\sim$ 14K. More sophisticated models of Io's rarefied atmosphere using particle models have also been performed applying particle based simulations. Monte Carlo cal-

culations have been done by Pospieszalska and Johnson ([71]) studying the effect of ion bombardment and the induced loss rate of Io's atmosphere. Austin and Goldstein ([1]) performed Direct Simulation Monte Carlo (DSMC) two dimensional axis-symmetric simulations of the circumplanetary flow on Io. Further, Moore et al. ([59]) presented DSMC simulations of the sublimation atmosphere and modelled vertical dynamics throughout eclipse. Their results showed, that non-condensable species significantly slow down the condensation process of SO_2 by the formation of a diffusion layer close to the surface. Also Walker et al. ([94], [93], [95]) presented three dimensional DSMC simulations of the sublimation atmosphere including a detailed thermal model to describe the surface temperature and density. Zhang et al. ([105], [106]) performed axis-symmetric plume simulations of Prometheus and Pele.

The interaction between atmosphere and volcanic plumes was first approached in a very simple way by Ingersoll [29] who added volcanic plumes as a constant mass flux to his simulations. Later Tsang et al. [92] performed a similar study with a constant volcanic feature added to a time varying sublimation surface. Also [95] and [59] added separately computed plumes to their atmospheric models. More detailed simulations of volcanic plumes regarding their source structure and composition were performed by McDoniel et al. ([49], [50], [51]) by applying three dimensional DSMC simulation of volcanic plumes in Io's atmosphere.

1.2   MOTIVATION

In this work a three-dimensional, basic but physically realistic model of Io's atmosphere is presented. It includes basic atmospheric features such as the sublimation surface, volcanic plumes and plasma heating. The goal is to create a model which makes it easy to vary the driving parameters, which can be run on a local machine, and is computationally efficient. The basic approach should support the understanding of the underlying physical processes in the atmosphere of Io. This will make it possible to build upon the basic model and gain a better understanding of the complexities and dynamics in the atmosphere. In combination with future observations this model is designed to help to constrain the interpretation of new data. Also further simulations of the interaction of different processes can help constrain the processes of mass loss from Io.

DIRECT SIMULATION MONTE CARLO

For the simulation of the gas flow field in the atmosphere of Io, the Direct Simulation Monte Carlo (DSMC) method is applied. DSMC was first introduced by G. A. Bird [6] and uses a stochastic, particle-based approach suitable for rarefied flows. It has been already used for different studies of Io's atmosphere (e.g. Zhang et al. [105], [106], Walker et al. [94], [93], [95] and McDoniel at al. [49], [50], [51]).

2.1 OVERVIEW OF FLOW REGIMES

The degree of rarefaction of a gas can be classified by the Knudsen number:

$$K_n = \frac{mfp}{L} \tag{1}$$

where mfp is the mean free path of a molecule between collisions and L is the characteristic length scale of the flow. If L is chosen as an overall dimension, as for example the radius of Io, the global Knudsen number for the complete flow is defined. Alternatively, if the characteristic length is considered as the size of a single simulation cell (see chapter 5) the local Knudsen number is defined and detailed information on the change of the Knudsen number in the complete flow can be obtained. Figure 3 illustrates the different flow regimes according to their Knudsen number range and the applicable range of various numerical model approaches.

Flows with high densities exhibit a small K_n value, often below 0.01, allowing the use of macroscopic models like the Euler or Navier-Stokes equations to describe the flow as a continuum. As density decreases, rarefaction increases, leading to larger K_n values. This transition moves the gas flow from the continuum to the slip-flow regime ($0.01 < K_n < 0.1$), and further to the transitional ($0.1 < K_n < 10$) and free-molecular flow regime ($K_n > 10$) as the distance between gas particles increases. Up to a Knudsen number of 0.1, the validity of the

Discrete particle or molecular model	Boltzmann Equation				Collisionless Boltzmann Equation
Continuum model	Euler EQS	Navier-Stokes Equations	Conservation equations do not form a closed set		
Local Knudsen number	0 ←	0.01	0.1	1	10	100	→ ∞
Flow regime	continuum flow	slip-flow	transition flow	free-molecular flow	
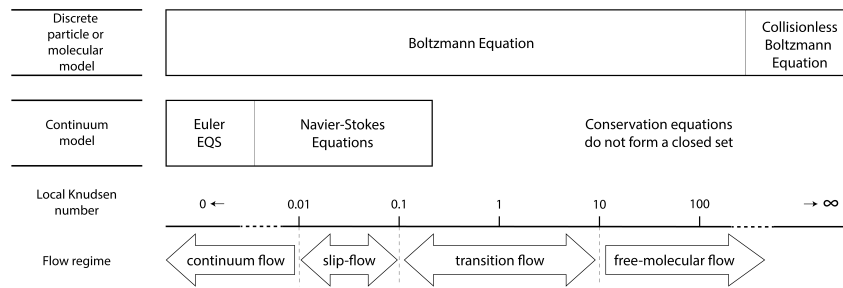
Figure 3: The different flow regimes according to their Knudsen number range and the applicability range of various numerical model approaches adapted from Bird [6] Chapter 1, Figure 1.1.

Navier-Stokes equations is maintained. However, for more rarefied gases, macroscopic fluid models are no longer valid and it is necessary to study inter-molecular interactions within the flow. The Boltzmann transport equation offers a statistical description of non-equilibrium flows, capturing the probabilistic changes in the states of gas molecules across space and time. It remains applicable across various flow regimes. Although analytic solutions to the Boltzmann equation exist in specific scenarios, they are typically not applicable to more complex cases. Consequently, numerical methods are employed to address the Boltzmann equation, with the DSMC method being one such approach.

On Io the flow densities and therefore the length scales of the gas flow can fluctuate widely. The mean free path can range from less than a meter close to volcanic plume sources to several meters at low altitudes in the day side atmosphere and up to tens or hundreds of kilometres at high altitudes or on the nightside of Io. In many cases the mean free path and the relevant physical length scale will be of the same order. However, while ranging within the transitional flow, continuum models will break down and a rarefied gas dynamics technique must be used. Therefore, the application of DSMC is advantageous since it is physically accurate in all flow regimes, although it can become computationally expensive at high densities.

2.2 3D DSMC - ULTRASPARTS

The DSMC method is employed for simulating rarefied gases and addressing the average properties of gas flows, in this case around 3D shapes of Io under specified boundary conditions. DSMC models the flow by computing the motion and collisions of particles for a number of timesteps Δt until the flow stabilizes and average values for the number density, temperature and velocity can be returned. In this study the ultra-fast Statistical Particle Simulation Package (ultraSPARTS) by the group of Jong-Shinn Wu ([102], [104], [103]) is used. It is a DSMC code in C++ which allows the simulation of 2D, 2D-axis-symmetric and 3D flows in unstructured grids. The code has been parallelized for execution on a multiprocessor cluster, aiming to decrease the computation time required for simulations. Further, within the ultraSPARTS package, several computational simplifications and methods are utilized to enhance the accuracy of the DSMC method while reducing computational time. Some of these strategies include:

1. **Statistical Weighting:** The statistical weighting can be defined as

$$W = \frac{number\,of\,real\,particles}{number\,of\,simulated\,particles} = \frac{N_{real}}{N_{sim}} \qquad (2)$$

   where the number of simulated particles represent a much larger number of real particles to allow for a faster sampling. Though, the number of simulated particles per cell should be large enough ($N_{sim} \sim 20 - 30$) to avoid statistical errors in the computations.

2. **Transient adaptive sub-cell scheme:** The Transient adaptive sub-cell scheme (TAS) divides the simulation cell into subregions to ensure nearest-neighbour collisions.

3. **Variable time-step scheme:** The Variable time-step scheme (VTS) enables cell size adapted time steps to minimize the required number of simulated particles for reduced statistical uncertainty and faster convergence to steady state. The aim is to keep the time step (Δt) as small as possible for enhanced accuracy in the DSMC simulation.

4. **Load balancing:** The dynamic load balancing technique should efficiently distribute the simulation calculations

across several cores. This method leverages the unstructured mesh topology to optimize the computational resource utilization.

Within the DSMC simulation, the state X of the gas at a time t is characterized by the coordinates and velocity vectors, represented as r_i and v_i, respectively, for a defined set of N simulation particles. The alteration of the gas flow state occurs through three stages within each simulation time step Δt.

1. **Collision less motion:** The particles are in free motion based on their velocity

$$r_i(t + \Delta t) = r_i(t) + \Delta t v_i(t) \tag{3}$$

This applies to particles without the influence of an external force field. In the simulations shown here the motion of the particles is calculated considering the effect of Io's gravity as well.

2. **Pair collisions:** Collision partners are randomly chosen from particles within the same cell, considering a collision probability. The collisions are then simulated using a designated collision model. Following the collision, the velocity vectors of the involved particles are updated with the velocity vectors of the particles post-collision.

3. **Interactions with simulation boundaries:** In addition to the pair collisions particles can also interact with the simulation boundaries. The inlet boundary provides the simulation domain with new particles and therefore acts as sublimation surface or volcanic inlet. The inlet density and temperature are an output of the thermal model and the initial velocity is set from a Half-Maxwellian velocity distribution function. The Code is able to apply a Cosine Law velocity distribution function which, however, has not been applied in this study (see appendix A). Particles which return to the surface condense back onto it and are excluded from the simulation. The outlet boundary can act as a vacuum boundary where particles passing through are deleted from the simulation or as another input boundary which inserts the plasma particles into the atmosphere.

The simulation concludes when the number of collisions has reached a stable state. The code outputs macroscopic flow properties, such as gas number density, velocity, and temperature

which result from averaging the present simulation particles within each cell. The obtained results are used either as input for subsequent dust dynamics simulations or for direct comparison. The DSMC simulation code accommodates the simulation of Io's atmosphere involving multiple gas species. In this study mainly SO_2 is used as the main species of Io's atmosphere and O_2 is used in some cases as a non-condensable background gas. In the case of a multi-species simulation, the code produces separate flow fields for each gas species and a combined flow field with the collective macroscopic properties of both gas species.

2.3 COLLISION MODEL

The ultraSPARTS code can be used by applying one of two collision models, the Variable Soft Sphere (VSS) or the Variable Hard Sphere (VHS) model, depending on the information given about the inserted species. In molecular gas dynamics both of the models are approaches used to describe the interactions between gas molecules (with molecule being a generic term referring to both, dia- or polyatomic molecules as well as single atoms) and the relationships between microscopic and macroscopic quantities. These models are particularly important in the context of kinetic theory and DSMC.

In general, a hard sphere model describes gas molecules as rigid spheres which interact only through instantaneous elastic collisions. These collisions are assumed to be perfectly elastic, meaning there is no energy loss during the collisions.The hard sphere model therefore simplifies the molecular interactions to the point where molecules are considered as non-deformable, non-interacting spheres with no attractive or repulsive forces between them. On the other side, a soft sphere model still represents gas molecules as spheres but the interaction potential is more complex, considering forces beyond simple elastic collisions. Here, intermolecular forces are introduced which affect the behaviour of the gas molecules. The molecular model chosen is therefore based on the definition of the forces included in the model. For real molecules the repulsive forces should be strongly dominant at short distances and weakly attractive forces should act at slightly larger distances as seen in Figure 4. Mostly, molecular models used for numerical simulations include some kind of approximation of these forces.
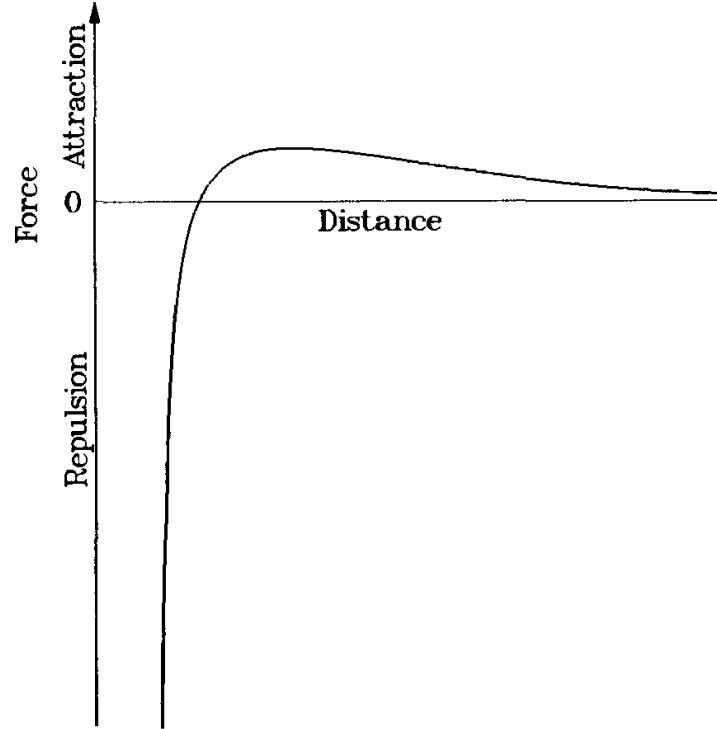
Figure 4: The typical intermolecular force field as a function of the distance adapted from Bird [6] Chapter 1, Figure 1.3.

2.3.1 *Hard Spheres*

In a simple hard sphere model the molecules are simulated as hard spheres, meaning the cross-section of the particles σ_T remains independent of the relative velocity between the colliding particles and can be expressed using the particle diameter ($\sigma_T = \pi \frac{1}{2}(d_1 + d2)$). Additionally, the scattering angle is isotropic in the center of mass frame of reference. This model offers the advantage that it is very simple. However, it is not very realistic. The viscosity and the self-diffusion coefficients of the model can be defined as:

$$\mu = \frac{5}{16}\sqrt{\frac{mk_BT}{\pi}}\frac{1}{d^2} \tag{4}$$

$$D_{11} = \frac{3}{8n\pi d^2}\sqrt{\frac{k_BT}{m}} \tag{5}$$

with m being the mass of the molecule, k_B the Boltzmann constant, T the temperature and n the number density. The only

free parameter of the model is the particle diameter which can be chosen to fit either the viscosity or the self-diffusion for a fixed temperature. Also, since the temperature dependence of $T^{1/2}$ does not correspond to general measurements the model is then not applicable to any other temperatures.

2.3.2 VHS

The Variable Hard Sphere model adds the dependence of the particle cross-section on the relative speed between colliding particles. Therefore, this model is characterized by two free parameters: the diameter of the molecules d_{ref} at a reference temperature T_{ref} and the exponent of the temperature in the viscosity power law ω.

$$\mu_{VHS} = \frac{15}{2(7-2\omega)(5-2\omega)} \frac{1}{d_{ref}^2} \sqrt{\frac{mk_B T_{ref}}{\pi}} (\frac{T}{T_{ref}})^\omega \qquad (6)$$

$$D_{11,VHS} = \frac{3}{2(5-2\omega)} \frac{1}{\rho d_{ref}^2} \sqrt{\frac{mk_B T_{ref}}{\pi}} (\frac{T}{T_{ref}})^\omega \qquad (7)$$

2.3.3 VSS

The Variable Soft Sphere model offers the same variability of the particle diameter as the VHS. Additionally, the deflection angle is reduced compared to the VHS model ([39]). This adds the exponent α of the cosine of the deflection angle to the calculation for the impact parameter ([6]). With the new parameter α it is possible to fit both, the viscosity and the self-diffusion. Also, for $\alpha = 1$ the VSS model returns the same results as the VHS model. In that way both models can be applied with the DSMC code. The viscosity and the self-diffusion coefficients of the VSS can be expressed as:

$$\mu_{VSS} = \frac{5(\alpha+1)(\alpha+2)}{4\alpha(7-2\omega)(5-2\omega)} \frac{1}{d_{ref}^2} \sqrt{\frac{mk_B T_{ref}}{\pi}} (\frac{T}{T_{ref}})^\omega \qquad (8)$$

$$Sc = \frac{\eta}{\rho D_{11,VSS}} = \frac{5(\alpha+2)}{3(7-2\omega)\alpha} \qquad (9)$$

with ρ being the density, Sc the Schmidt number and η the exponent of the inverse power law model which leads to the

power law temperature dependence of the coefficient of viscosity ($\omega = \frac{1}{2}\frac{\eta+3}{\eta-1}$) as seen for the VHS model.

For small molecules the VHS model offers a good enough solution with lower computational costs, though for large molecules (setting the boundary at a molecular weight of $50g/mol$) the VSS model should be considered. Also, the VHS model should be applied if the main interest is the viscosity force and the VSS model should be used for all flow properties. In the appendix A the values used to implement different species to the model using the VHS and VSS model are shown.

DRAG3D

For the simulation of the dust flow field in the volcanic plumes of Io the DRAG3D Code is used. This code has been originally developed for cometary research and has been applied to several studies of Comet 67P Churyumov-Gerasimenko (e.g. [48],[25]). Utilizing the gas flow field results from the DSMC simulation, it is possible to simulate the movement of dust particles. These are assumed to be spherical and can vary in size with the radius ranging from $10\,nm$ to $1\,m$. The predominant forces influencing the dust dynamics near the surface are the gas drag force and Io's gravity. The dust field is simulated by propagating test particles through the simulation domain and solving the equation of motion by applying a fourth-order Runge-Kutta method with an adaptive timestep. For the reduction of the computational expense, the dust dynamics for different dust sizes are calculated in parallel, neglecting dust-dust collisions. Particle tracking continues until particles either reach the outlet boundary of the simulation domain or are redeposited on the surface. The equation of motion for a single dust particle is

$$
\begin{aligned}
m_d \frac{d^2\vec{x}}{dt^2} &= \vec{F_G} + \vec{F_D} \\
&= m_d \vec{g_x} + \frac{1}{2}\sigma_d \sum_j C_j m_j n_j |\vec{v_j} - \vec{v_d}|(\vec{v_j} - \vec{v_d})
\end{aligned}
\tag{10}
$$

with the particle radius r_d, mass m_d, cross-section σ_d and the velocity $\vec{v_d}$. The gravitational acceleration is directly calculated from Io's mass and the position of the particle. The drag force j indicates the gas species, C is the local drag coefficient, m the mass of the species and n the local gas density. The local drag coefficient can be calculated analytically by applying the solution of the free-molecular flow limit ([13], [82]).

$$
C_j = \frac{2\xi^2 + 1}{\sqrt{\pi}\xi^3} e^{-\xi^2} + \frac{4\xi^4 + 4\xi^2 - 1}{2\xi^4} \mathrm{erf}(\xi) + \frac{2(1-\epsilon)\sqrt{\pi}}{3\xi}\sqrt{\frac{T_d}{T_j}}
\tag{11}
$$

with the dust temperatures T_d and gas temperatures T_j, the fraction of specular reflection ϵ and the dimensionless relative gas-dust velocity ξ.

$$\xi = \frac{|\vec{v_j} - \vec{v_d}|}{\sqrt{\frac{2k_B T_j}{m_j}}} \tag{12}$$

Further, the dust particles start the simulation with an initial velocity of zero. Only if the local drag force exceeds the local gravity the dust particle is lifted from the surface and its trajectory gets tracked. In this process the effect of inter particle cohesion is neglected. The equation of motion is then applied to the dust at any position within the simulation grid. The gravitational acceleration is uniform for all particles, regardless of mass or size. However, the drag acceleration for spherical particles with constant density is inversely proportional to the radius ($\sim 1/r_d$), diminishing for larger particles. Consequently, gravitational forces play a more significant role in the trajectories of larger particles, leading to observable returning trajectories in the results for larger dust size bins. Dust field properties in grid cells, such as dust number density or velocity, are derived from numerically weighting test particles to accurately represent the actual number of particles leaving a surface facet. Further, synthetic images can be created by combining a column density integration and light scattering effects by the present dust particles in the line of sight.

3.1 COLUMN DENSITY INTEGRATION

To generate synthetic images for direct comparison, the dust number density is integrated along lines of sight from the camera toward the surface. The position of the camera and the oberservation geometry can be selected before. Points beyond the grid outlet boundary are extrapolated using a $1/r^2$ law. This process is performed separately for each simulated size bin, yielding 40 partial images when using all of the dust size bins. In the final step, these partial images are combined to create the ultimate synthetic image encompassing all dust sizes. The calculated column density n_{col} for each size bin can be weighted based on a power-law particle size distribution function of the form:

$$n_{col}(r_d) \sim r_d^{-\beta} \tag{13}$$

where β is the power law index, a free parameter which can be adjusted in half-integer increments within the range $2.0 \leqslant \beta \leqslant 4.0$. Further, the particle size distribution influences the scattering behaviour of the particles and therefore the production of synthetic images of the reflectance.

3.2 IMAGE COMPOSITION AND SCATTERING MODEL

To obtain an image, the brightness, expressed in unitless reflectance values R, is computed for each partial image, assuming an optically thin atmosphere.

$$R = n_{col} \sigma_{geo} Q_{scat} \frac{p(\phi)}{4\pi} \qquad (14)$$

Here σ_{geo} is the geometric particle cross section and can be expressed as π_d^2. The scattering properties, including the scattering efficiency Q_{scat} and the phase function $p(\phi)$ as a function of the phase angle ϕ, are determined either by using the Mie theory [7] or by applying the Markkanen theory [47],[46]. In the concluding step, the partial images are merged to generate the overall synthetic image corresponding to a dust size distribution with a specific power-law exponent and dust-to-gas ratio. In general the model uses the OSIRIS WAC18 filter for the image composition which has a wavelength of 612.6nm and a bandwidth of 9.8nm [35].

3.3 SCATTERING MODELS

For the calculation of the scattering properties two different models can be used. In the first model the particles are assumed to be spherical particles and the Mie theory is applied to determine the scattering efficiency and phase function. While Mie theory is a very well studied method it has the disadvantage of only being valid for particles in a certain size range and assuming spherical particles. Therefore, the DRAG3D code includes the Markkanen model which can be applied to calculate the light scattering properties for large particles with a size of more than a few millimetre ([47], [46]). In contrast to Mie scattering model, the Markkanen model assumes more complex particles above a certain size. The transition between the two scattering models starts at a dust size of $r_d = 2 \times 10^{-4}$m.

Part II

SIMULATION SEQUENCE

In the following part the individual steps of the simulation sequence are presented and the different input values are explored.

MODELLING OVERVIEW

This chapter shall provide an introduction and a comprehensive overview and introduction of the simulation process and the steps necessary to simulate the gas and dust flow fields presented in this study. Mainly, the process can be divided into three steps:

1. The calculation of the gas flow field of the atmosphere of Io using the Direct Simulation Monte Carlo (DSMC) method.

2. The calculation of the dust flow field from the gas field results using the DRAG3D dust dynamics code.

3. The production of synthetic images from the dust field results by applying the properties of a defined bandpass of an optical system.

Here the third step is only applied to the study of volcanic plume cases. However, all steps include further sub-steps which will be discussed in the following chapters and are displayed in figure 5 which gives an overview of the whole simulation process. A similar process pipeline has been used and described in cometary studies by Marschall et al. ([48]) and Gerig et al. ([25]).

The simulated gas and dust flow fields should make it possible to gain a better understanding of the processes driving the atmosphere of Io and their interactions. The model parameters are therefore constrained by some of the studies and observations of Io which were discussed in chapter 1. The following chapters will take a closer look at these parameters and input values. In addition, the modelling approach relies on a few assumptions. Initially, the gas and dust flow domain are simulated in a domain with a restricted altitude. This incorporates the main physical processes. The number of free parameters in the model is also intentionally limited, aiming for a controlled simulation environment within a restricted parameter space. This choice facilitates a systematic exploration of individual parameters, preventing the emergence of ambiguous
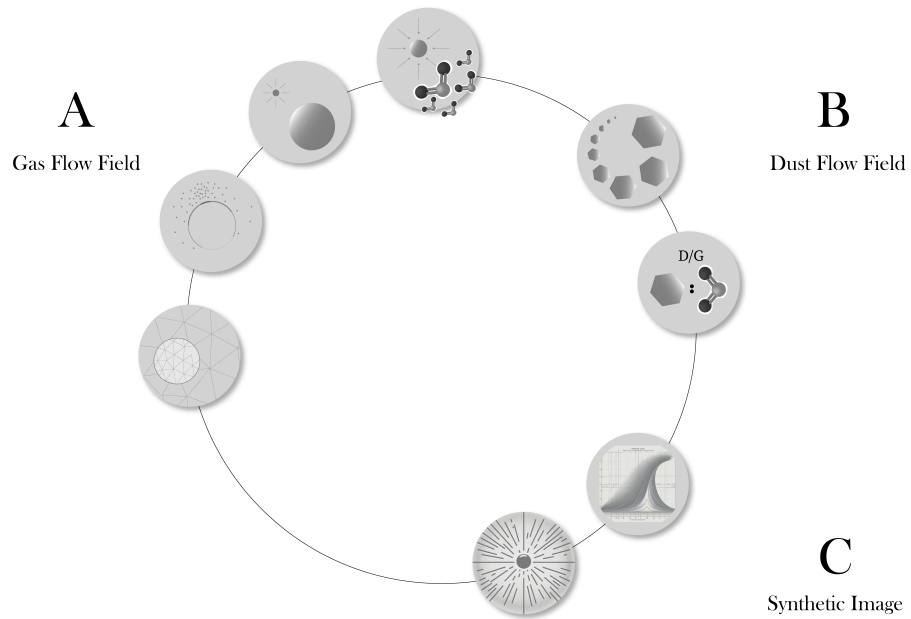
Figure 5: A schematic representation of the gas and dust simulation process. This two-step process involves the computation of the gas (A) and dust (B) flow field in 3D. The individual steps are elaborated upon in the subsequent chapters. In a third step (C), it is possible to produce synthetic images.

solutions often associated with overly intricate models. Excessive complexity can lead to under constrained models, impeding progress in comprehending the underlying physics. Consequently, the focus centres on the primary forces steering the gas and dust dynamics within the atmosphere of Io. Secondary processes and their effects are intentionally neglected to maintain model simplicity and clarity. These include processes such as the effects of dust on the gas flow field and photochemistry effects. However, these assumptions are analysed in more detail in chapter 8.

5

SIMULATION MESH

For the application of the DSMC method to a global model, a three dimensional mesh is required to sample particle movement and collisions within each cell and to extract the macroscopic atmospheric properties from sampling and averaging over all of the computational particles in one cell. Therefore, the mesh determines the resolution of the simulation and the results. For the creation of the different meshes the CFD (computational fluid dynamics) mesh generation software *Fidelity Pointwise* by *Cadence*[1] is utilised. Being the first step in the simulation process the mesh generation is a very crucial part, but since it is also quite time-consuming only a small number of meshes are used for different simulations.

Therefore, the simulation mesh defines some basic principles. First, a three dimensional shape model is used as the inlet surface of the mesh. This inlet surface is created by setting the shape model in the center of the coordinate system and projecting a mesh onto its surface. The shape model can be any three dimensional shape and for all of the applied meshes shown here the shape model of Io created from data by White et al. ([97]) shown in figure 6 has been used. Its topography ranges roughly between $-4km$ and $14km$ in elevation.

Further changes in the cell size control the mesh resolution which should be chosen according to the flux density of the simulation. The quality of the computation within a mesh can be determined by the ratio between the cell dimension (Δs) and the average distance travelled by a particle between collisions, which is the mean free path:

$$mfp = 1/(\sqrt{2}\pi n d^2) \tag{15}$$

Here $d = 7.16 \times 10^{-10}m$ is the effective diameter of SO_2 molecules and the figure of merit is such that

$$\frac{\Delta s}{mfp} \leqslant 1 \tag{16}$$

---

1 www.cadence.com
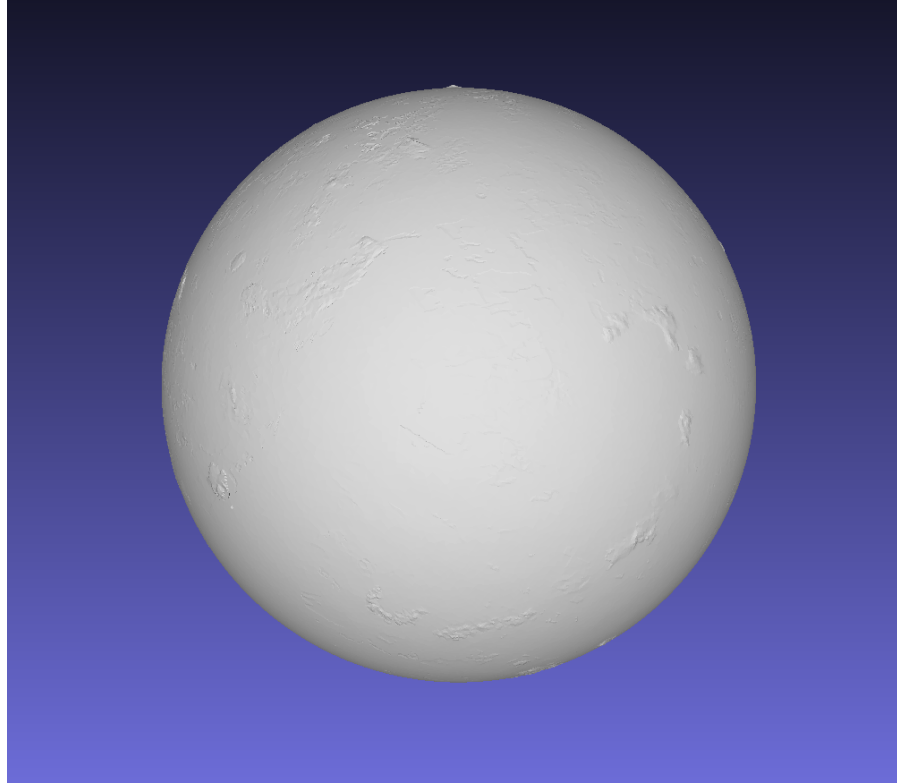
Figure 6: The shape model of Io used as the base for the mesh generation. It is based on the data by White et al. [97] and on surface texture data from global mosaics by the USGS Astrogeology Science Center. In a Cartesian coordinate system the z-axis goes through the north pole.

Since the mean free path depends on the local number density, it decreases with an increasing inlet flow but increases with a larger distance from the surface. Equation 16 states that the size of a simulation grid cell should be equal or smaller than the mean free path of a particle in this cell and if this condition is satisfied wherever the accuracy of the simulation is sufficient. In the case of high number densities at, for example, volcanic hotspots, the needed dimension of the cell can be very small, so that the total number of cells becomes very large which is expensive in terms of computational efficiency. However, the code uses the TAS technique described in chapter 2 to address this problem and previous studies with the applied DSMC code showed that the error of $\Delta s/\mathrm{mfp} > 40$ leads to a mean difference of the overall flow of 2% [21]. For the studies shown here a limit of $\Delta s/\mathrm{mfp} = 20$ was set based on the work of Pinzon et al. ([70]). Also, at higher altitudes, the mesh cells increase in size. This is possible because the flow densities decrease due

to the gas expansion into vacuum or a very low density background atmosphere. Consequently, the resolution of the mesh at the outlet boundary surface is much coarser than at the inlet surface.

The used meshes shown in the following section have been applied with different cell dimensions depending on the values of the inlet flow and the atmospheric processes which were simulated.

5.1 SPHERICAL SEGMENT MESH

For the testing of the volcanic plume model and local atmospheric processes two spherical segment meshes are used. The first one covers a surface area of about 450x450km and has an altitude of 450km. The second one, Spherical Segment Large (SSL), covers a surface area of 900x900km with an altitude of 450km. Both meshes include a circular inlet area in the middle of the inlet surface with a radius of 8km which serves as an inlet for a volcanic plume. Therefore, the inlet surfaces of the plume and the surrounding surface can vary in mesh resolution. Since the gas expansion for volcanic plumes is very fast and the densities can vary enormously between the inlet and the outlet surface, for the larger mesh a second smaller block was created within the simulation domain around the plume source inlet to gain a better control of the mesh distribution and increase the computational efficiency (see image 7). Table 1 shows the total number of cells of the mesh, the number of surface cells and the cell dimensions of the different meshes.

PARAMETER	SPH. SEGMENT	SSL
Total number of cells	10'640'974	12'679'540
Inlet surface cells	1'021'972	1'669'132
Δs inlet	50m − 1km	50m − 1km
Δs outlet	2km	10km

Table 1: Spherical Segment meshes and their properties.
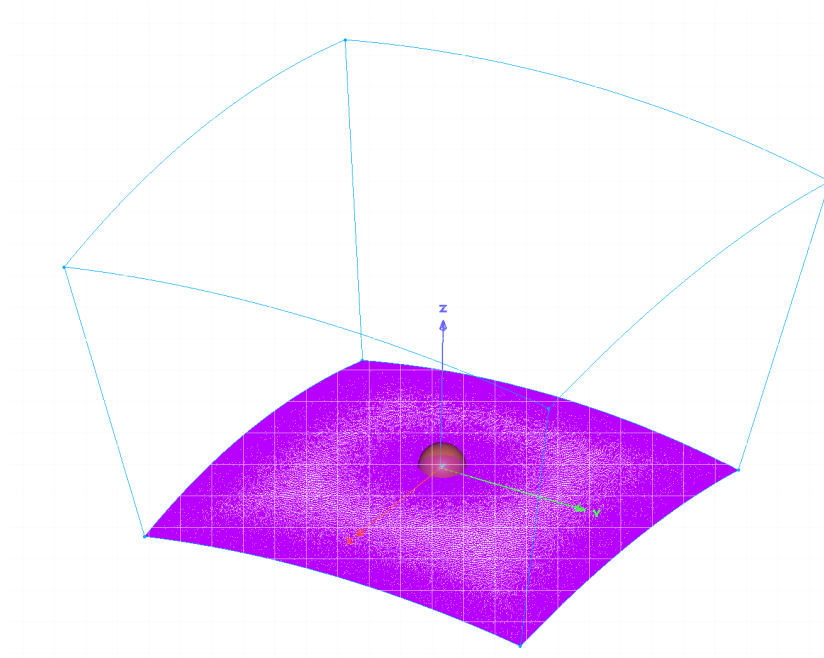
Figure 7: The Spherical Segment Large with an additional spherical block around the plume source inlet to increase the computational efficiency.

5.2   HALF SPHERICAL SHELL MESH

The main mesh used for the shown studies is the Half Spherical Shell (HSS) mesh. It covers half of the surface of Io and reaches an altitude of 250km. This mesh has been developed and integrated from sub-meshes with different resolutions, ranging from a lower resolution sub-mesh for studies of the night side of Io to a higher resolution sub-mesh for studies of the day side or interactions with volcanic plumes. Plume source inlet surfaces are added in the same way as before and consist of a circular shape with a 8km or 6km radius. They are placed at different spots on the surface, either in the middle of the mesh (around the z-axis) or at 45° respectively. This can be changed to support different plume distributions. Table 2 shows a summary of the properties of different Half Spherical Shell meshes and image 8 displays a 2D slice through a Half Spherical Shell mesh.

PARAMETER	HALF SPHERE	PLUME 45	2 PLUMES
Total number of cells	7'272'927	4'538'981	4'801'017
Inlet surface cells	1'183'474	704'214	750'442
Δs inlet	$1 - 10\text{km}$	$100\text{m} - 10\text{km}$	$100\text{m} - 10\text{km}$
Δs outlet	$10 - 100\text{km}$	50km	50km

Table 2: Half Spherical Shell meshes and their properties.
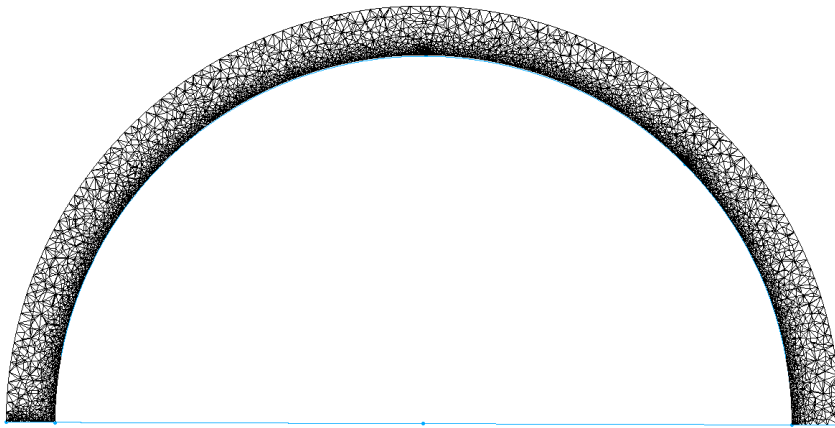
Figure 8: A 2D slice through the half spherical shell mesh showing the cell distribution. Noticeable is the high density of cells close to the surface and the wider cells close to the top of the simulated atmosphere.

6

THERMAL MODEL AND INLET BOUNDARY CONDITIONS

For the input of the inlet boundary surface, two options can be chosen. For a uniform distribution a general number density and temperature of the inlet surface can be chosen and is applied to every surface cell. This can be done for very simplified cases and local tests but also for the input of volcanic plume inlet surfaces. On the other hand a more detailed input can be applied by adjusting the input values for every single surface cell. In this case an illumination geometry is selected and the incidence angle of the solar insulation for every surface cell of the inlet boundary is calculated and a thermal model is used to determine the surface temperature, the local gas production rate and number density.

For the calculation of the surface insulation, the Sun is assumed to be a distant point source with a heliocentric distance of 5.2AU to Io and an average solar flux of $1384 Wm^{-2}$ at 1AU. The incidence angle θ_i can be defined as the angle formed between the incidence solar vector $\vec{v_\odot}$ and the vector normal to the surface $\vec{n}$. It is calculated for every surface cell:

$$\cos\theta_i = \frac{\vec{v_\odot}\vec{n}}{|\vec{v_\odot}||\vec{n}|} \tag{17}$$

At the position where the surface is perpendicular to the direction of solar insolation, the heat input and therefore the temperature is the highest and decreases with the cosine of the incidence angle. Further, for incidence angles of $\theta_i \geqslant 90°$ the surface is assumed to be not illuminated and a minimum temperature is set.

6.1 THERMAL MODEL

For the most simple case, a thermal model is applied to calculate the energy balance at each surface cell k of the inlet boundary, so that the temperature and gas emission rate for the sublimation inlet can be determined:

$$\frac{S_\odot(1-A_H)\cos\theta_i}{r_h^2} = \epsilon\sigma_s T_k^4 - L_{SO_2}\frac{dm_k}{dt} + \kappa\frac{dT_k}{dz} \tag{18}$$

The left side of the equation represents the solar energy input where $S_\odot$ denotes the solar constant at 1AU, A_H is the directional-hemispheric albedo, r_h the heliocentric distance in AU and θ_i the solar incidence angle. On the right side, the first term corresponds to the thermal radiated emission from the surface. Here the infrared emissivity ϵ is set at 0.8, σ_s is the Stefan-Boltzmann constant and T_k the surface temperature. The second term on the right side accounts for the energy loss through sublimation of ice per time unit. L_{SO_2} represents the latent heat of sublimation for the gas species and $\frac{dm_k}{dt}$ is the mass loss rate per second per unit area at the surface. Effectively, the mass loss rate can also be negative because of condensation back onto the surface. The third term reflects the influence of thermal conduction at the surface which depends on the thermal conductivity of the surface. In the results presented here a model is used which doesn't include the effect of thermal inertia (see chapter 8) and therefore this term has been neglected. The gas emission flux for particles with a mass m can be calculated by applying the Hertz-Knudsen equation under the assumption of thermodynamic equilibrium and when the back-flux of particles can be disregarded.

$$\frac{dm_k}{dt} = \frac{p_{vap}}{\sqrt{2\pi m k_B T_k}} \tag{19}$$

with the equilibrium vapour pressure p_{vap} and the Boltzmann constant k_B. The vapour pressure can be further calculated using an empirical version of the Clausius-Clapeyron equation ([90]):

$$\ln(p_{vap}) = A - \frac{B}{T} \tag{20}$$

The empirical constants A and B vary for different species. In this case for sulphur dioxide with $A = 30.3532$ and $B = 4510$. For oxygen O_2 another empirical version was applied and the empirical constants $A = 18.2725$, $B = -542.795$, $C = -7.44203$ and $D = 0.0144$ were obtained by fitting laboratory data of the vapour pressure ([76]). The empirical version used was:

$$\log(p_{vap}) = A + \frac{B}{T} + C\log(T) + DT \tag{21}$$

By adhering to flux conservation the gas production rate can be translated into a gas number density n at the surface following the expression:

$$\frac{dm_k}{dt} = \frac{1}{4}nmv \tag{22}$$

Assuming a half-Maxwellian velocity distribution at the surface the mean speed of the gas v can be determined as $\sqrt{\frac{8k_BT}{\pi m}}$. Due to the significant temperature dependence of the gas emission flux, even slight alterations in surface temperature can lead to substantial changes in the production rate. However, the majority of the energy is directed towards the sublimation of ice, and as the solar heat input increases, the surface temperature experiences only gradual changes. For surface cells with no solar insulation and an incidence angle $\theta_i \geqslant 90°$ the temperature is set to a nominal value of either 50K based on models by Ingersoll et al. ([30] or 90K based on models by Walker et al. ([93]).

6.2 INHOMOGENEOUS SURFACE MODEL

For a more detailed thermal model an inhomogeneous surface model has also been considered which is based on a SO_2 surface frost distribution map by Doute et al. ([17]) from IR emission data of Io's surface. Data of the frost coverage fraction and the albedo is given with degree resolution in both latitude and longitude. Between longitudes $0°W$ and about $60°W$ no data is available due to lacking observations of these regions. Also at polar latitudes data are missing and the reliability of existing data is rather low because of the highly oblique viewing angle. A map of the surface frost coverage can be seen in figure 9.

The data of the surface frost coverage goes into the calculation of the thermal model as a regulating factor of the gas production rate. For each surface inlet cell the calculated $\frac{dm_k}{dt}$ is multiplied with the surface frost fraction and thereby depends on the amount of frost available at the surface. For cells in regions with no data coverage the average coverage value of all available data (~ 0.433) is set. Since observations feature dark polar caps which indicate a lack of polar ice coverage ([58], [64]), for polar regions without data coverage an minimum coverage value of 0.1 is set.
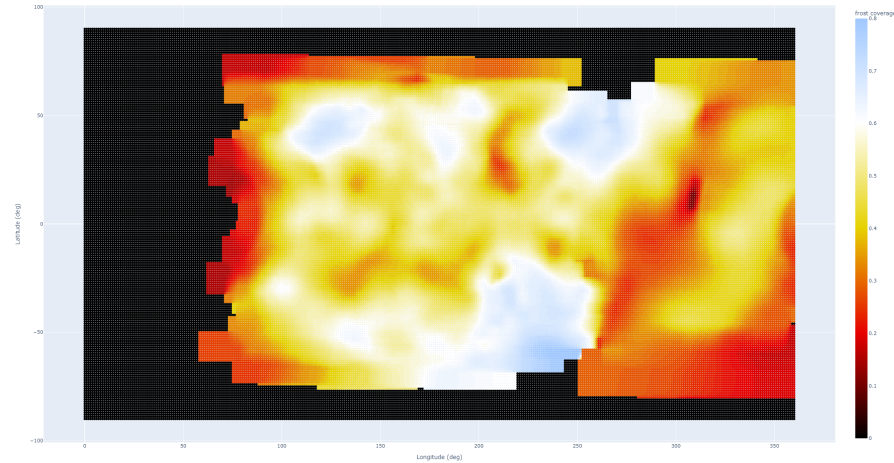
Figure 9: The surface frost coverage fraction from IR emission data by Doute et al. ([17]).

6.3   VOLCANIC ACTIVITY AND PLASMA HEATING

The input values for surface features such as volcanic plumes are set as uniformly distributed values over all cells of that feature. In that case values for the number density, the temperature and the flow velocity for different directions (radial or in Cartesian coordinates) can be set. For the volcanic plumes these values are set for every cell in a circular area on the surface of the mesh which is set as the source inlet surface of the plume. In most modelled cases, this is a circular area with a radius of 8km.

For the incoming plasma particles the outlet boundary surface, which in other cases is set as a vacuum outlet, can be adjusted as an inlet boundary surface with a negative velocity directing the particles into the simulation domain from the outlet. Therefore, the velocity of the particles can be set to either a negative Z-velocity or a negative or positive Y- or X-velocity, depending on which direction the particles should enter the simulation domain from. Additionally, also the number density and the temperature of the particles are set.

7

DSMC ULTRASPARTS INPUT

The DSMC code requires a certain number of input files. The first is the mesh file which is described in chapter 5 and forms the base of the simulation. As described in chapter 6 another input file is the thermal model which sets the input values for the inlet surfaces of the mesh. Additionally, the simulation needs three other files: the Input file, the Boundary file and the Species file. The Input file sets the general conditions of the simulation, such as the gravitational model (mass and center of gravity), the number of species used, the weighting and time step details and settings on the variable time step scheme. The Boundary file gives an overview of all boundary surfaces and sets their characteristics. So, they can be treated as inlet surface, vacuum outlet boundary or specular reflecting walls. It also sets whether an inlet boundary should be defined by a uniform temperature and density distribution or a thermal model. Further, the Species file contains detailed information on the species which is needed for the collision model. By adjusting these values it can also be determined which of the collision models is to be used, the VSS or the VHS (see chapter 2).

OMITTED EFFECTS OF POTENTIAL IMPORTANCE

8.1 GENERAL ASSUMPTIONS OF THE DSMC AND DRAG3D CODE

In general this study focusses on the main forces driving the gas and dust flow fields in the atmosphere of Io. However, assumptions and simplifications have been made which may influence the actual situation to some extent. They are catalogued here.

1. Effects of dust on the gas flow field: The dust flow field calculation assumes that the dust particles are lifted and accelerated by the gas flow. However, back-reactions of the dust on the gas through mass-loading are neglected. This assumption makes it possible to calculate the dynamics of the gas and dust flow fields separately which eliminates the need of a joined gas-dust interaction model. Models by Marschall et al. ([48]) show that the kinetic energy of the dust flow is two orders of magnitude lower than the kinetic energy of the gas, but this may not be the case here since some feedback on the gas flow from the dust may occur at a higher level.

2. Heating of the gas by the dust: The heating of the gas by collisions with the dust is not accounted for in this study. Tenishev et al. ([88]) show that this effect can be neglected in the case of cometary gas flows and that the back-coupling of the dust does not affect the gas flow field. However, the situation might be different for Io.

3. Rotation: For simplification the rotation of the moon is neglected and therefore only steady-state solutions of the gas and dust flow fields are considered. This assumption can be clearly justified for the gas flow field since the particles move with rather high velocities and therefore cross the simulation domain within seconds or minutes which is much smaller than the rotation period of Io (~ 42.459h). For the dust flow field it can also be justified for particles $< 300\mu m$ ([48]) with high velocities. For larger dust par-

ticles or slow moving particles it might be necessary to consider a time dependent model.

4. Dust-dust collisions: Since dust-dust collisions occur with low enough probability they can be neglected. Marschall et al. [48] found the mean free path of dust particles in various simulation set ups to be around 2000 m assuming the flows to be optically thin at the source. This simplification allows to calculate the dust dynamics for different dust sizes independently and in parallel which decreases the computation time significantly. However, for large eruptions with higher number densities and for higher dust-gas ratios this assumption should be viewed critically.

5. Species: For the study shown here, SO_2 is considered to be the primary gas. This can be justified for simple cases, since it is the dominant component of Io's day side atmosphere ([69]). However, for more detailed studies also other species as S, S_2 or SO need to be added to the model.

6. Velocity distribution function (VDF): For the gas flow field the VDF at the surface is set to be half Maxwellian. Other possibilities as the cosine law VDF have been tested but for the cases shown here a half-Maxwellian VDF is assumed. This can be justified for most cases, however in cases of fast gas expansion the resulting VDF might deviate from this assumption.

7. Condensation: Gas particles returning to the surface are viewed as condensating particles and are deleted from the simulation. However, it should be considered that the flow back to the surface reduces the total outflow below that. Further, energy is deposited through re-condensation. For a physically improved simulation these effects would need to be included within the boundary conditions.

8.2 PHOTOCHEMISTRY

Besides the mentioned simplifications, chemical reaction processes are also neglected. Photo-dissociation and -ionisation are not accounted for. In cometary studies ([27]) it has been shown that the scale lengths of these processes usually extend the size of the here used simulation domains and therefore only become crucial at distances beyond the reach of the simulation. This can

be compared to the thin atmosphere around Io. However, for the general neutral atmosphere of Io, photo-chemistry plays an important role ([87]) in the heating of the atmosphere and in the production of minor species that may have non-negligible local number densities. This should be considered in future studies.

Part III

RESULTS

GAS RESULTS

For a better overview of all gas result cases, they are listed in table 3 and 4 and each case is provided with an abbreviation.

9.1 UNIFORM SO_2 ATMOSPHERE $UniSO_2$

The simulation of the uniform SO_2 atmosphere is used to create the basic case for comparison. Therefore this chapter deals with the uniform gas sublimation of SO_2 from a half spherical and homogeneously distributed ice source. In the first part only the sublimation mechanism will be studied and in the second part plasma heating will be added. To assure stable results which accurately reflect the physical mechanisms the convergence is checked. Therefore, the change in particle number with the number of iterations (time steps) is reviewed in figure 10 for the most simple case. It shows that the simulation reaches convergence after ∼ 100000 time steps. All results shown here have been iterated at least this number of time steps.
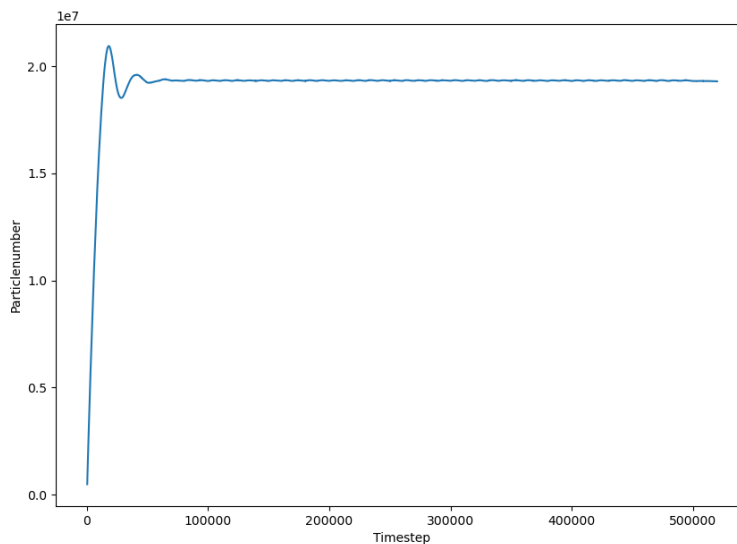
Figure 10: The particle number displayed over the number of time steps.

9.1.1 *No plasma impact*

First, the half spherical mesh with a radius of Io is used to simulate the outgassing of SO_2. A uniform sublimation case of the average dayside atmosphere is assumed which leads to input values of a number density of $1 \times 10^{15} m^{-3}$ and a surface temperature of 115K which corresponds to an incidence angle of $\sim 20°$. The outflow velocity of the sublimating particles is assumed by the thermal velocity $v_{th} = \sqrt{\frac{8k_B T}{m\pi}}$. Figure 11 shows a two dimensional slice through the mesh and displays the number density and temperature profiles. Further figure 12 shows the number density, temperature and velocity profiles plotted against the radius from the surface to the end of the simulation domain (which covers a range of $\sim 1820 - 2070 km$ which yields in an altitude of 250km) of a line profile in Z-direction.

(a)   (b)
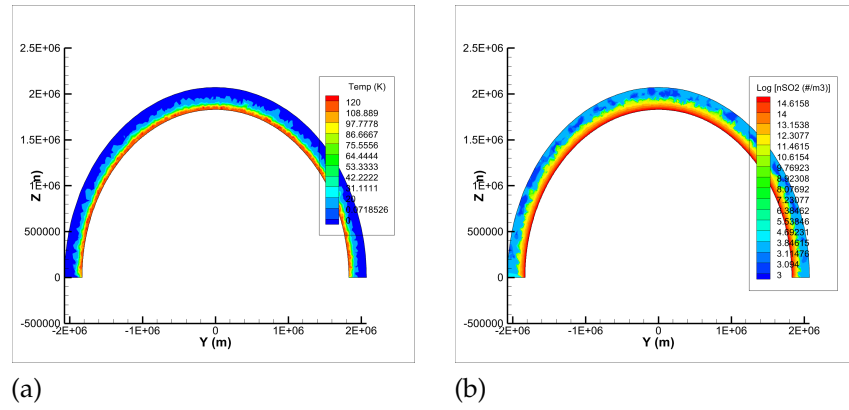
Figure 11: The temperature (a) and logarithmic number density (b) profiles of the uniform SO_2 sublimation, displayed in two dimensional slices through the 3D simulation domain.

From the figures it can be observed that in the case of pure sublimation the particles do not have enough energy to reach higher altitudes than $\sim 150 km$. Upon reaching the maximum height the number density as well as temperature and velocity drop to zero. This means the particle collisions and movement do not hold enough energy to reach higher altitudes. Especially, in the velocity profiles it is visible that the majority of the particles reach their peak velocity at $\sim 30 - 40 km$ and start to fall back shortly after. Also, the temperature drops very rapidly with increasing distance to the surface. It already reaches a temperature of $\sim 90 K$ at an altitude of 60km. Further, also the scale height $H = \kappa T/mg = 8.3 km$ and the computed scale height from a vertical profile through the simulation domain
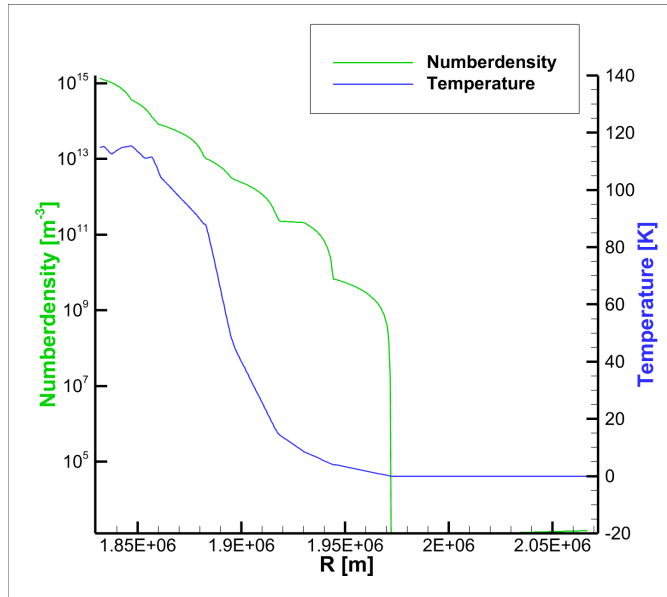
(a)
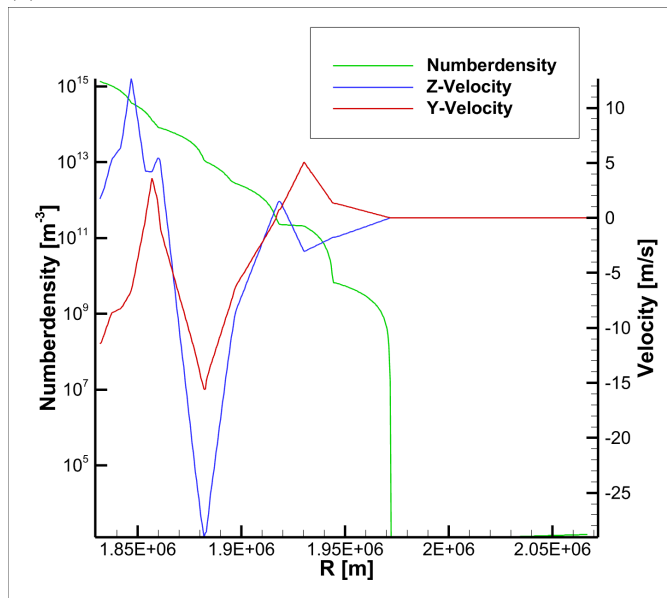
(b)

Figure 12: Line profiles of the number density, temperature (a) and velocities (b) in Z- and Y-direction of the uniform SO_2 sublimation of a profile in Z-direction.

of $H_{sim} = 9.8$km reach only lower altitudes. These height distribution can also be observed as various steps in the number density profile of figure 12a. Further steps of lower number densities appear at altitudes of 100km and 130km. However, observations of the radio signal ([38])strongly suggest that Io's atmosphere is more extended than it would be predicted by this very basic model. Hence, another energy supply must be

added to the system. Here heating of the atmosphere by plasma bombardment is assumed and covered in the next section.

9.1.2   *Plasma impact*

In a second step plasma particles are introduced from the simulation outlet with a velocity in negative Z-direction. The plasma particles are inserted as additional neutral SO_2 particles which provide energy to the atmosphere by colliding with the atmospheric particles. However, the input parameters of the plasma particles are hard to define and the knowledge of the energy deposition is extremely poor. The number density, temperature and velocity can vary on a large scale depending on the position in the atmosphere of Io and on electromagnetic interaction processes. Especially, since the simulation only covers the atmosphere flow close to the surface of Io the properties of the plasma particles approaching this atmosphere layer are likely to be different from the properties observed in the plasma torus. Here plasma densities of $1 \times 10^8 \mathrm{m}^{-3}, 3 \times 10^8 \mathrm{m}^{-3}, 4 \times 10^8 \mathrm{m}^{-3}, 5 \times 10^8 \mathrm{m}^{-3}, 1 \times 10^9 \mathrm{m}^{-3}$, velocities of 15km/s, 30km/s, 45km/s in negative Z-direction and a temperature of 150eV are studied. Table 5 shows the input values for the different cases and the energy deposited per cubic metre for SO_2 for each case.

Figure 13 shows two dimensional slices of the number density for a plasma particle density of $1 \times 10^8 \mathrm{m}^{-3}$ and several velocities and figure 14 displays the number density and temperature profiles of a line profile from the surface to the edge of the simulation domain in the Z-direction for the three different plasma particle input velocities with a plasma particle density of $1 \times 10^8 \mathrm{m}^{-3}$. For the first case $\mathrm{UniSO_2P1815015}$ with a velocity of 15km/s no indication of a heating effect is visible and in comparison to figure 11a the profile with plasma impact is barely distinguishable. In contrast, the third case $\mathrm{UniSO_2}$ P1815045 with a velocity of 45km/s shows the other extreme with a massive heating effect, reaching temperatures of the order of 10^5K. This does not seem realistic, however it has to be noted that the SO_2 particles assumed here have double to four times the mass of the main plasma ions which influences the energy provided to the atmosphere. The second case $\mathrm{UniSO_2P1815030}$ with a velocity of 30km/s is able to heat the atmosphere with peak temperatures of ~ 800K and is able to add enough energy to the atmosphere in order for the particles to reach higher altitudes with number densities of $1 \times$

10^{10} to $1 \times 10^{11}\mathrm{m}^{-3}$ at altitudes of 250km. When looking at the density profiles, both higher velocity cases are able to inflate the atmosphere and increase the densities in higher altitudes. Also when studying the exobase, which can be defined as the altitude where $n_{col} \times \sigma_{cross} = 1$ (with the column density n_{col} and the collision cross section σ_{cross}), both higher velocity cases increase the exobase to a height of ~ 30km. Here, the column density is calculated radially through the simulation domain. Figure 15 shows the varying number density and temperature along a profile in Z-direction for different densities of the plasma particles and a velocity of 15km/s. Again, the first case UniSO$_2$P1815015 of a minimal density of $1 \times 10^8\mathrm{m}^{-3}$ shows almost no effect and no difference to the pure sublimation case. On the other hand, the case UniSO$_2$P1915015 with a maximal density of $1 \times 10^9\mathrm{m}^{-3}$ already displays a large heating effect reaching very high temperatures at relatively low altitudes of ~ 80km from the surface.

However, it must be considered that the amount of plasma energy deposited in the atmosphere is assumed to only be 20% of the plasma flow energy due to corotation ([100], [45], [98]). This corresponds to a reduced velocity of ~ 25.5km/s at the torus mass flux assuming a relative velocity of 57km/s of the corotating plasma. Additionally, it should be regarded that in these cases only SO$_2$ is used whereas the Io Plasma Torus mainly consists of sulfur and oxygen ions and O$^+$ should be considered as the dominant species of the impacting plasma ([89]. This results in a difference in mass by a factor of 4 which in the case of SO$_2$ reduces the velocity to a value of ~ 13km/s. Therefore, the cases with a velocity of 15km/s can be assumed to be closer to the actual conditions of the inflowing plasma particles and the first case in figure 13 seems more realistic.

9.2 UniSO$_2$O$_2$

In addition to the surface sublimation of SO$_2$ this chapter covers the effect of inserted O$_2$. For the simulation O$_2$ is inserted as a background gas.

9.2.1 *No plasma impact*

In a first step the input of O$_2$ as a background gas is studied for a fully illuminated surface with uniform SO$_2$ outgassing as in the section before (with a SO$_2$ density of $1 \times 10^{15}\mathrm{m}^{-3}$ and a

(a)

(b)

(c)
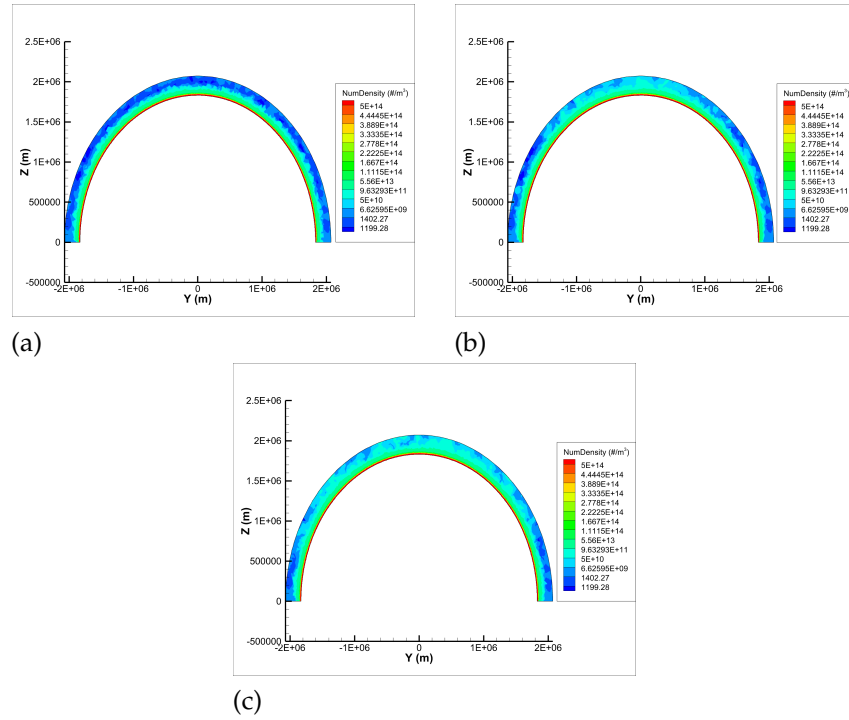
Figure 13: Two dimensional slices displaying the number density for varying input velocity of the plasma particles of $15km/s, 30km/s, 45km/s$ (from left to right) with a plasma particle number density of $10^8 m^{-3}$ and a temperature of $150eV$.

surface temperature of 115K). It is tested for three different O_2 densities of $2 \times 10^{10} m^{-3}, 2 \times 10^{12} m^{-3}, 2 \times 10^{15} m^{-3}$. The O_2 gas is inserted as a background gas which means that the particles are already distributed in the simulation domain and a certain number of O_2 particles are present in each cell. That is why it does not need to be sourced from the surface. Figure 16 shows the temperature and number density variation from the surface to the end of the sublimation domain in Z-direction for the previously stated density cases.

9.2.2 *Plasma impact*

In a second step the plasma particles are inserted with varying velocities of $15km/s$ and $30km/s$ for a case of day side SO_2 sublimation with a O_2 background gas density of $2 \times 10^{12} m^{-3}$. Figure 17 shows the 2D slices of the temperature of theses cases and figure 18 displays the number density and temperature along a radial profile through the simulation domain. The 2D slices show that the faster velocity (case $UniSO_2O_2212P3815030$)

Figure 14: Line plots displaying the number density and temperature profiles for varying input velocity of the plasma particles of 15km/s, 30km/s, 45km/s and with a plasma particle number density of 10^8m^{-3} and a temperature of 150eV for a profile in Z-Direction.

increases the amount of deposited energy and therefore increases the heating effect. In comparison to figure 14 the radial profiles show that the added O$_2$ increases the number density of the atmosphere and increases the heating effect of the incoming plasma particles. For the case with a plasma velocity of 30km/s (case UniSO$_2$O$_2$212P3815030) the atmosphere displays a temperature profile similar to case UniSO$_2$P1815045 with a plasma velocity of 45km/s. This means the added O$_2$ increases the heating effect at lower altitudes. Also, both cases with a plasma velocity of 15km/s show a significant change in the temperature and number density profiles when O$_2$ is added as a background gas.

In a further step cases of day and night side sublimation with background O$_2$ should be compared. Therefore, a SO$_2$ sublimation input with a number density of 1×10^{15}m^{-3} and a temperature of 115K is used for the day side and a sublimation input with a number density 1×10^{12}m^{-3} of and a temperature of 90K is used for the night side. In both cases the O$_2$ back-
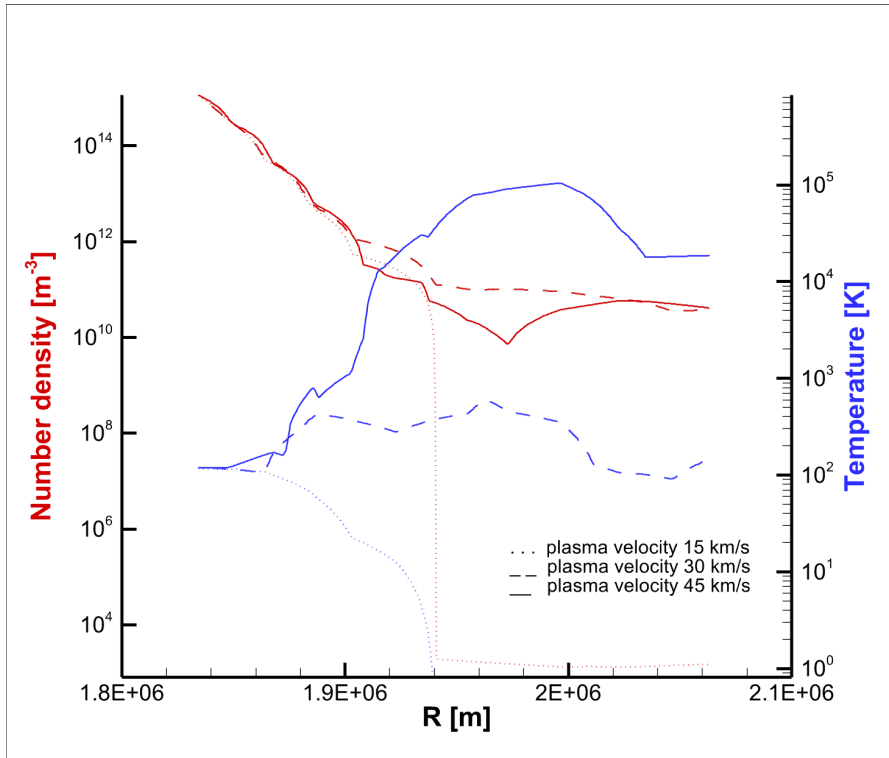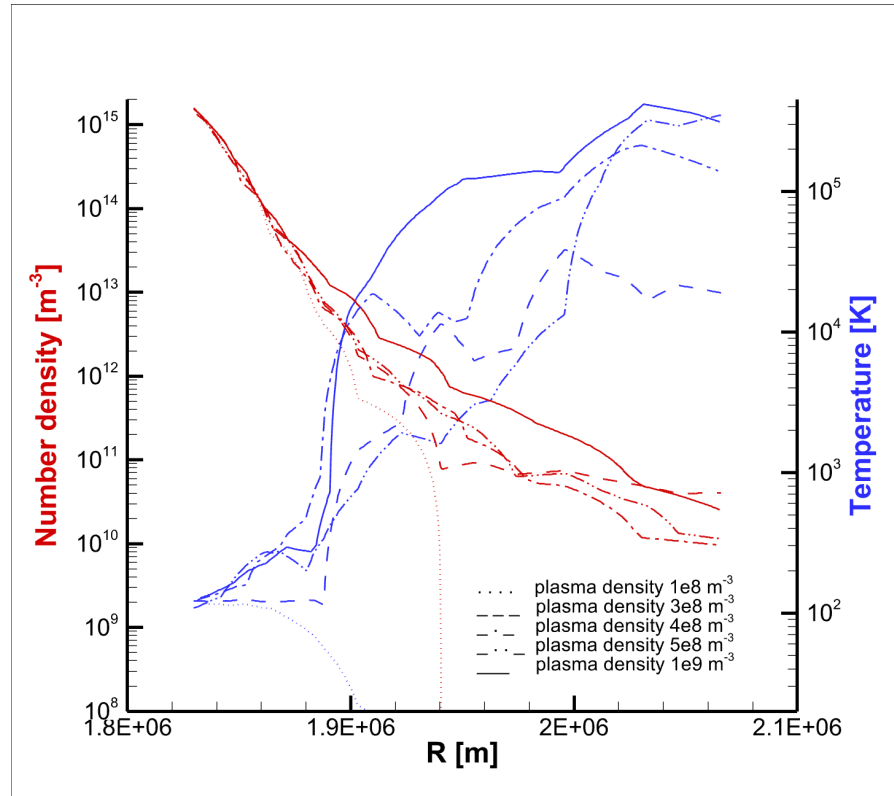
Figure 15: Line plots displaying the number density and temperature profiles for varying input densities of the plasma particles of $1 \times 10^8 m^{-3}, 3 \times 10^8 m^{-3}, 4 \times 10^8 m^{-3}, 5 \times 10^8 m^{-3}, 1 \times 10^9 m^{-3}$ with a plasma particle velocity of 15km/s and a temperature of 150eV for a profile in Z-Direction.

ground gas has a density of $2 \times 10^{15} m^{-3}$. Both cases contain inserted plasma particles at a density of $3 \times 10^8 m^{-3}$ and a velocity of 15km/s. Figure 19 shows the 2D slices of theses cases and figure 20 the line plots. It is clear from both, the 2D plots and the line plots, that the nightside is very rarefied and the plasma can reach the surface almost unimpeded. The temperature is only driven by the impacting plasma particles. For the dayside profile it can be observed that the heating and inflation effect is higher with a background O_2 gas than seen in case UniSO$_2$P3815015.

9.3   SSO$_2$

In addition, to the uniform sublimation case a more detailed sublimation based on the solar incidence angle and a surface frost distribution by Doute et al. ([17]) was tested. Figure 21 shows slices for the number density and temperature fields for
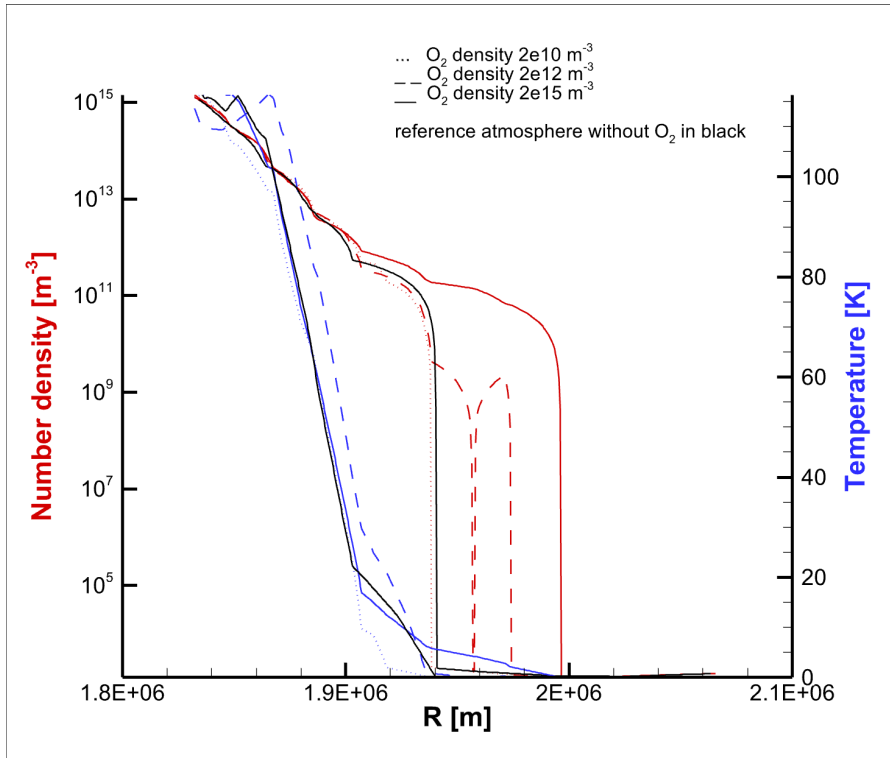
Figure 16: Line plots displaying the number density and temperature profiles for varying input densities of the O_2 as a background gas in a uniform sublimation atmosphere.

(a)

(b)
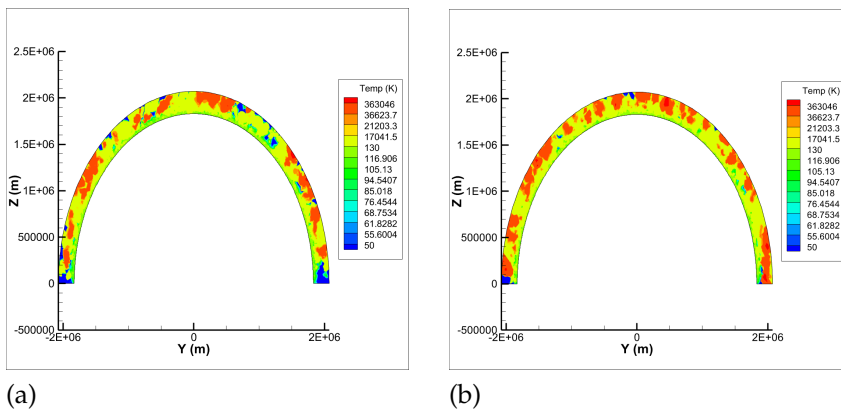
Figure 17: Two dimensional slices through the 3D simulation domain of the temperature field for a day side SO_2 sublimation with O_2 background gas for different plasma velocities of 15 km/s (a) and 30 km/s (b) with a plasma particle density of $3 \times 10^8 \mathrm{m}^{-3}$ and temperature of 150 eV.

a case with the sub solar point being at $X = Y = 0$ and figure 22 shows the same for a case with the sub solar point at $X = Z = 0$. However, due to the high complexity with varying input
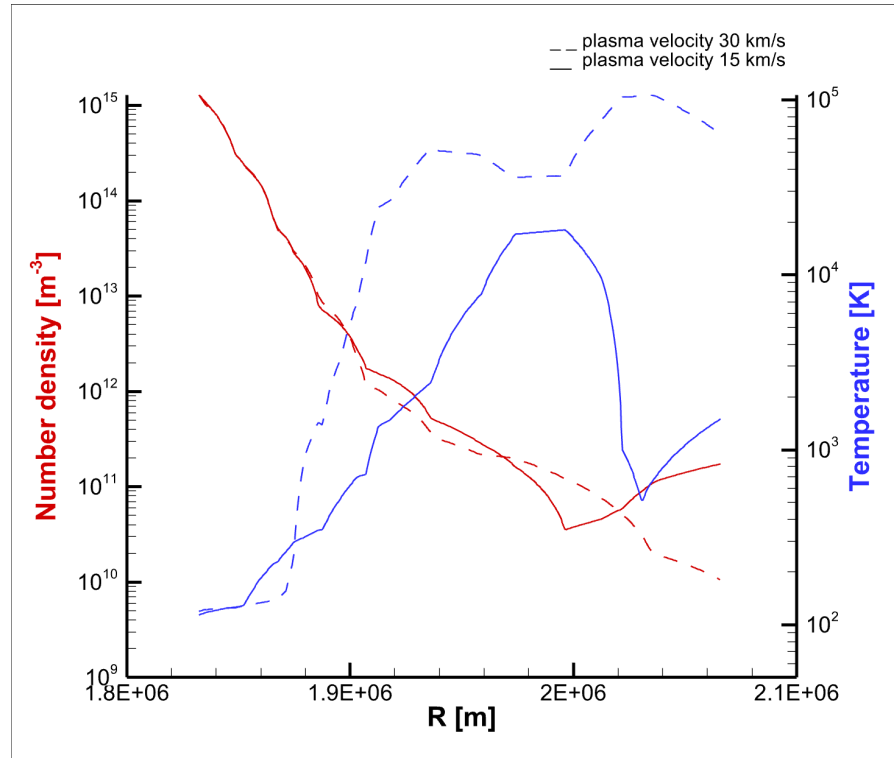
Figure 18: Line plots displaying the number density and temperature profiles for varying velocities of the inserted plasma particles with a plasma particle density of $3 \times 10^8 \mathrm{m}^{-3}$ and temperature of $150eV$.

(a)

(b)
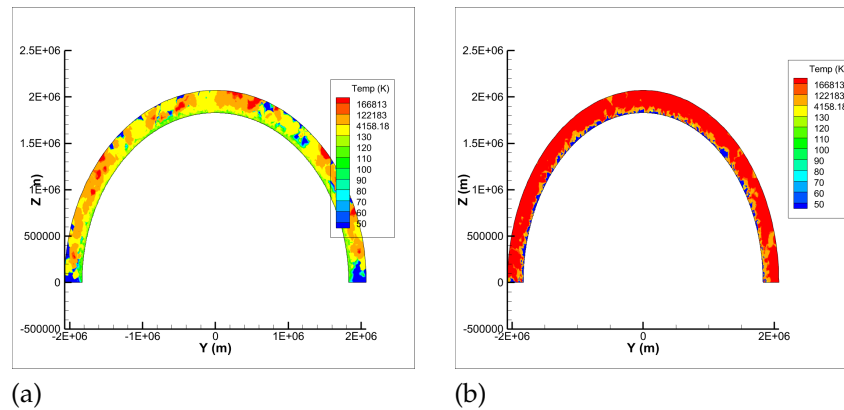
Figure 19: Two dimensional slices through the 3D simulation domain of the temperature field for a day side SO_2 sublimation (a) and night side SO_2 sublimation (b) with O_2 background gas. Both cases contain plasma particles at a density of $3 \times 10^8 \mathrm{m}^{-3}$ and a velocity of 15km/s.

values for each inlet cell, these cases are computationally very expensive, especially when aiming for a good resolution and convergence.
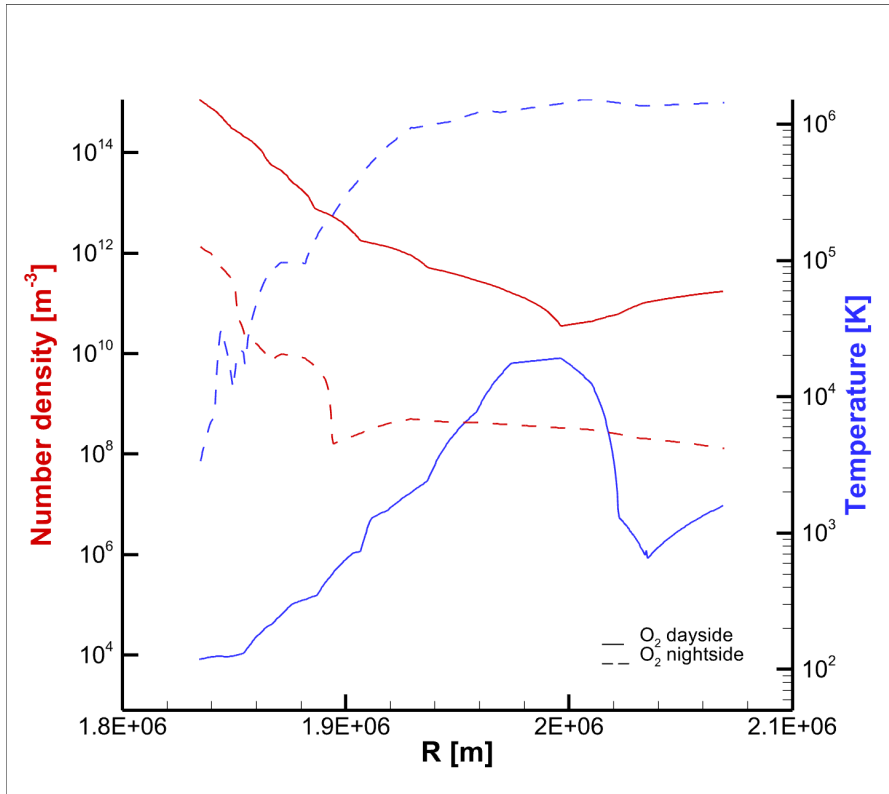
Figure 20: Line plots displaying the number density and temperature profiles for cases comparing day and night side with O_2 background gas with plasma particles at a density of $3 \times 10^8 m^{-3}$ and a velocity of 15km/s.

(a)

(b)
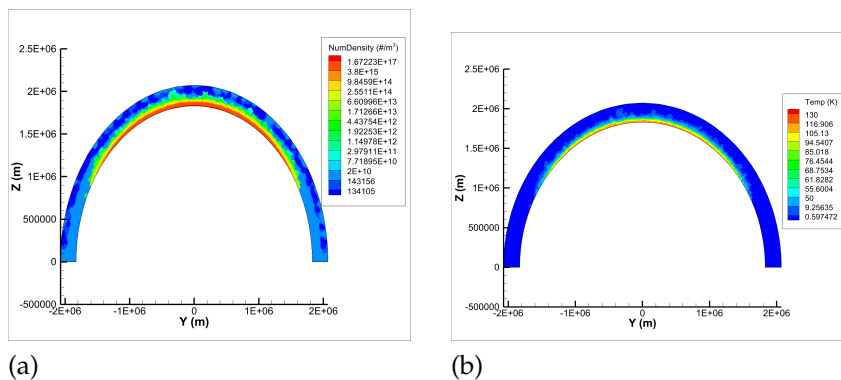
Figure 21: Two dimensional slices through the 3D simulation domain of the number density (a) and temperature (b) field for a day side SO_2 depending on the solar incidence angle and a surface frost distribution with the sub solar point being located at $X = Y = 0$.

9.4 VacV

The most simple case of a volcanic activity is a SO_2 plume into vacuum. This can be used to validate the physical mechanisms

Figure 22: Two dimensional slices through the 3D simulation domain of the number density (a) and temperature (b) field for a day side SO_2 depending on the solar incidence angle and a surface frost distribution with the sub solar point being located at $X = Z = 0$.

in the model. For this case the Spherical Segment mesh with an altitude of 450km and a circular inlet source with a 8km radius is used. Since this model represents a volcanic outburst plume the source area is treated as an inlet boundary with a number density, temperature and velocity. Figure 23 shows a SO_2 plume into vacuum with a density of $6 \times 10^{16} m^{-3}$, a temperature of 500K and a bulk velocity of 850m/s at the source. The plots show the typical plume structure of a hot gas which emerges under gravitational force from the source, expands, cools and slows down until it comes to a stop, where the rising and falling gas collide and form the typical umbrella shaped canopy shock. The inlet velocity follows a half Maxwellian velocity distribution. For a comparison to the cosine law velocity distribution see appendix A.

9.5 $UniSO_2V0$

In the next step a volcanic plume as used before is set in the middle of the large Half Spherical Shell mesh (at $X = Y = 0$) with an altitude of 250km and a uniform sublimation of SO_2 for a fully illuminated surface is set at the surrounding surface. Since the mesh altitude is lower compared to the case before, the plume input values are adjusted for the plume to fit into the simulation domain. Different input values for the plume are discussed in the next section.

(a)   (b)
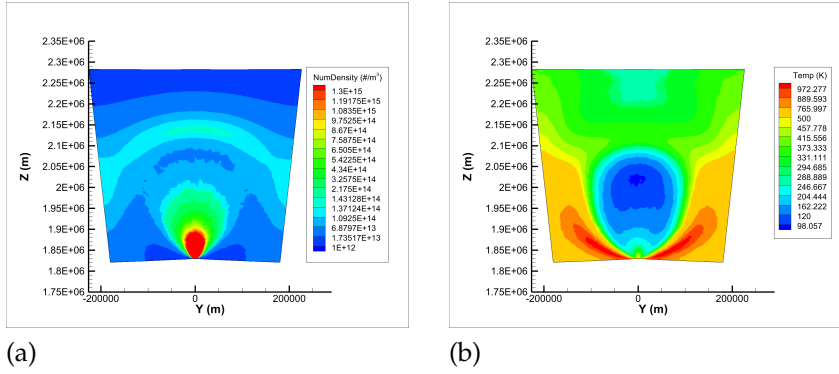
Figure 23: Two dimensional slices through the 3D simulation domain of the number density (a) and temperature (b) field for a SO_2 plume into vacuum.

9.5.1 *No plasma impact*

For the volcanic plume a number density of $3 \times 10^{17}\,\mathrm{m}^{-3}$, a surface temperature of 300K and a outflow velocity of 500m/s were set. The dayside sublimation atmosphere was set with a number density of $1 \times 10^{15}\,\mathrm{m}^{-3}$ and a temperature of 115K. Figure 24 shows two dimensional slices through the simulation domain of the number density and temperature fields. The plume shows the same structure as the plume into vacuum VacV shown in figure 23. However, the surroundings of the plume and the interaction of the plume material with the sublimating frost can be observed. The plume increases the exobase along the center of the plume to ~ 175km and at a location 45 degree from the plume to ~ 45km. Compared to the exobase of a uniform sublimation surface interacting with plasma particles of ~ 30km the plume is able to increase the exobase at larger distances to higher values.

The temperature field at the sides of the plume (as shown in figure 24b) is particularly interesting. The region in the domain where material of the plume canopy falls down and material from the plume center expands horizontally from the plume source and interacts with the sublimating material reaches temperatures well in excess of surface temperatures. In figure 25 two vertical profiles are compared, one being located in the center of the plume reaching from the surface to end of the domain and one being located on the left side of the plume within the hot region. The plot compares the number density, the translational temperature and the rotational temperature along the two profiles.
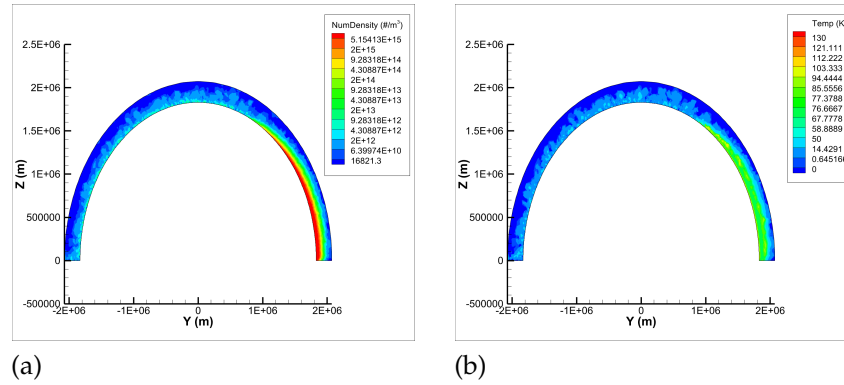
(a)   (b)
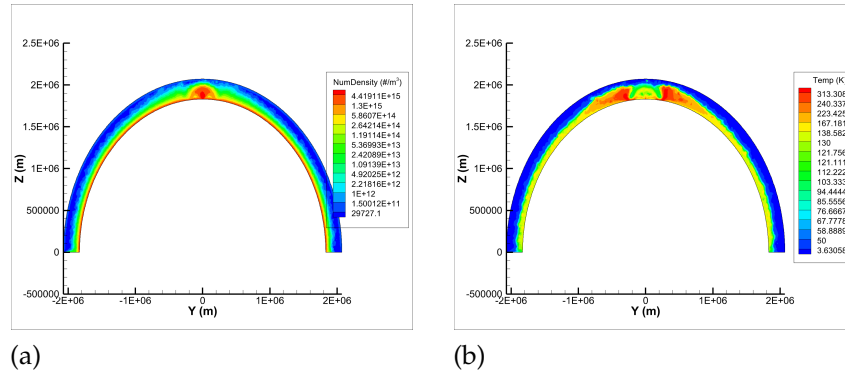
Figure 24: Two dimensional slices through the 3D simulation domain of the number density (a) and temperature (b) field for a SO_2 plume into a day side sublimation atmosphere.
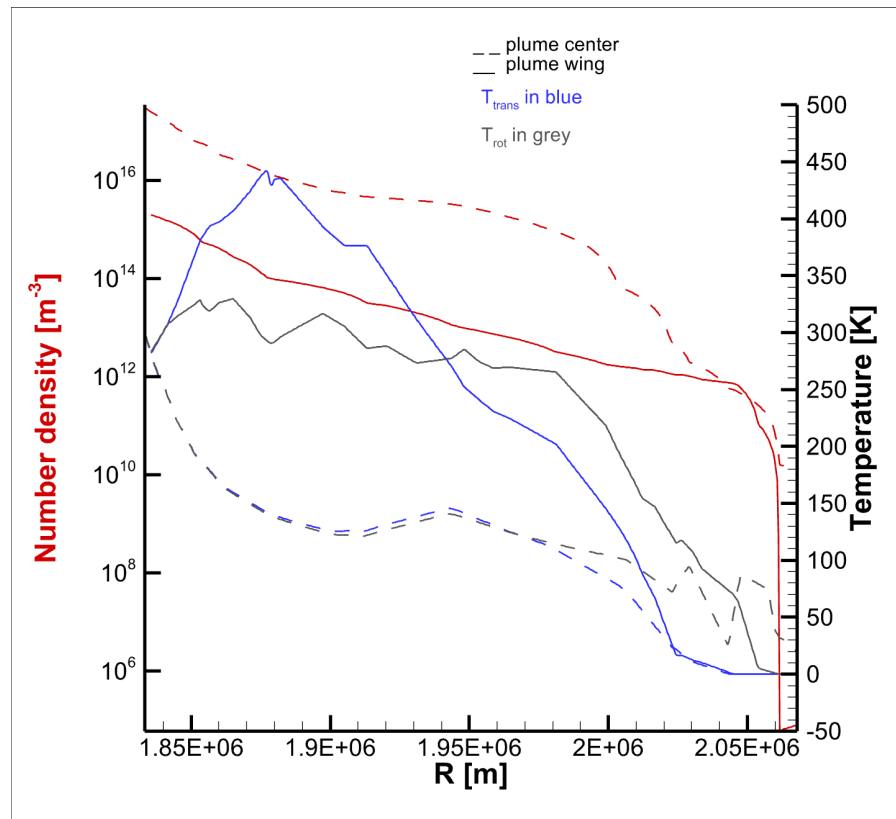
Figure 25: Line plots displaying the number density, translational and rotational temperature profiles for vertical profiles in the center of a plume and at the side of a plume.

It is expected that the number density in the center of the plume is higher than in the wing region before it drops at a height of $\sim 180 - 200 \mathrm{km}$ where the canopy shock of the plume is located. On the other hand while comparing the temperature profiles the hot wing region seems to be in non-LTE. In partic-

ular, where the hottest part is located (at a height of ~ 50km) the translational and rotational temperatures show the highest difference. In comparison, in the center of the plume both temperature profiles show only very small deviations from each other. This might indicate that the gas particles are pushed to this region very rapidly as some kind of shock wave which increases the translational temperature fast while the rotational temperature takes longer to adjust. Experimental and theoretical calculations of the rotational relaxation number Z_{rot} of SO$_2$ by Bass et al. [4] find an increase of Z_{rot} for higher temperatures ($>$ 250K), indicating a slower equilibration process between translational and rotational temperatures for higher temperatures if the gas is not in equilibrium. Figure 26 shows the velocity in Y-direction and the mean speed for both profiles. It displays what was assumed before. In the wing region a peak velocity is reached which points in the negative Y-direction, so material gets pushed away from the plume horizontally.
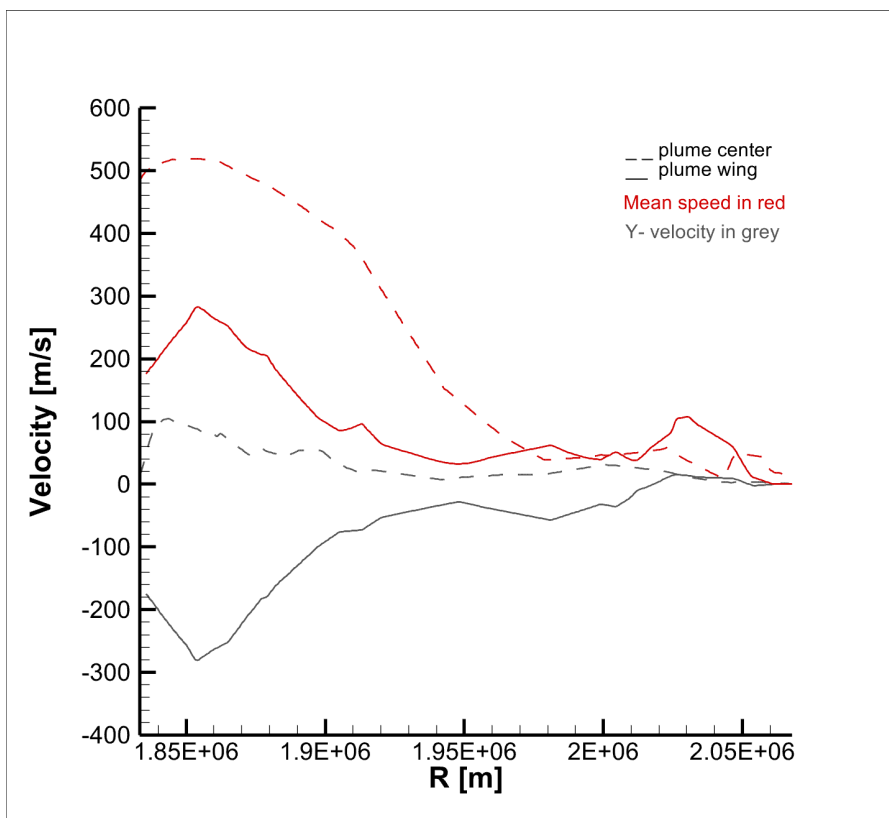
Figure 26: Line plots displaying the velocity in Y-direction and the main speed for vertical profiles in the center of a plume and at the side of a plume.

9.5.2 *Plasma impact*

Plasma particles were added with different inflow velocities of 30km/s and 45km/s. Figure 27 shows two dimensional slices of temperature and number density fields for both cases.

It seems that the plume in each case regulates the influence of the plasma particles. Figure 28 displays that the temperature in the center of the plume is only influenced by the plasma particles above the canopy. This seems to also affect the regions next to the plume. Figure 29 shows the effect of plasma heating for different positions in the simulation domain for the case $UniSO_2V0P1815030$ with 30km/s plasma velocity. The heating effect increases gradually with increasing distance from the plume. Additionally, the change in plasma velocity does only have an effect on the temperature peak above the canopy but not on any other parts.

Further, it is interesting that in comparison to case $UniSO_2V0$ in figure 24 the non-equilibrium hot wings next to the plume seem to not exist here. Figure 30 displays the translational and rotational temperatures for the profile within the wing of the plume. The plot confirms the assumption and the hot wing effect seen before does not occur here. A very small deviation of the temperatures is seen at $\sim 50-60$km from the surface. This implies the interaction with the plasma particles at the plume canopy must have an effect on the plume particles preventing the heating in the plume wings.

9.6 $UniSO_2V45$

In this case the impact of another position within the atmosphere and varying input parameters of the volcanic plume are studied. The volcanic plume is located at a position 45 degree from the middle of the mesh on the Y-axis with a circular source with a 6km radius. Figure 31 shows the plume set in a day side atmosphere with a number density of $1 \times 10^{15}m^{-3}$ and a temperature of 115K. The plume itself has an inlet density of $3 \times 10^{17}m^{-3}$, a surface temperature of 300K and a outflow velocity of 500m/s. It is recognisable that the smaller source surface has an effect on the height of the plume but shows the same effect of creating the hot wing areas to the sides.

Figure 32 shows the radial integrated column density which displays the ring structure of the region below the canopy of lower density.

9.6.1   *No plasma impact*

Next, the plume is enlarged by increasing the outflow density to $3 \times 10^{19} \mathrm{m}^{-3}$ and has a surface temperature of 300K and a outflow velocity of 500m/s. The uniform sublimation atmosphere is exchanged with a sublimation varying with incidence angle and therefore latitude which is also influenced by the surface frost distribution of the model by Doute et al. ([17]). The sub solar point is set at the middle of the mesh, at $X = Y = 0$. Figure 33 shows the number density and temperature fields for this case. In combination the sublimation and the plume are able to increase the exobase to a height of 220km.

From looking at the temperature field in figure 33b it is possible to assume that the extent of the hot wings next to the plume depends on the amount of sublimated material at the surface. The plume shown here also creates the hot wings to both sides. However, a clear asymmetry in the hot wings can be observed. At the plume side facing the subsolar point, where the sublimation densities are higher, the wing reaches higher temperatures at higher altitudes compared to the case with uniform lower sublimation densities. On the other side though, the wing at a position facing away from the subsolar point is much smaller. Figure 34 shows a comparison of vertical profiles at the different positions and their temperatures.

The plot displays that only the wing on the plume side facing the subsolar point is able to reach temperatures as high as in the case described in the section before. However, here the maximal deviation of the translational and rotational temperature modes occurs at an higher altitude of $\sim$ 100km which is almost double the height compared to the case which could be seen before with uniform sublimation. On the contrary, the wing on the plume side facing away from the subsolar point shows a low deviation at a height of $\sim$ 50km but both modes stay below temperatures of 250K. However, at higher altitudes the profile show larger deviations of the translational and rotational modes. These are assumed to result from the very rarefied atmosphere at far distances from the subsolar point and at higher altitudes since the sublimation there is low in density and particles may collide at a lower frequency which leads to a limited energy transfer between the different modes. The temperature profile in the center of the plume follows the expected course.

9.6.2 *Plasma impact*

For the analysis of the interaction of the plume with plasma particles, the plume is set with a number density of $3 \times 10^{17} \mathrm{m}^{-3}$ and has a surface temperature of 300K and a outflow velocity of 500m/s. The plume is set in a uniform SO_2 day side atmosphere with plasma particles inserted from the Z-direction at a density of $3 \times 10^8 \mathrm{m}^{-3}$, a temperature of 150eV and a velocity of 30km/s. Figure 35 shows two dimensional slices of the number density and temperature fields and figure 36 the comparison of vertical profiles along the plume for this plume and a seperate calculation with a plume at 0° which gets bombarded by the plasma from straight above. The comparison shows that for a center plume profile the plume at 45° gets heated already at lower altitudes of around 120km whereas the plume at 0° only experiences heating above the canopy of the plume starting at ~ 180km. Both of the wing profiles do not show signs of the hot wings to the sides. However, the wing of the plume at 0° shows a heating effect from the beginning whereas the wing of the plume at 45° only experiences a heating effect from an altitude of 120km. This is a similar height as for the plume center of this plume but with the difference that the wing gets heated faster. So, probably both regions get heated by particles coming from the side of the plume.

9.7 UniSO₂V0V45

In the last case two plumes, one at the center and one at 45 degrees from the center were added to the half spherical shell domain. The center plume has a circular source with a radius of 8km and the side plume has a circular source with a radius of 6km.

9.7.1 *No plasma impact*

First, both plumes are set in a day side sublimation atmosphere with a number density of $1 \times 10^{15} \mathrm{m}^{-3}$ and a temperature of 115K. Both plumes have a inlet density of $3 \times 10^{17} \mathrm{m}^{-3}$, a surface temperature of 300K and a outflow velocity of 500m/s. Figure 37 shows the number density and temperature fields for this case and table 6 contains the height for different positions within the field.

The temperature field shows the hot wings beside both of the plumes. When considering the exobase height at different positions it seems that though the plume at 0° is larger the structure of both plumes is the same. Also with a distance of 45° the plumes don't seem to interact as much or influence each other. This can be confirmed when looking at the temperature profiles for the different positions in figure 38 . It also shows that the position in between the plumes is not as much affected by the plumes since the profile is very similar to the one located 45° on the opposite side of the smaller plume.

9.7.2 *Plasma impact*

In the next step plasma particles are added to the case mentioned before. Therefore, different parameter variations were studied as listed in table 7.

Figure 39 shows the number density and temperature along vertical profiles for the first group (cases 1 − 3) for different positions within the atmosphere: the center of the plume at 0°, the wing of the plume at 0° and the sublimation atmosphere at 45° (opposite of the small plume). The first case in figure 39a shows almost no sign of plasma interaction. The number densities are only enhanced close to the plume and the only heating effect is seen in the temperature profile of the plume wing. However, all temperature profiles drop very fast at a height of ∼ 180km. The profiles of the sublimation atmosphere do not seem to be influenced by either the plasma particles or the plumes. They behave as seen before for a basic sublimation atmosphere. In contrast, cases 2 and 3 show heating effects at higher altitudes above the plume, but also above the sublimation atmosphere. It seems that the canopy can regulate the plasma influence much better, since the heating effect in the plume center is lower than at the plume wing. However, the effect of the hot wing seen for case 1 seems to be suppressed by the plasma interaction. The sublimation atmosphere is heated the most. The heating effect shows in both cases 2 and 3 a peak at ∼ 100km which is about the height of the sublimation atmosphere in case 1. This peak therefore, could show the main interaction area of plasma and atmospheric particles. Further, table 8 shows the different exobase altitudes for the various cases and different positions. For cases 1 − 3 it shows again the clear difference between case 1 and cases 2 and 3. Case 1 does not show signs of plasma interaction, where as in cases 2 and 3 the altitude of the exobase for

every position increases. However, above the wing case 3 has a lower exobase altitude but it also shows low signs of the wing heating effect. This could indicate a less strong plasma interaction. For the second group of cases $(4-6)$ the plasma particle temperature was increased and the velocity reduced. Similar to cases 2 and 3 the regulation of the heating effect by the plume is observable. Here it is even clearer that a heating effect only occurs above the canopy from a height of 180km. The plume center heating peak in case 4 however implies that there weren't enough particles to heat the entire upper atmosphere since after reaching the peak, the temperature drops again. Also, the wing heating effect is not seen in any of these three cases. The sublimation atmosphere is showing a gradual decrease in number density for all three cases, however the heating effect can be seen everywhere. The lower density is also displayed in the exobase altitude for all three cases, as they are lower than in the cases $1-3$. This can probably be explained with the lower velocity of the plasma particles. Though, in cases 5 and 6 the heating effect is the largest for the plume wing, which is justifiable since it interacts with particles from directly above whereas the sublimation atmosphere gets impacted from the side. For the third group of cases $(7-9)$ the effect of the plasma in the first case is again almost not observable. Especially, for the sublimation atmosphere no enhancement in density or temperature is seen and also for the plume positions no heating above the plume can be observed. However, in cases 8 and 9 the plasma influence can be clearly seen. In case 8 the atmosphere experiences the highest heating effect. This could be due to the higher velocity which enables it for more plasma particles coming from Z-direction to faster enter the atmosphere. Also, in case 8 the heating of the plume wing by plasma particles only occurs above $\sim$ 130km but the effect of the hot wing can still be observed at around $\sim$ 70km. However, case 9 shows the highest exobase altitudes of all cases, which can be explained with the increased plasma input density. In comparison it is indicated that for a density of $1 - 3 \times 10^8 \mathrm{m}^{-3}$ the heating effect is rather low or not even observable. Further, with higher velocities the heating effect is very large and the energy deposition seems too high. Therefore, for further studies values of lower velocity and higher number density would be interesting.

CASE	SUBLIMATION N T V [m^{-3}] [K] [m/s]	PLUME N T V [m^{-3}] [K] [m/s]	PLASMA N T V [m^{-3}] [eV] [km/s]
UniSO$_2$	10^{15} / 115 / v_th	-	-
UniSO$_2$P1815015	10^{15} / 115 / v_th	-	10^8 / 150 / 15
UniSO$_2$P1815030	10^{15} / 115 / v_th	-	10^8 / 150 / 30
UniSO$_2$P1815045	10^{15} / 115 / v_th	-	10^8 / 150 / 45
UniSO$_2$P3815015	10^{15} / 115 / v_th	-	3×10^8 / 150 / 15
UniSO$_2$P4815015	10^{15} / 115 / v_th	-	4×10^8 / 150 / 15
UniSO$_2$P5815015	10^{15} / 115 / v_th	-	5×10^8 / 150 / 15
UniSO$_2$P1915015	10^{15} / 115 / v_th	-	10^9 / 150 / 15
UniSO$_2$O2210 O$_2$	SO$_2$: 10^{15} / 115 / v_th O$_2$: 2×10^{10}	-	-
UniSO$_2$O2212 O$_2$	SO$_2$: 10^{15} / 115 / v_th O$_2$: 2×10^{12}	-	-
UniSO$_2$O2215	SO$_2$: 10^{15} / 115 / v_th O$_2$: 2×10^{15}	-	-
UniSO$_2$O2212P3815015	SO$_2$: 10^{15} / 115 / v_th O$_2$: 2×10^{12}	-	3×10^8 / 150 / 15
UniSO$_2$O2212P3815030	SO$_2$: 10^{15} / 115 / v_th O$_2$: 2×10^{12}	-	3×10^8 / 150 / 30
UniSO$_2$O2215P3815015	SO$_2$: 10^{15} / 115 / v_th O$_2$: 2×10^{15}	-	3×10^8 / 150 / 15
UniSO$_2$NO2215P3815015	SO$_2$: 10^{12} / 90 / v_th O$_2$: 2×10^{12}	-	3×10^8 / 150 / 15

Table 3: A Listing of all gas result cases considered here (A).

CASE	SUBLIMATION N T V $[m^{-3}]$ [K] [m/s]	PLUME N T V $[m^{-3}]$ [K] [m/s]	PLASMA N T V $[m^{-3}]$ [eV] [km/s]
SSO$_2$	changing with latitude	-	-
VacV	vacuum	6×10^{16} / 500 / 850	-
UniSO$_2$V0	10^{15} / 115 / v_{th}	3×10^{17} / 300 / 500	-
UniSO$_2$V0P1815030	10^{15} / 115 / v_{th}	3×10^{17} / 300 / 500	10^8 / 150 / 30
UniSO$_2$V0P1815045	10^{15} / 115 / v_{th}	3×10^{17} / 300 / 500	10^8 / 150 / 45
UniSO$_2$V45	10^{15} / 115 / v_{th}	3×10^{17} / 300 / 500	-
SSO$_2$V45L	changing with latitude	3×10^{19} / 300 / 500	-
UniSO$_2$V45P3815030	10^{15} / 115 / v_{th}	3×10^{17} / 300 / 500	3×10^8 / 150 / 30
UniSO$_2$V0V45	10^{15} / 115 / v_{th}	3×10^{17} / 300 / 500	-
UniSO$_2$V0V45P	10^{15} / 115 / v_{th}	3×10^{17} / 300 / 500	plasma variations as in table 7

Table 4: A Listing of all gas result cases considered here (B).

CASE	N $[m^{-3}]$	T $[K]$	v $[km/s]$	E $[MJ/m^{-3}]$
UniSO$_2$P1815015	10^8	150	15	8.055
UniSO$_2$P1815030	10^8	150	30	32.22
UniSO$_2$P1815045	10^8	150	45	72.5
UniSO$_2$P3815015	3×10^8	150	15	24.17
UniSO$_2$P4815015	4×10^8	150	15	32.22
UniSO$_2$P5815015	5×10^8	150	15	40.28
UniSO$_2$P1915015	10^9	150	15	80.55

Table 5: The various cases of plasma impact at a uniform sublimation atmosphere, their input values for number density, temperature and velocity and the energy deposition in Mega Joule per cubic metre.

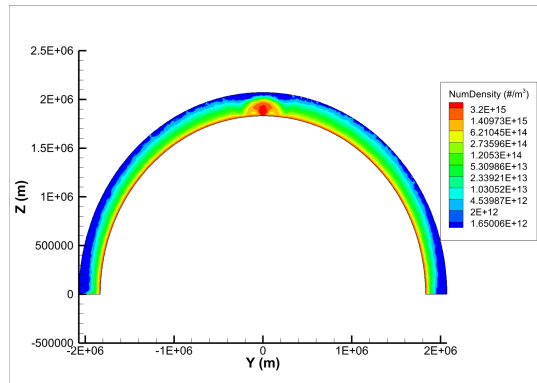| POSITION	EXOBASE $[km]$
plume center (0°)	187
plume wing (0°)	37
plume center (45°)	143
plume wing (45°)	32
in between plumes	29
atmosphere at 45° opposite	28

Table 6: The exobase at different positions for a case with two plumes set in a day side atmosphere.
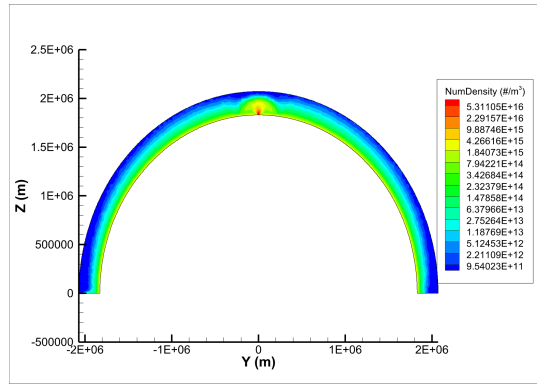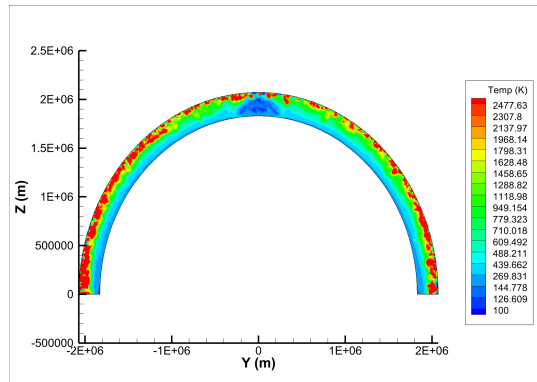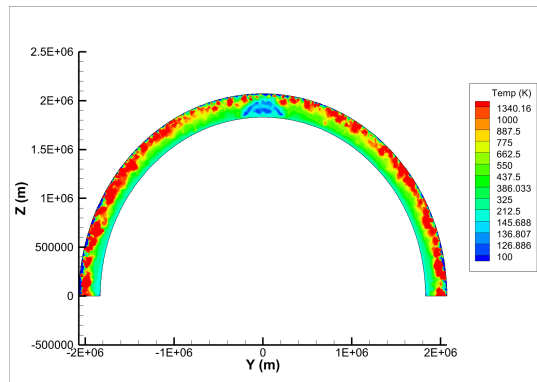
Figure 27: Two dimensional slices through the 3D simulation domain of the number density and temperature fields of a volcanic plume within a sublimation atmosphere and with additional plasma particles at 30km/s (a and b) and 45km/s (c and d).
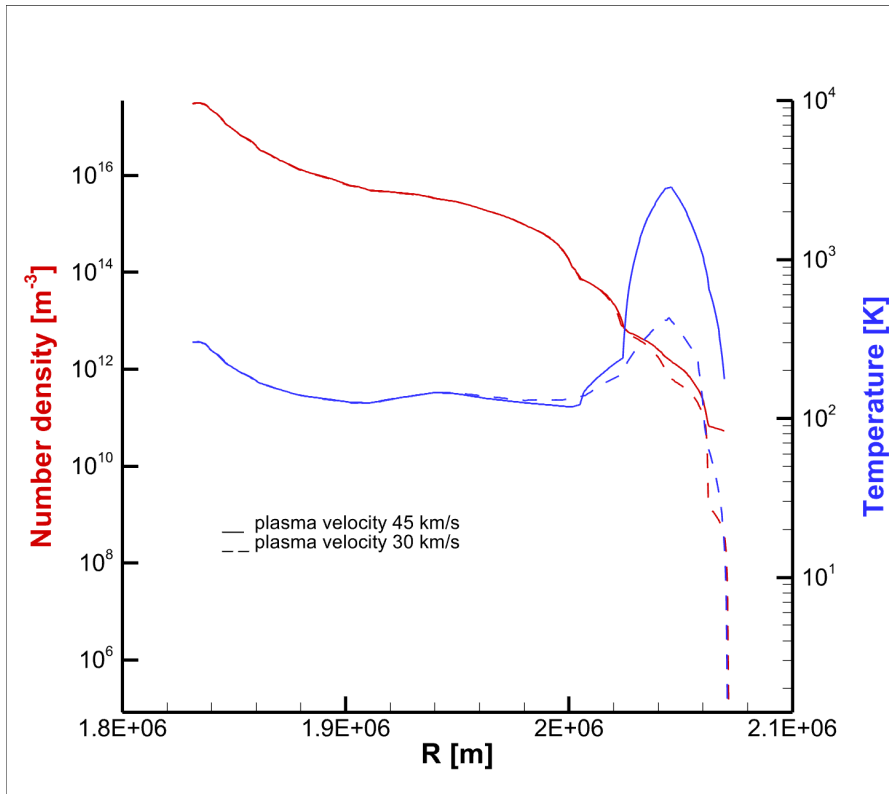
Figure 28: Line plots displaying the number density and temperature along vertical profiles through the center of the plume for cases of different plasma velocities.
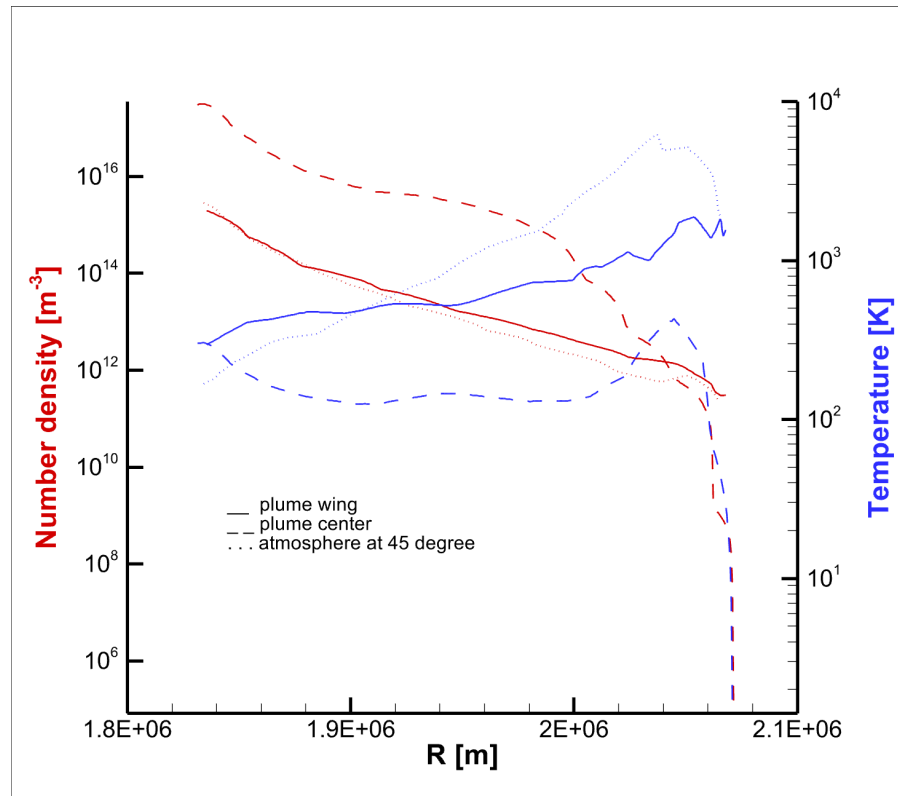
Figure 29: Line plots displaying the number density and temperature along vertical profiles through the center of the plume, the plume wing and in the atmosphere at 45 degree from the plume center for a plasma velocity of 30km/s.
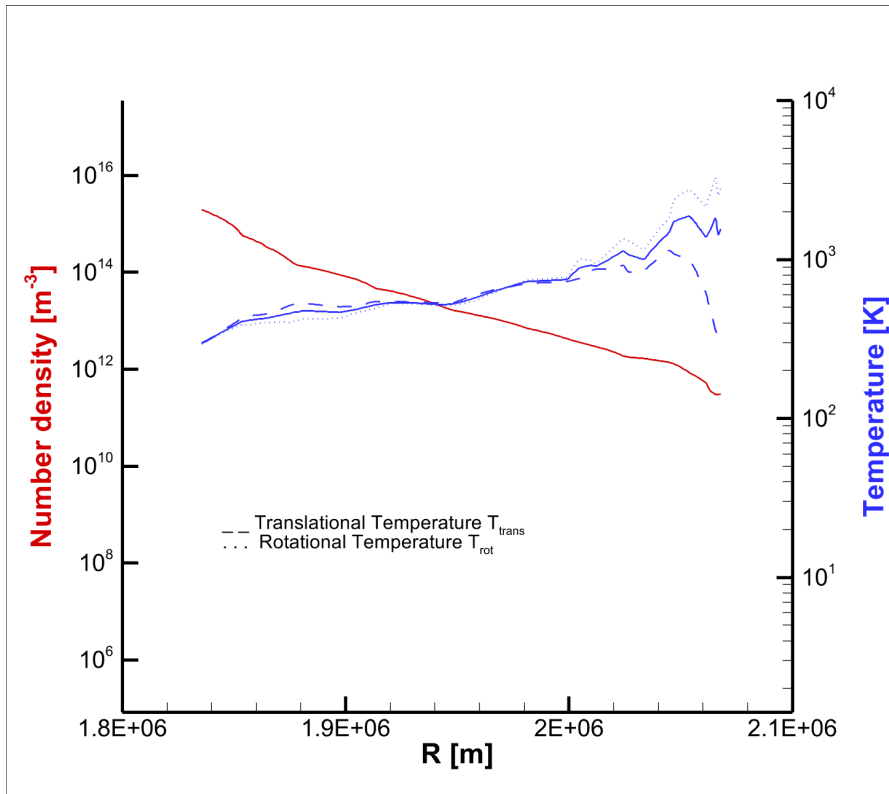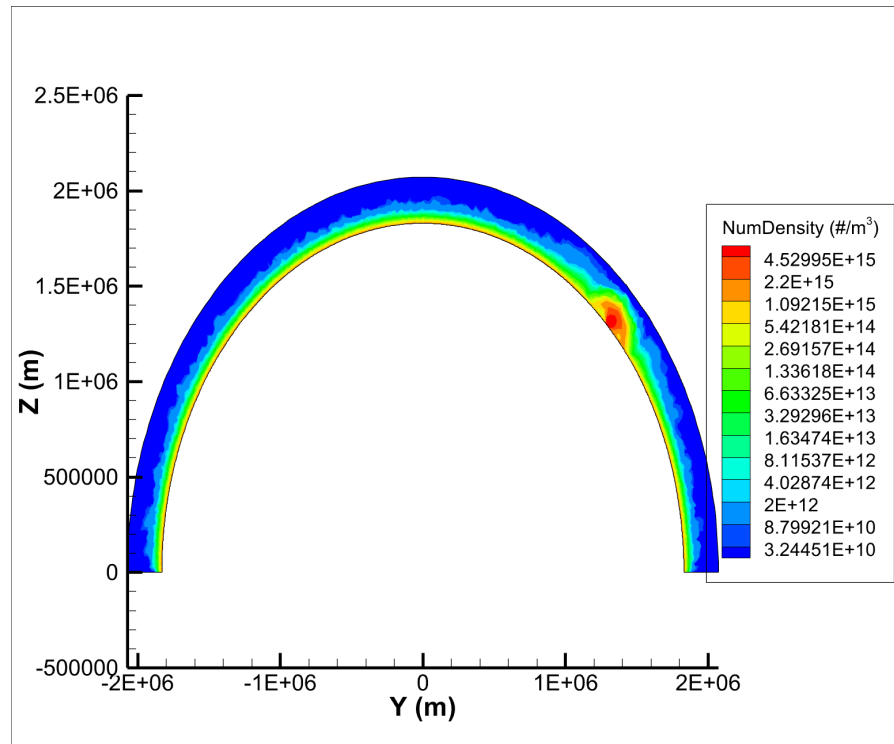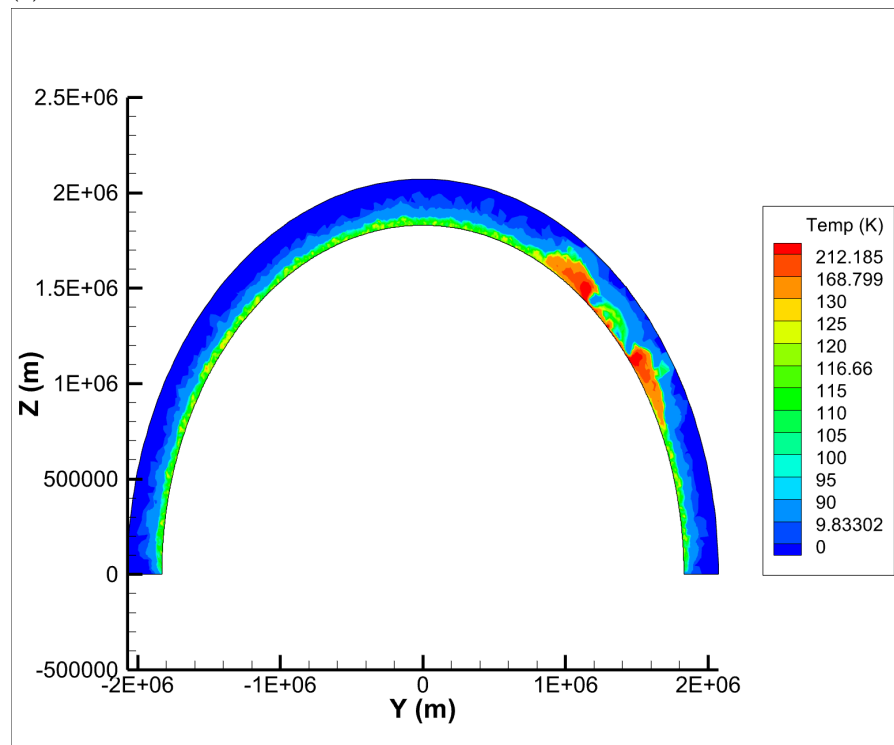
Figure 30: Line plots displaying the number density and different temperature modes along the vertical profile through the plume wing for a plasma velocity of 30km/s.
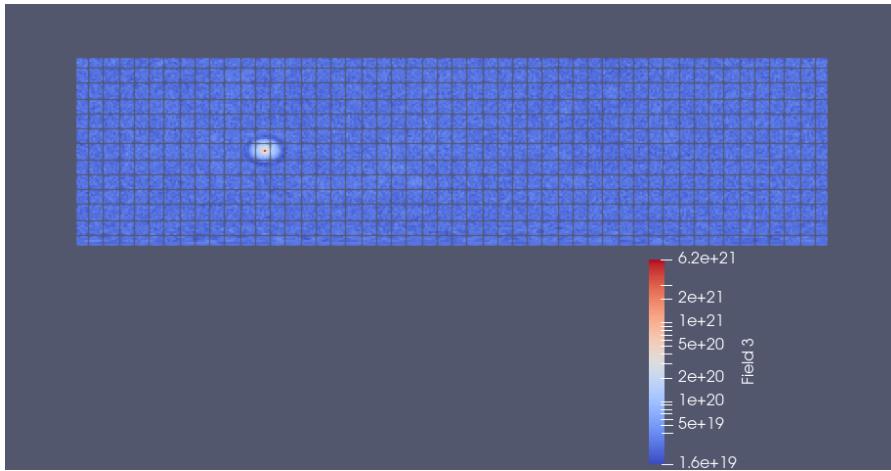
(a)

(b)

Figure 31: Two dimensional slices through the 3D simulation domain of the number density (a) and temperature (b) field for a SO_2 plume into a day side sublimation atmosphere at an angle of 45 degree (case $\mathrm{UniSO_2V45}$).

(a)

(b)

Figure 32: The radial integrated column density of a plume at 45 degree within a uniform sublimation atmosphere and in (b) a close up of the plume region (case UniSO$_2$V45).
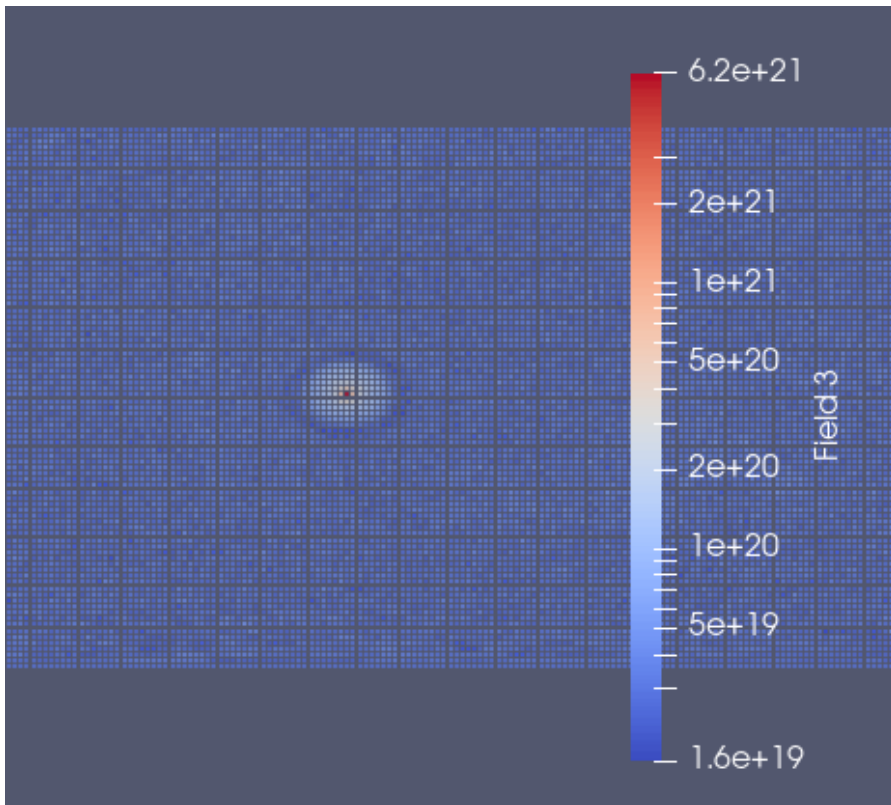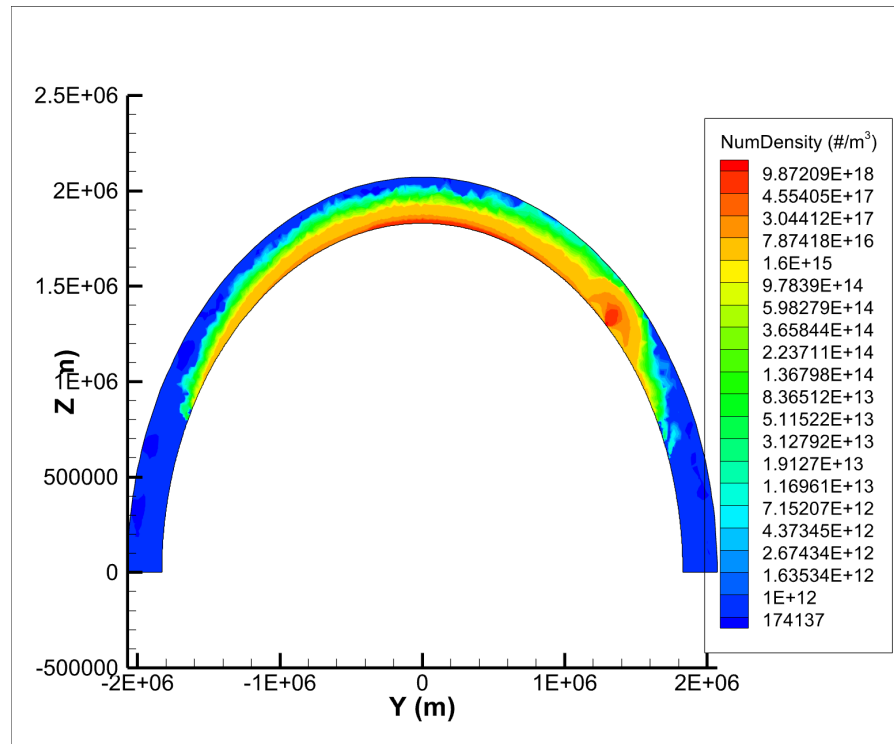
(a)
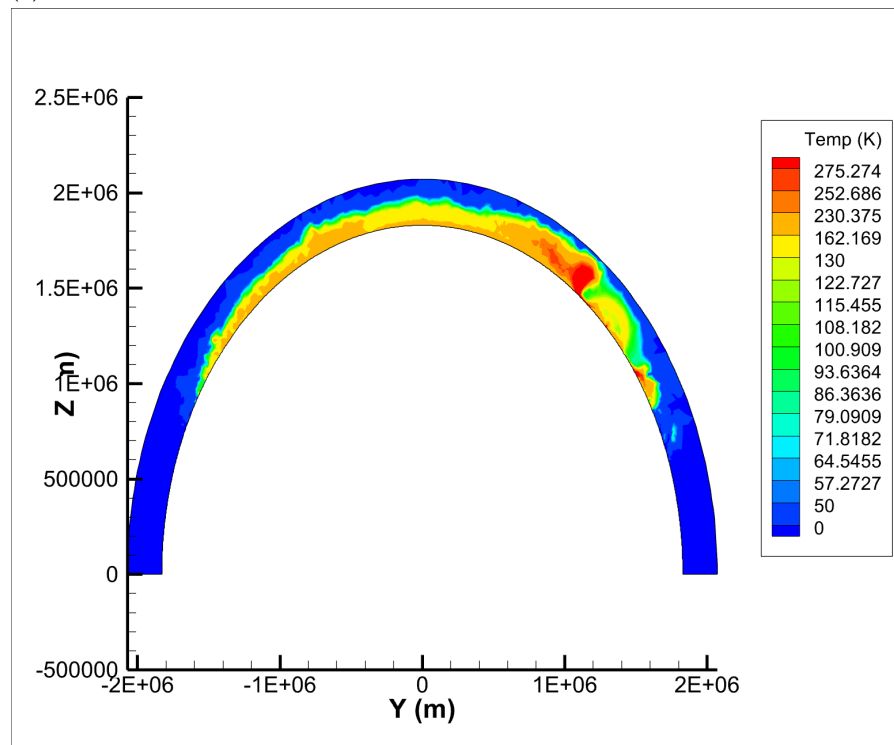
(b)

Figure 33: Two dimensional slices through the 3D simulation domain of the number density (a) and temperature (b) field for a SO_2 plume into a day side sublimation atmosphere with latitudinal variations depending on the incidence angle and the surface frost distribution (case SSO_2V45L).
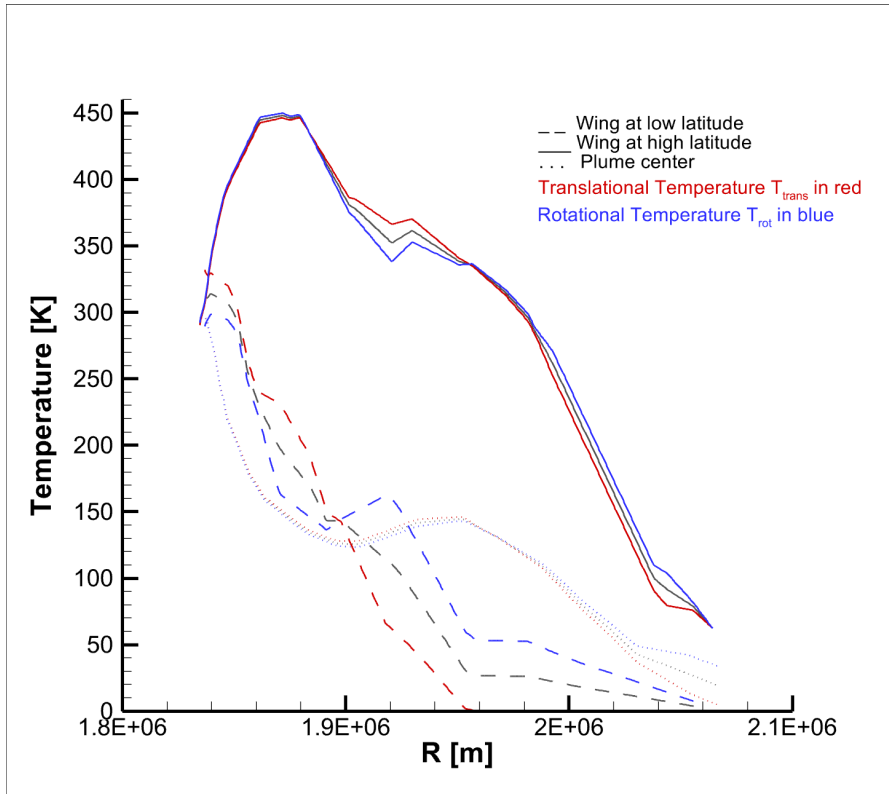
Figure 34: Vertical line profiles of the translational and rotational temperatures for positions at the center of the plume, the subsolar point facing wing and the anti subsolar point facing wing.
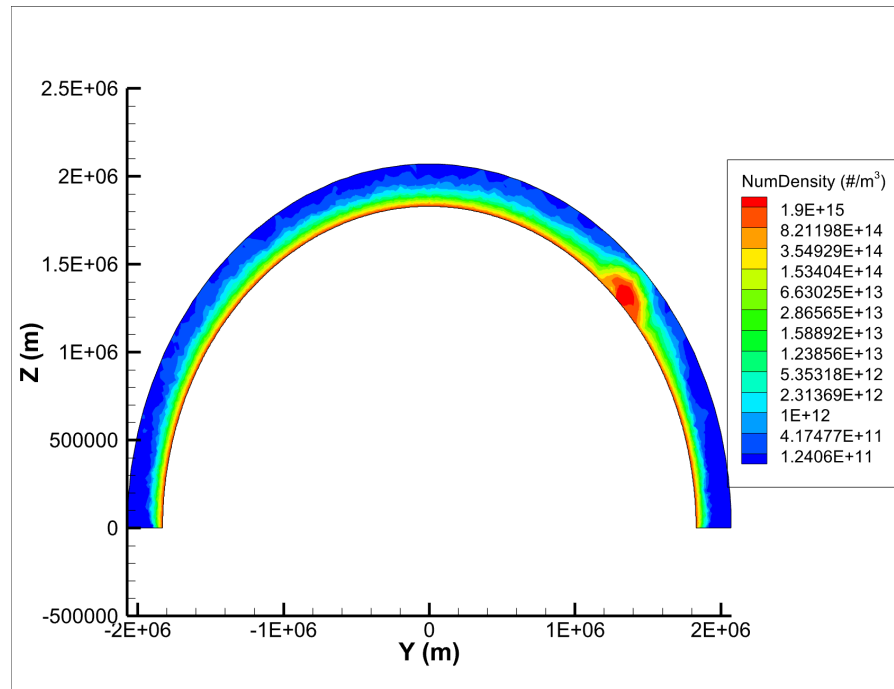
(a)
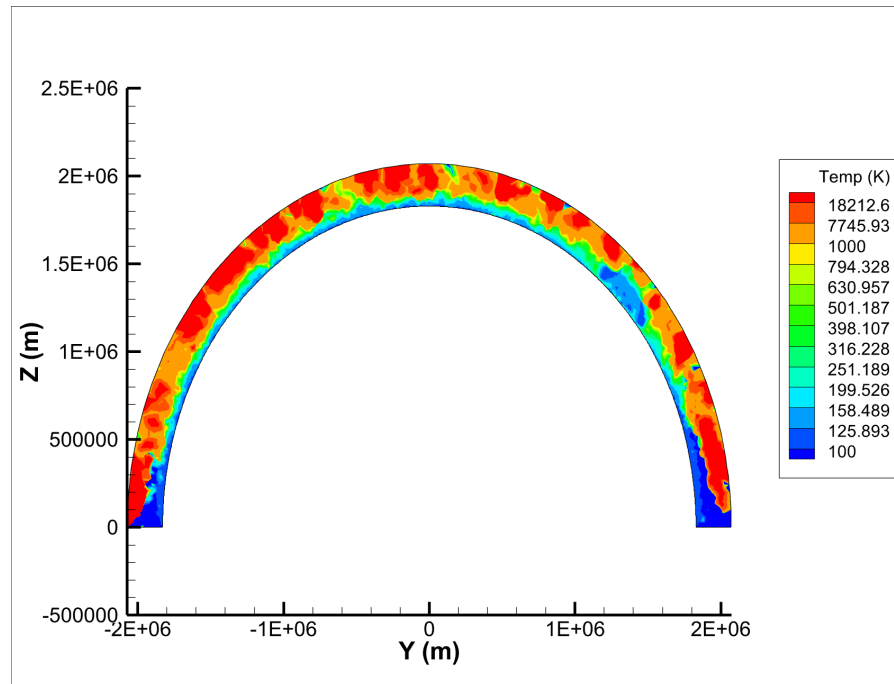
(b)

Figure 35: Two dimensional slices through the 3D simulation domain of the number density (a) and temperature (b) field for a SO_2 plume at $45°$ into a day side sublimation atmosphere and with plasma particles from Z-direction.

Figure 36: Vertical line profiles of the number density and temperature for different positions in the case of a plume at 45° and a plume at 0° within a day side sublimation atmosphere with plasma particles from Z-direction.

(a)
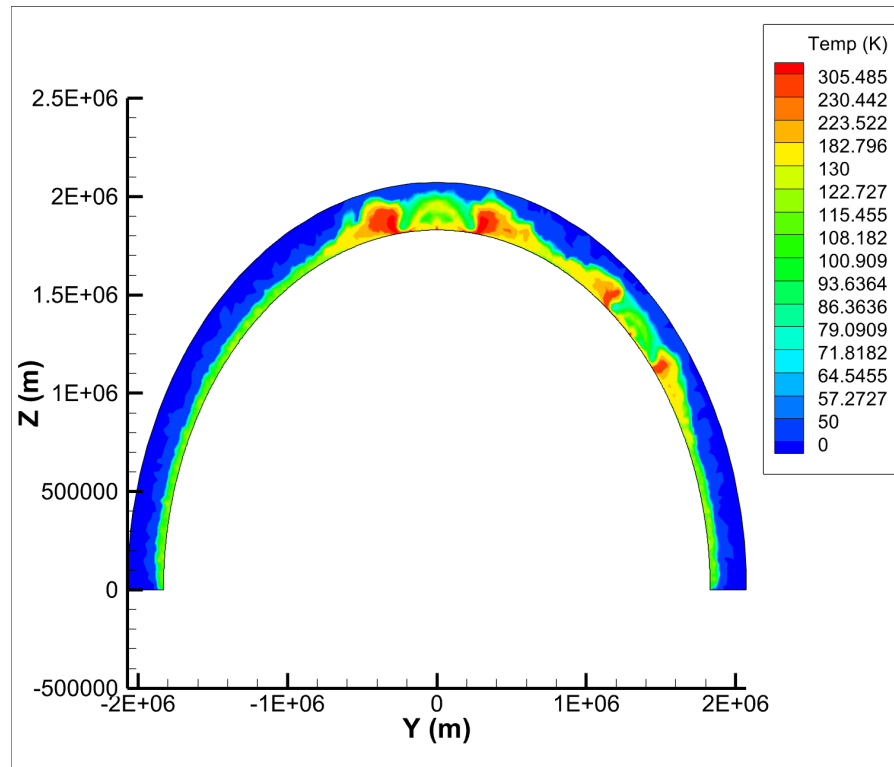
(b)

Figure 37: Two dimensional slices through the 3D simulation domain of the number density (a) and temperature (b) field for two SO$_2$ plumes into a day side sublimation atmosphere.
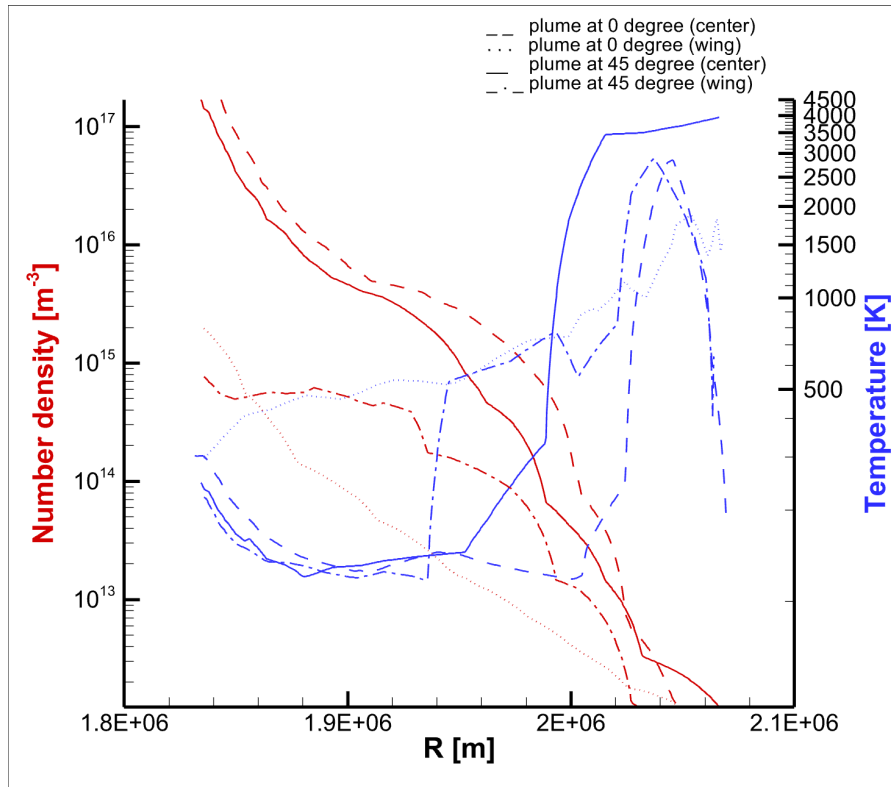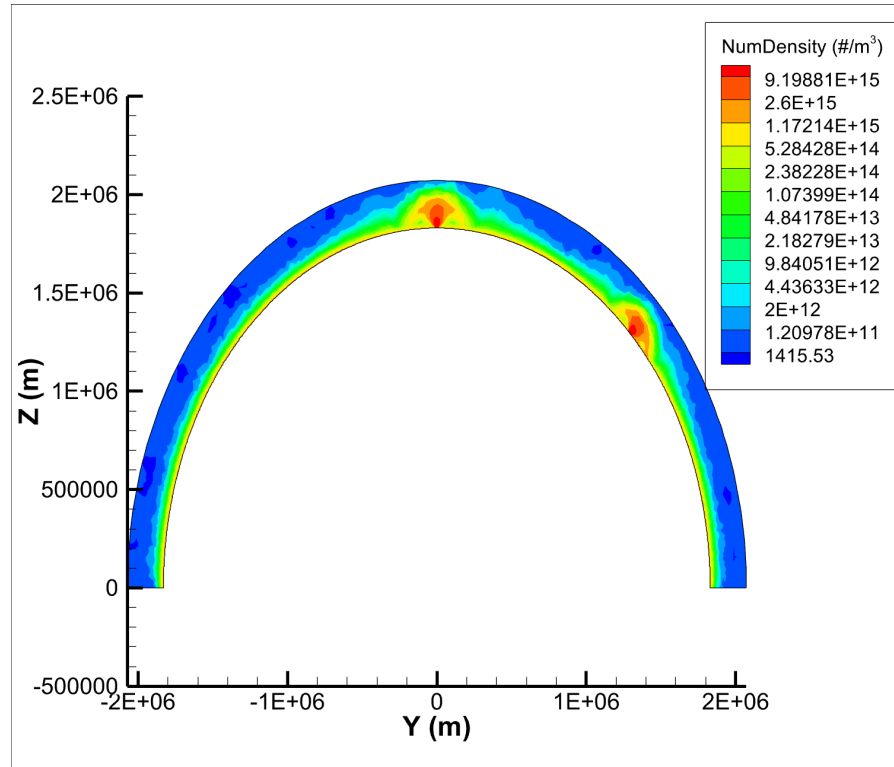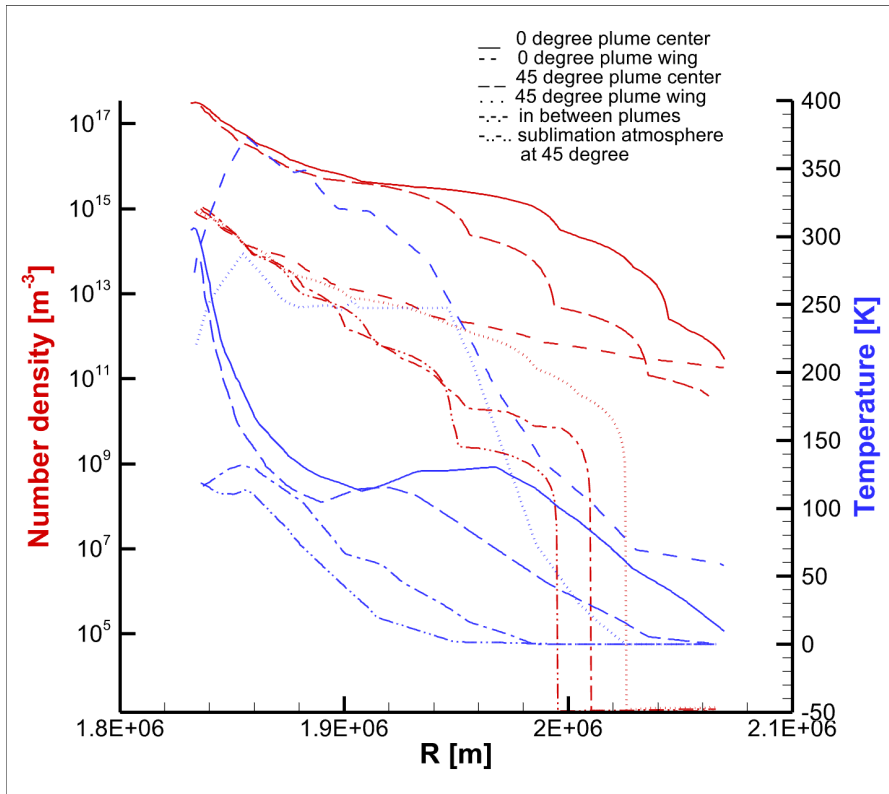
Figure 38: Vertical line profiles of the number density and temperature for different positions in the case of 2 plumes within a day side sublimation atmosphere.

CASE NR.	N $[M^{-3}]$	V $[km/s]$	T $[eV]$	EFFECTS
1	3×10^8	30	100	no plasma effect, wing effect
2	4×10^8	30	100	plasma heating, no wing effect
3	5×10^8	30	100	plasma heating, small wing effect
4	3×10^8	15	150	plasma heating, no wing effect
5	4×10^8	15	150	plasma heating, no wing effect
6	5×10^8	15	150	plasma heating, no wing effect
7	1×10^8	45	150	low plasma heating
8	5×10^8	45	150	highest plasma heating
9	1×10^9	45	150	plasma heating

Table 7: Cases of different plasma particle input parameter UniSO$_2$V0V45P(number density N, velocity V and temperature T) for the case of 2 plumes in a uniform sublimation atmosphere and their main effects.

CASE NR.	PC [km]	PW [km]	45 [km]
1	186	32	30
2	190.8	34.2	31.2
3	190.8	30.6	31.2
4	186	32.7	30.2
5	186	32.7	30.7
6	189.2	33.2	31.7
7	185	34.2	30.2
8	189.2	34.2	29.6
9	191.4	34.8	34.8

Table 8: Different exobase altitudes for the cases listed in table 7 for different positions: PC = Plume Center, PW = Plume Wing, 45 = Sublimation atmosphere at 45°.
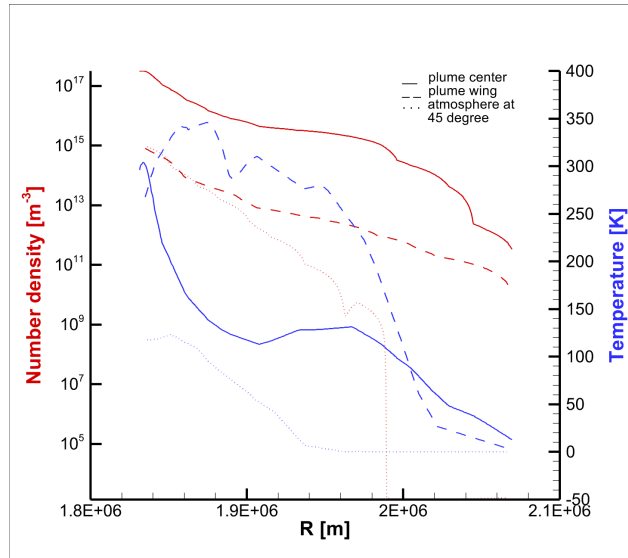
(a)
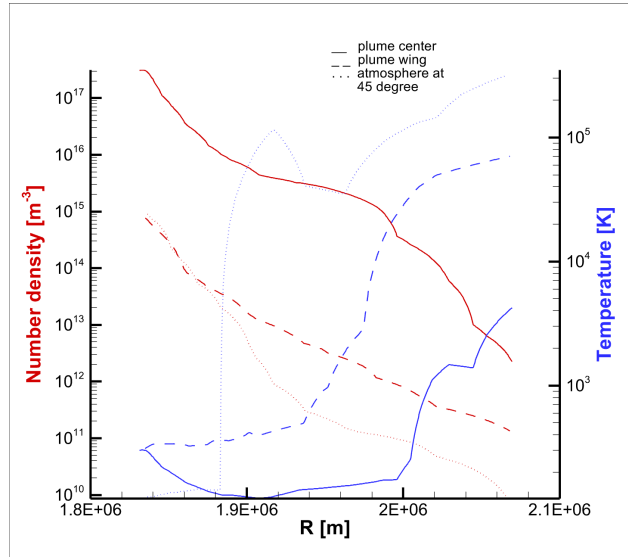
(b)
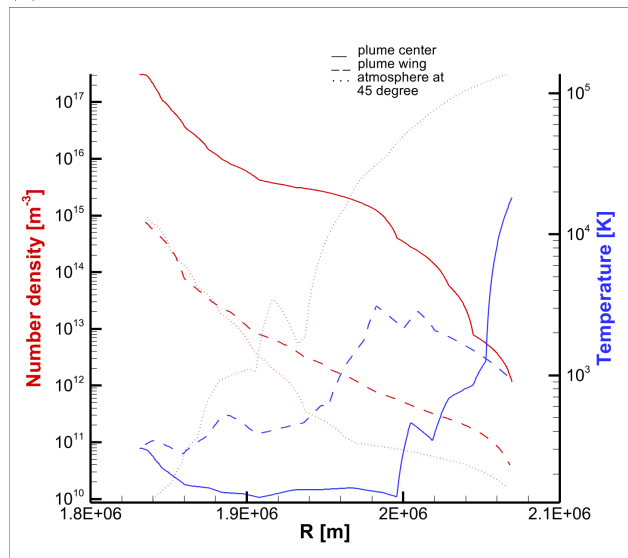
(c)

Figure 39: Vertical line profiles of the number density and temperature for different positions in the atmosphere and for different plasma densities of $3 \times 10^{8} \text{m}^{-3}$ (a), $4 \times 10^{8} \text{m}^{-3}$ (b) and $5 \times 10^{8} \text{m}^{-3}$ (c) with a plasma velocity of 30km/s and temperature of 100eV.
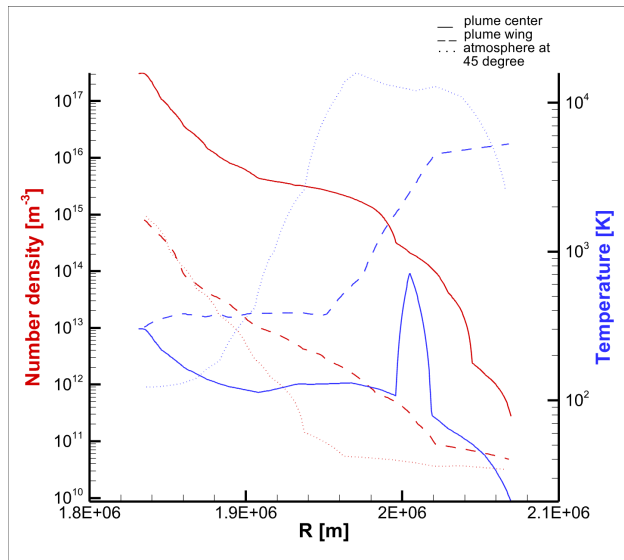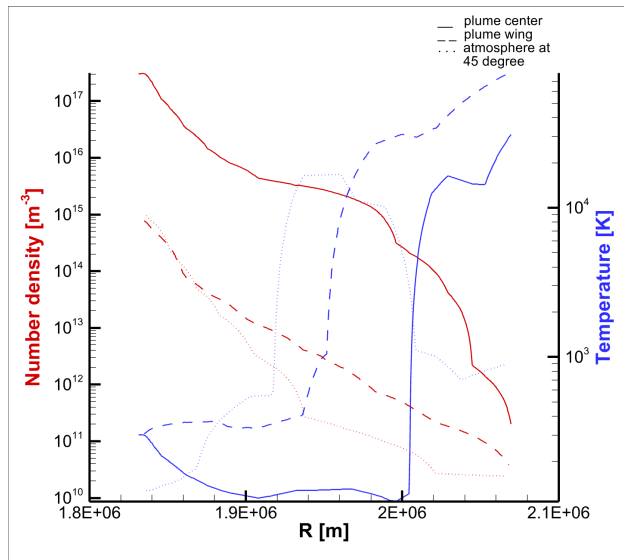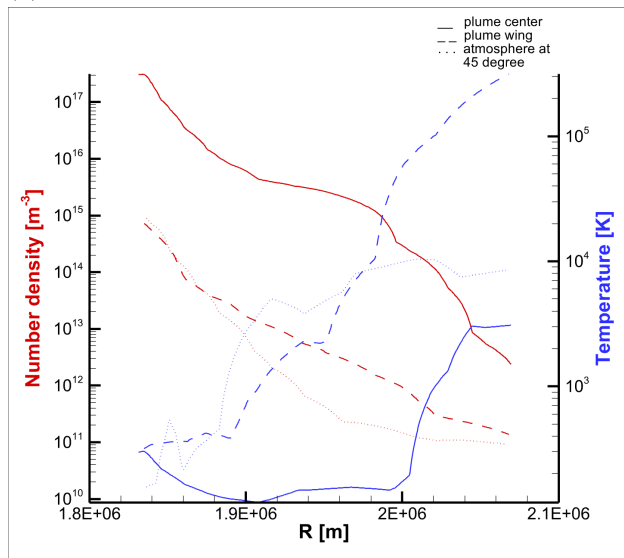
Figure 40: Vertical line profiles of the number density and tempera-
ture for different positions in the atmosphere and for dif-
ferent plasma densities of $3 \times 10^8 \mathrm{m}^{-3}$ (a), $4 \times 10^8 \mathrm{m}^{-3}$ (b)
and $5 \times 10^8 \mathrm{m}^{-3}$ (c) with a plasma velocity of 15km/s and
temperature of 150eV.
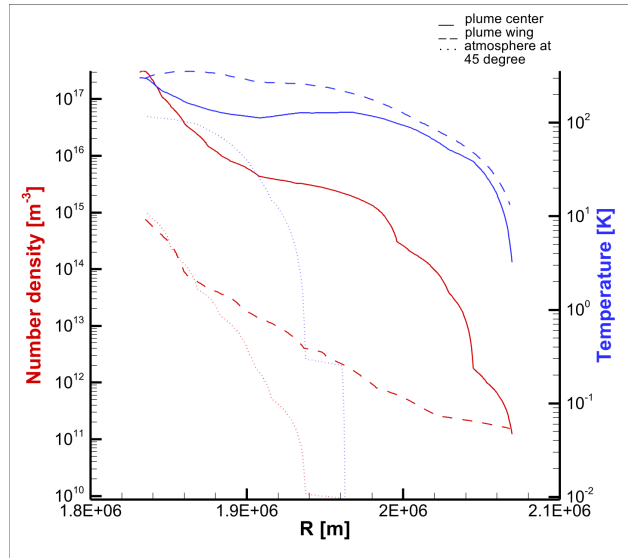
(a)
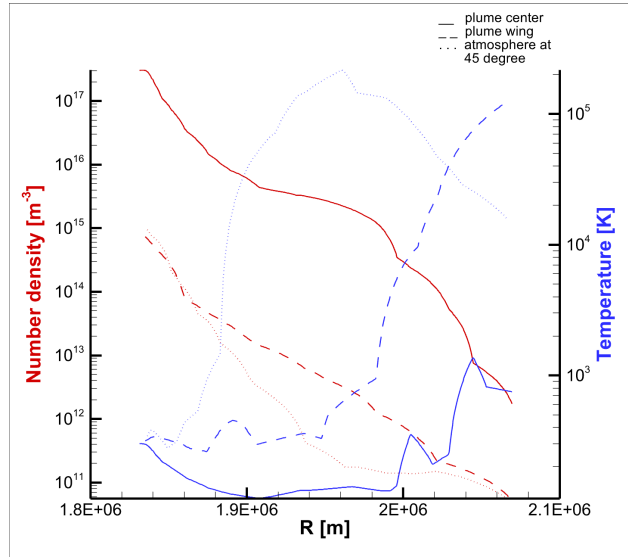
(b)
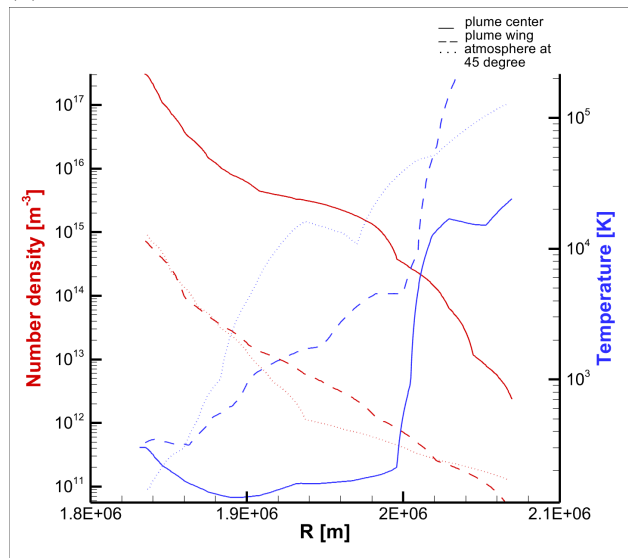
(c)

Figure 41: Vertical line profiles of the number density and temperature for different positions in the atmosphere and for different plasma densities of $1 \times 10^8 \mathrm{m}^{-3}$ (a), $5 \times 10^8 \mathrm{m}^{-3}$ (b) and $1 \times 10^9 \mathrm{m}^{-3}$ (c) with a plasma velocity of 45km/s and temperature of 150eV.

DUST RESULTS

In this chapter the behaviour of dust in the simulations with SO_2 plumes will be studied. For the dust dynamics presented here the gas flow field of a single plume into vacuum and the flow field of two plumes into a day side atmosphere were used to calculate trajectories of dust particles ranging in size from 1nm to 100μm. Since the dust sizes stay $< 2 \times 10-4$ the calculations of the reflectance images are done applying Mie theory.

10.1 DUST COLUMN DENSITY

Figures 42 and 43 show the column density of the dust result for the different dust sizes and display the dust flow controlled by gas drag and gravity. The single plume has a surface temperature of 500K and an outflow velocity of 850m/s for the gas particles whereas the plumes in the second case have a surface temperature of 300K and a outflow velocity of 500m/s for the gas flow. Figure 43 compares the column density for different sized particles. It can be observed that as particle size increases the column density in the center of the plume increases but the canopy of the plume fades and eventually disappears.

Column density plots can also be important for the comparison to observational data. However, caution must be exercised since observations do not differentiate between condensates and ash particles (dust). Here observations of Voyager 1 of Pele in the UV and a plot of the UV brightness contours ([73]) are shown in figure 44 and compared to the dust flow field results. The column density plot of plumes with the smallest dust particles in figure 43 feature a distinct canopy shape and a high density region in the plume center which correlates with the features of the Pele observation and seem as the closest match for the whole plume structure. However, the larger particles are probably a better fit for the center of the plume and for a better match of the canopy probably even smaller dust sizes are needed. This is not covered in this study since only cases with single dust sizes are displayed.

When looking at the number density and mean velocity profiles in figure 45 the indicated behaviour can be confirmed. As

expected, the smaller and lighter particles reach much higher velocities than the heavier and larger particles. Therefore, the smaller particles are carried much farther and to increased altitudes whereas the larger particles remain closer to the center of the plume. Also, particles with dust sizes $> 1\mu m$ are not visible in the results at all as the drag force is not high enough to lift them from the surface. This will change with an increase of the initial gas velocity dragging the dust.
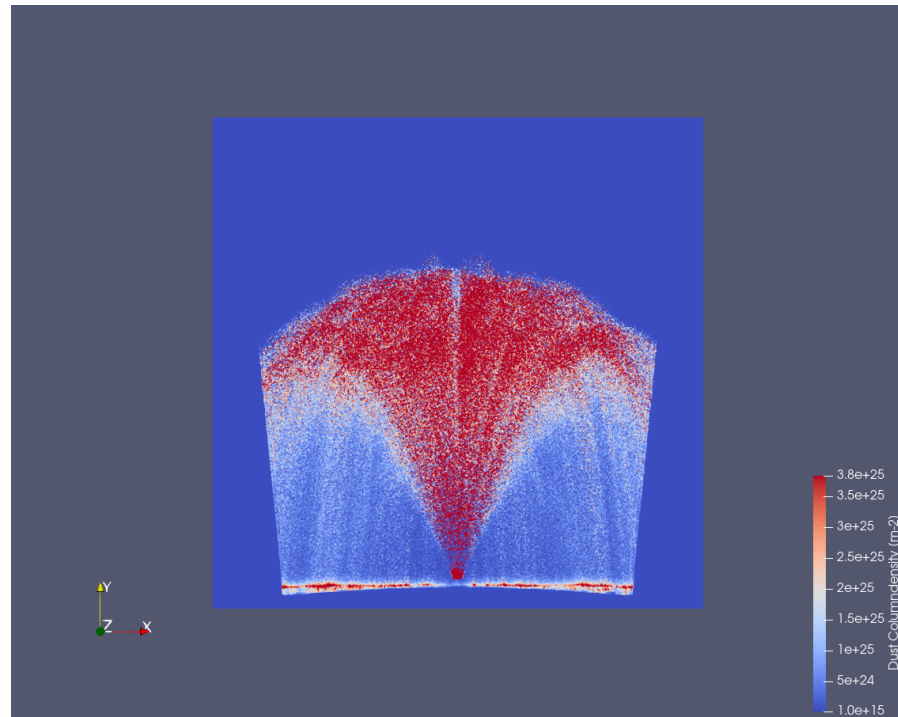
Figure 42: Dust column density of a plume into vacuum for a dust size of $10nm$.

10.2 SPECTRAL REFLECTANCE

Additionally to the main parameters and the column density integration it is also possible to look at the scattering behaviour of the dust particles and its influence on the brightness measurement. Figure 47 and figure 46 show the reflectance for particle sizes ranging from $10nm$ to $100\mu m$ whereas figure 48 shows the reflectance for particle sizes ranging from $10nm$ to $1\mu m$. Further the reflectance depends on the dust size distribution. Here a differential power law dust size distribution is assumed which can be expressed as $r_d^{-\beta}$ and is characterised by the power law exponent β. The images here display the reflectance for
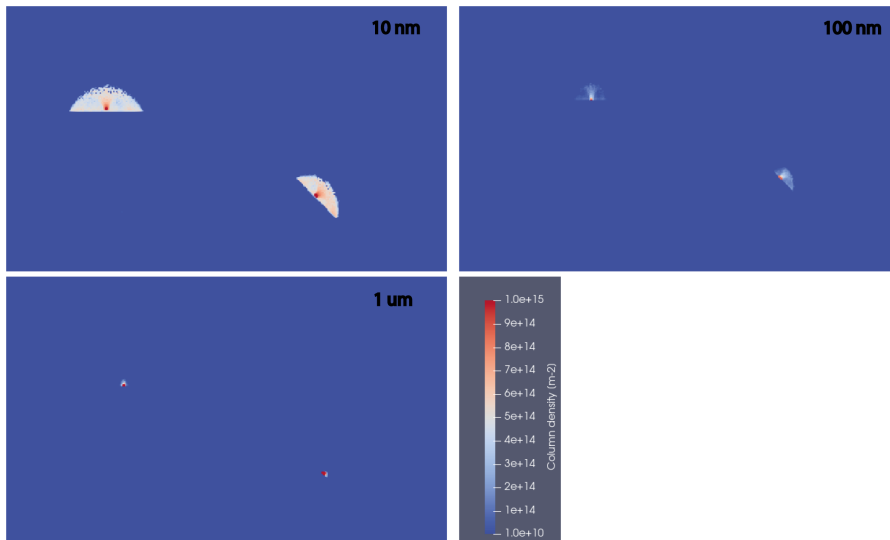
Figure 43: Dust column density of 2 plumes into a day side atmosphere for dust sizes of 10nm, 100nm and 1µm.
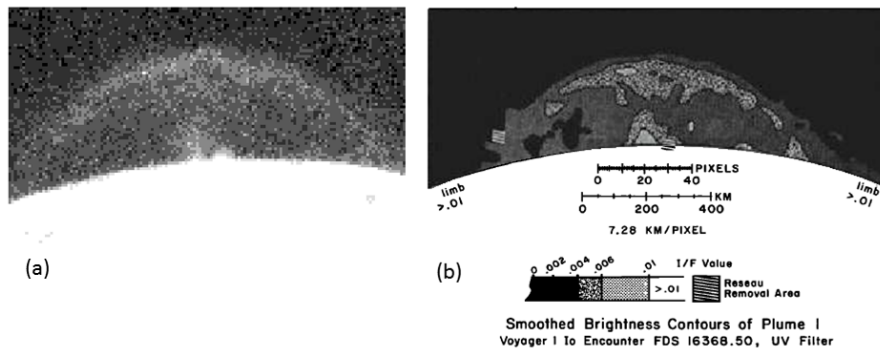
Figure 44: Voyager 1 observation of Pele in the UV (a) and UV brightness contour levels (b) from Strom et al. ([73]).

power law exponents of β = 2, 3, 4. For the lifted dust particles in all cases the brightness increases with an increasing power law exponent meaning the number of particles in the efficient scattering regime increases. This makes sense, since for a high power law exponent the smaller sized particles dominate and as seen in the section before mostly the smaller sized particles are lifted from the surface. For a low power law exponent the larger particles dominate which however do not get lifted high enough and stay in the center of the plume. Therefore, it is only possible to see the plume canopy for a higher power law exponent. Further, it must be considered that the power law exponent is set at the surface. This influences the dust size distribution since the smaller particles are accelerated more compared
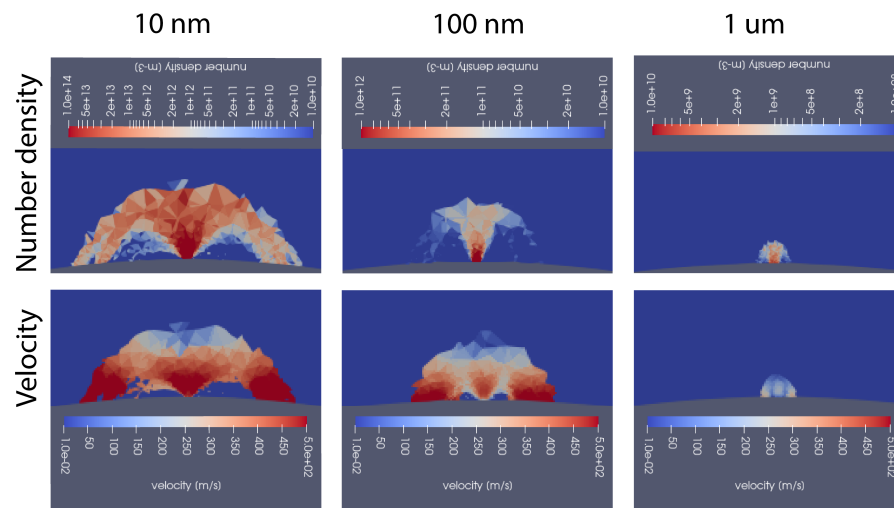
Figure 45: The dust mean speed and number density of the center plume for particle sizes of 10nm, 100nm and 1μm.

to the larger particles which leads to a dilution of the smaller particles and a change in the power law ([52]).
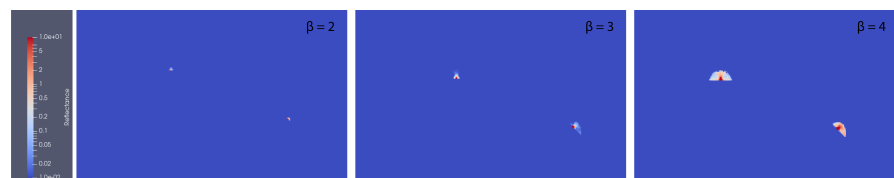
Figure 46: The dust reflectance of 2 plumes into a day side atmosphere for a particle range of 10nm − 100μm and different power law exponents 2, 3 and 4.

(a)

(b)

(c)
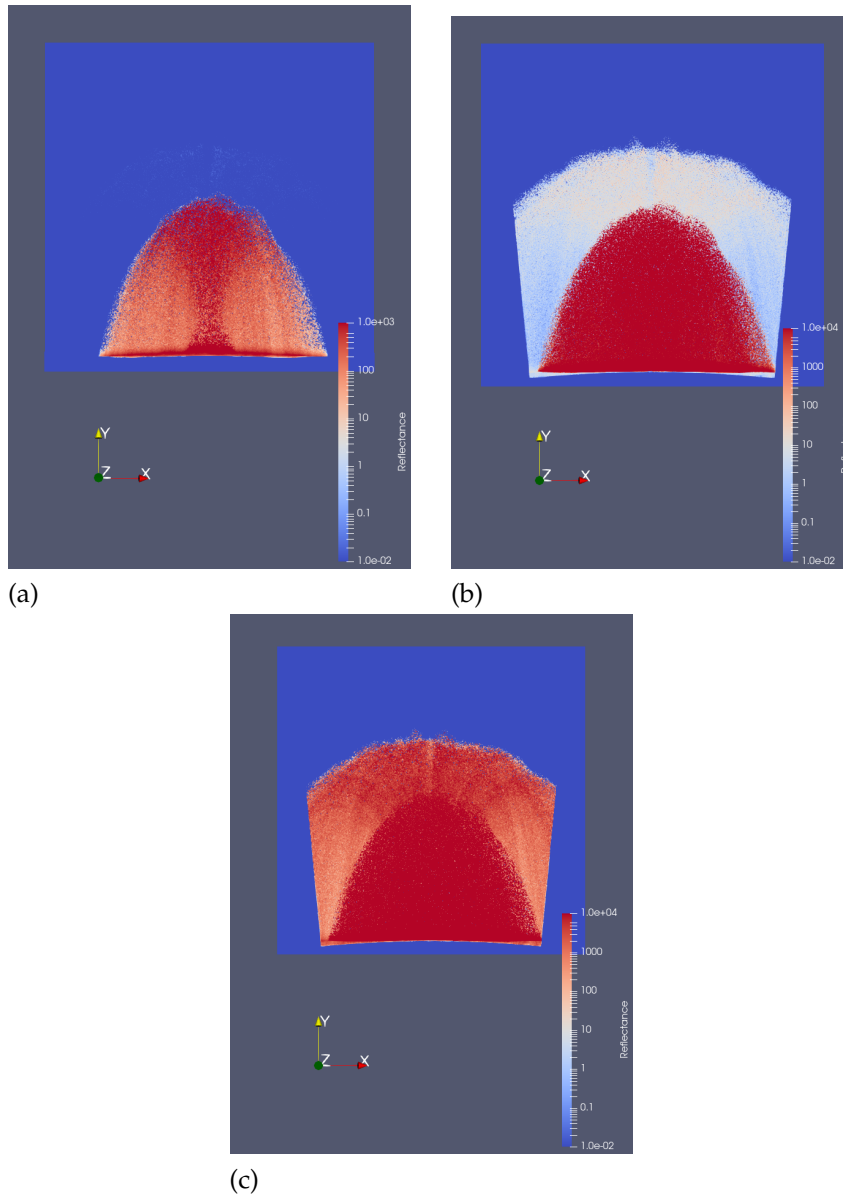
Figure 47: The dust reflectance of a single plume into vacuum for a particle range of $10\,\text{nm} - 100\,\mu\text{m}$ and different power law exponents 2 (a), 3 (b) and 4 (c.)
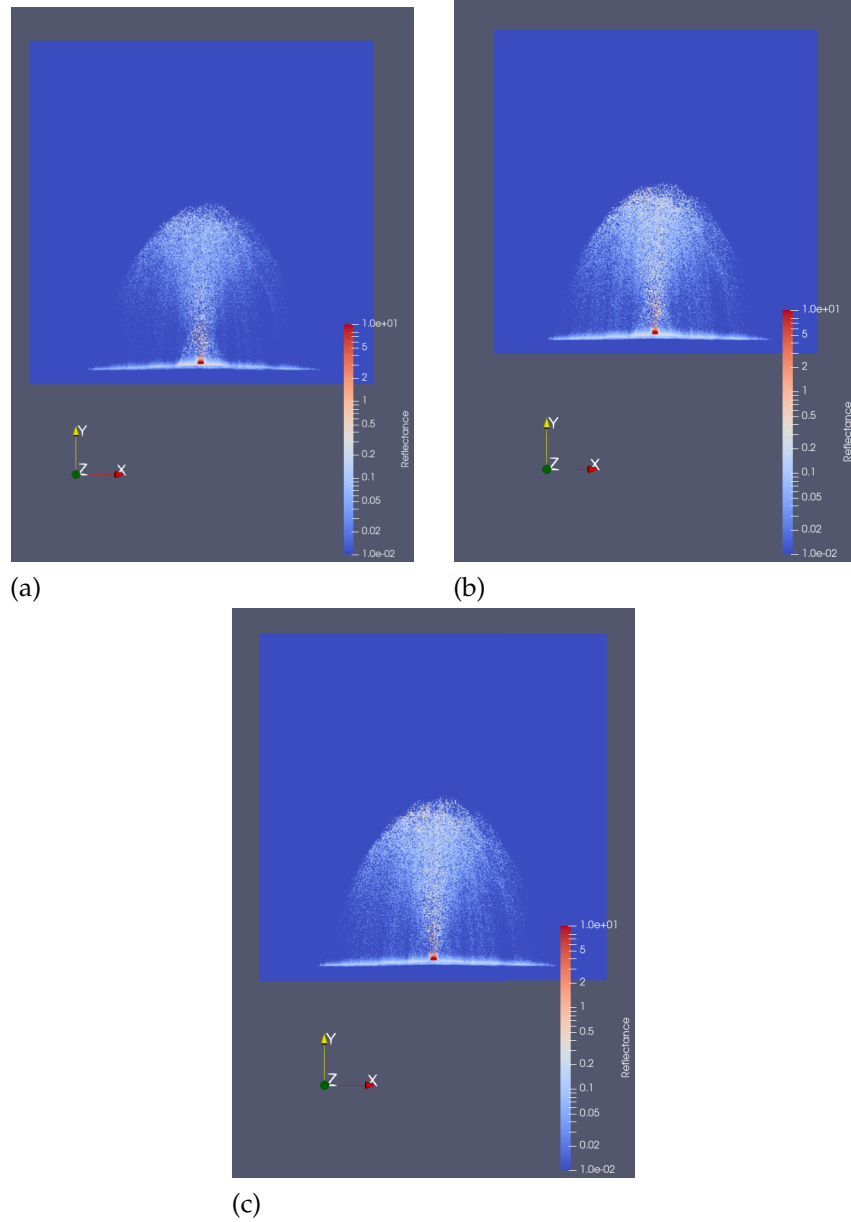
Figure 48: The dust reflectance of a single plume into vacuum for a particle range of $10 \text{nm} - 1 \mu \text{m}$ and different power law exponents 2 (a), 3 (b) and 4 (c)

Part IV

DISCUSSION AND OUTLOOK

In the following part the outcomes of the study will be discussed and future additions and plans will be illustrated.

11

SUMMARY AND DISCUSSION

In the course of this study a three dimensional DSMC model of the atmosphere of Io could be constructed. Further, investigations of dust and gas flows can be performed and the effects and interactions of different atmospheric processes can be analysed. With this model it is possible to perform parameter studies of different atmospheric effects on a basic level on a local machine relatively time efficient. The final model contains the following components:

1. Sublimation: The sublimation of SO_2 surface frost deposits can be simulated on different levels. It can be modelled either by applying a simple, uniform outgassing surface or by calculating a thermal model from the solar illumination and a surface frost distribution resulting in a detailed surface map of temperature and gas production rate. However, the second approach is still very computationally expensive.

2. Volcanic activity: Volcanic plumes can be distributed over the surface by setting a source geometry and the inlet boundary condition.

3. Plasma heating: The effect of plasma heating can be modelled by inserting gas particles from the outlet boundary and generating the heating effect through enhanced particle collisions. The parameters of the plasma particles can be varied and their effect is studied.

4. Species: The DSMC code can be used with several species. Currently, cases with SO_2 and O_2 have been performed, however studies with different minor species of Io's atmosphere are possible and can be approached in the future.

5. Dust: The resulting gas flow field can be used to insert into a dust calculation model which returns a dust flow field with variable dust sizes and particle size distributions.

Further, the model was computed for several cases and several conclusions could be made:

1. In order for the sublimation atmosphere to reach an increased exobase, additional processes as plumes or plasma heating must be added.

2. In the case of adding O_2 to the model, the density should be $> 2 \times 10^{15} m^{-3}$. It can add the non-condensable atmosphere on the night side. Further, in this model the O_2 should be inserted through an inflow condition rather than as a background gas. The results show the interaction of O_2 with plasma particles on the night side mainly for the inflow particles.

3. The interaction of sublimation atmosphere and plumes is rather complex. However, plumes only seem to influence the atmosphere in their closer surroundings. Also the transport of the plume particles depends on the sublimating gas flux and surface temperature around the plume.

4. The plume structure can be generated as expected, however at the sides of a plume hot wings are generated, hot non-equilibrium regions. This effect has also been seen by Zhang et al. ([105]). It could be explained by the cooled falling particles which fall into a low density region and collide with radially expanding particles from the plume and sublimating particles from the surface. The three different modes in the velocity distribution represented by a single kinetic temperature based on the mean velocity results in a high temperature. Further, the horizontal motion of the gas away from the plume at velocities of $\sim 300 m/s$ aligns with measurements of winds from disk-resolved millimetre observations by Moullet et al. ([62]).

5. Plasma heating in interaction with plumes depends on the location of the plume. In general, a plume seems to regulate the influence of the plasma heating on the atmosphere. However, the plasma warms the material from he canopy creating hotter regions above the plume. Also, when interacting with incoming plasma particles, the heating effect at the sides of the plume seems to be suppressed.

6. Plasma heating of a sublimation atmosphere leads to an enhancement of the number density and temperature when

the plasma densities are $> 1 \times 10^8 \mathrm{m}^{-3}$ and the plasma velocity $> 15 \mathrm{km/s}$ at a height of $\sim 250 \mathrm{km}$ from the surface. The plasma particles can therefore increase the exobase and inflate the atmosphere.

7. The behaviour of the dust flow in a plume depends on the dust size and the gas flow. Particles with smaller sizes ($\sim 10 - 100 \mathrm{nm}$) get dragged by the gas flow and follow its motion through the plume, forming a visible canopy. Larger grains either don't get lifted from the surface or decouple from the gas flow as soon as the gas density decreases and stay in the center of the plume.

OUTLOOK AND FUTURE WORK

The results shown here can be extended in various ways by performing different simulations using the same methods or by implementing further methods or processes in the model. Some examples could be:

1. A revised version of the sublimation atmosphere from thermal model calculations would be very convenient for further studies. It would need to be a compressed version of the one currently available to improve the computational run time with a more detailed inlet surface.

2. The influence of not only O_2 but also other minor species in Io's atmosphere could be studied by expanding the number of species available in the model.

3. Chemical reactions especially with regard to the plasma interaction would be interesting to study. Probably the gradual implementation of different processes would be the most promising.

4. Further plume simulations also in closer interaction with each other would be interesting and could provide data to compare to future plume observations.

5. Also another closer look at the hot wings and the winds from the expanding plume material would be interesting in comparison with observational data.

6. Simulations with plasma not only as neutrals but also as ions and electrons could give an insight on how material is lost from Io's atmosphere.

7. The calculation of the vertical column density and a disk integrated column density would be a valuable result in comparison to observations by Atacama Large Millimeter/Submillitmeter Array (ALMA).

The combination of more detailed processes could provide useful insights in the future, however it should also be handled with care since the more complex the model the more complex

physical effects occur which make the results more difficult to interpret. Therefore, a gradual extension of the model would be the best. Also, every extension of the modelled processes comes with an increase in the computational power needed.

Part V

APPENDIX

APPENDIX

A.1 APPENDIX A: COSINE LAW VELOCITY DISTRIBUTION FUNCTION

The initial velocity distribution function (VDF) of the gas at the surface is complex and influenced by many unknown factors. During this study two methods to describe the VDF were analysed. The first method, which was favoured for the results shown in the thesis, involves the assumption of a half-Maxwellian velocity distribution based on the surface temperature and is a common and sufficient way to specify the initial outflow conditions. The second method employs a cosine law distribution, where the angle to the surface normal (θ) follows:

$$f(\theta) \propto \cos^n(\theta) \tag{23}$$

with n being an integral exponent ($n \geqslant 1$). This distribution is considered more realistic for thin-film evaporation compared to a simple $\cos(\theta)$ dependence ([67]). The diagram in Figure 49 illustrates how the exponent n shapes the geometry of the evaporated flux, considering insights from Greenwood et al. ([26]) on the proper construction of the boundary condition.

In this study the cosine law velocity distribution was tested for the outflow velocity of a volcanic plume into vacuum. Figure 50 shows a SO_2 plume into vacuum with a density of $6 \times 10^{16} m-3$, a temperature of 850K and a velocity of 500m/s following the cosine law velocity distribution function for an exponent of 8. In comparison to figure 23 this plume doesn't follow the typical plume structure which would be expected. It resembles more a outflow nozzle than the typical plume structure. In the frame of this study it was decided to not apply the cosine law velocity distribution function, but in future this might be something to investigate further.

A.2 APPENDIX B: SPECIES VARIABLES

The following tables display the needed specifications of different species for the DSMC simulation.
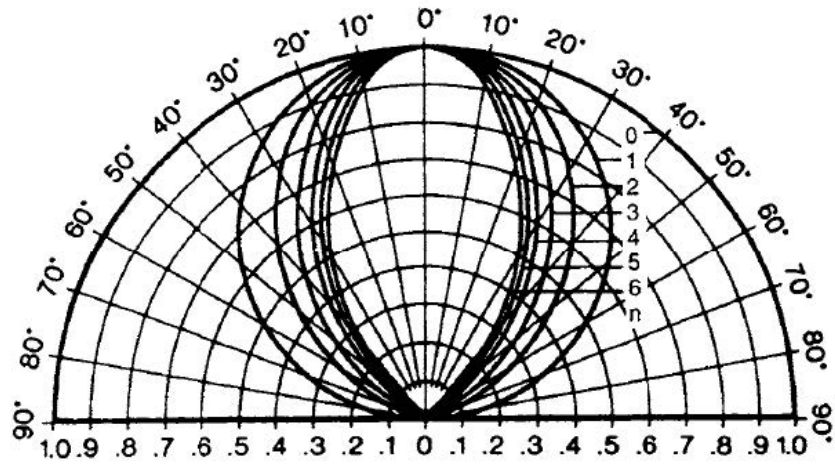
Figure 49: The angular distribution of gas outflow following different cosine law exponent ([72]).

(a)   (b)
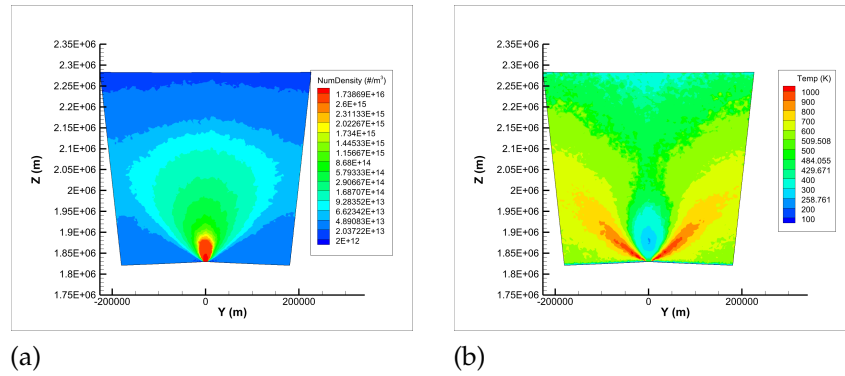
Figure 50: Two dimensional slices through the 3D simulation domain of the number density (a) and temperature (b) field for a SO_2 plume into vacuum with a outflow velocity following the cosine law velocity distribution function.

PARAMETER	SO_2	O_2	SO	S_2	S
diameter (m)	$7.16e-10$	$4.07e-10$	$4.19e-10$	$5.0e-10$	$3.0e-10$
mass (kg)	$1.06e-25$	$5.31e-26$	$7.993-26$	$1.07e-25$	$5.33e-26$
rotational DOF	3	1	1	1	0
VHS T_{ref} (K)	273	273	273	273	273
VHS Viscosity Coef.	1.05	0.77	0.77	0.77	0.67
VSS Parameter	0.968	1	1	1	1
Number of Vib. Modes	3	1	1	1	0
Vib. Modes (1,2,3)	1656, 745, 1960	2256	2500	2500	—
char. dissociation T	65705	59500	62745	50225	0

Table 9: Species parameters

[1] J Austin and David B. Goldstein. "Rarefied Gas Model of Io's Sublimation-Driven Atmosphere." In: *Icarus* 148.2 (2000), p. 370383. ISSN: 0019-1035. DOI: 10.1006/icar.2000.6466.

[2] Fran Bagenal, James D. Sullivan, and George L. Siscoe. "Spatial distribution of plasma in the Io torus." In: *Geophysical Research Letters* 7.1 (1980), p. 4144. ISSN: 1944-8007. DOI: 10.1029/gl007i001p00041.

[3] G.E. Ballester, M.A. Mcgrath, D.F. Strobel, Xun Zhu, P.D. Feldman, and H.W. Moos. "Detection of the SO2 Atmosphere on Io with the Hubble Space Telescope." In: *Icarus* 111.1 (1994), p. 217. ISSN: 0019-1035. DOI: 10.1006/icar.1994.1129.

[4] H. E. Bass, T. G. Winter, and L. B. Evans. "Vibrational and Rotational Relaxation in Sulfur Dioxide." In: *The Journal of Chemical Physics* 54.2 (1971), p. 644647. ISSN: 1089-7690. DOI: 10.1063/1.1674890.

[5] A Binder and D Cruikshank. "Evidence for an atmosphere on Io." In: *Icarus* 3.4 (1964), p. 299305. ISSN: 0019-1035. DOI: 10.1016/0019-1035(64)90038-7.

[6] G.A. Bird. *Molecular Gas Dynamics and the Direct Simulation of Gas Flows*. Clarendon Press, Oxford Engineering Science Series, 1994.

[7] Craig F. Bohren and Donald R. Huffman. *Absorption and Scattering of Light by Small Particles*. Wiley, 1998. ISBN: 9783527618156. DOI: 10.1002/9783527618156.

[8] H. S. Bridge et al. "Plasma Observations Near Jupiter: Initial Results from Voyager 1." In: *Science* 204.4396 (1979), p. 987991. ISSN: 1095-9203. DOI: 10.1126/science.204.4396.987.

[9] A. L. Broadfoot et al. "Extreme Ultraviolet Observations from Voyager 1 Encounter with Jupiter." In: *Science* 204.4396 (1979), p. 979982. ISSN: 1095-9203. DOI: 10.1126/science.204.4396.979.

[10]   R. W. Carlson et al. "The distribution of sulfur dioxide and other infrared absorbers on the surface of Io." In: 24.20 (1997), pp. 2479–2482. DOI: 10.1029/97GL02609.

[11]   John T. Clarke, Joe Ajello, Janet Luhmann, Nick Schneider, and Isik Kanik. "Hubble Space Telescope UV spectral observations of Io passing into eclipse." In: *Journal of Geophysical Research: Planets* 99.E4 (1994), p. 83878402. ISSN: 0148-0227. DOI: 10.1029/93je02547.

[12]   M. R. Combi, K. Kabin, T. I. Gombosi, D. L. DeZeeuw, and K. G. Powell. "Io's plasma environment during the Galileo flyby: Global three dimensional MHD modeling with adaptive mesh refinement." In: *Journal of Geophysical Research: Space Physics* 103.A5 (1998), p. 90719081. ISSN: 0148-0227. DOI: 10.1029/98ja00073.

[13]   J.-F. Crifo, G.A. Loukianov, A.V. Rodionov, and V.V. Zakharov. "Direct Monte Carlo and multifluid modeling of the circumnuclear dust coma." In: *Icarus* 176.1 (2005), p. 192219. ISSN: 0019-1035. DOI: 10.1016/j.icarus.2005.01.003.

[14]   D.P. Cruikshank and Robert E. Murphy. "The post-eclipse brightening of Io." In: *Icarus* 20.1 (1973), p. 717. ISSN: 0019-1035. DOI: 10.1016/0019-1035(73)90033-x.

[15]   Ashley Gerard Davies, Laszlo P. Keszthelyi, David A. Williams, Cynthia B. Phillips, Alfred S. McEwen, Rosaly M. C. Lopes, William D. Smythe, Lucas W. Kamp, Laurence A. Soderblom, and Robert W. Carlson. "Thermal signature, eruption style, and eruption evolution at Pele and Pillan on Io." In: *Journal of Geophysical Research: Planets* 106.E12 (2001), p. 3307933103. ISSN: 0148-0227. DOI: 10.1029/2000je001357.

[16]   Lionel ; Matson Dennis ; Leone Giovanni ; Keszthelyi Laszlo ; Jaeger Windy Davies Ashley Gerard ; Wilson. "The heartbeat of the volcano: The discovery of episodic activity at Prometheus on Io." In: *Icarus* 184.2 (2006), p. 460477. ISSN: 0019-1035. DOI: 10.1016/j.icarus.2006.05.012.

[17]   S Douté. "Mapping SO2 Frost on Io by the Modeling of NIMS Hyperspectral Images." In: *Icarus* 149.1 (2001), p. 107132. ISSN: 0019-1035. DOI: 10.1006/icar.2000.6513.

[18] Frederick W. Fallon and Robert E. Murphy. "Absence of post-eclipse brightening of Io and Europa in 1970." In: *Icarus* 15.3 (1971), p. 492496. ISSN: 0019-1035. DOI: 10.1016/0019-1035(71)90127-8.

[19] Lori Feaga, Melissa McGrath, and Paul Feldman. "Io's dayside SO2 atmosphere." In: *Icarus* 201 (2009), pp. 570–584. DOI: 10.1016/j.icarus.2009.01.029.

[20] Paul D. Feldman, Darrell F. Strobel, H. Warren Moos, Kurt D. Retherford, Brian C. Wolven, Melissa A. McGrath, Fred L. Roesler, R. Carey Woodward, Ronald J. Oliversen, and Gilda E. Ballester. "Lyman-α imaging of the SO2 distribution on Io." In: *Geophysical Research Letters* 27.12 (2000), p. 17871790. ISSN: 0094-8276. DOI: 10.1029/1999gl011067.

[21] Susanne Finklenburg. "Investigations of the Near Nucleus Gas and Dust Coma of Comets." PhD thesis. University of Bern, 2014.

[22] L. A. Frank, W. R. Paterson, K. L. Ackerson, V. M. Vasyliunas, F. V. Coroniti, and S. J. Bolton. "Plasma Observations at Io with the Galileo Spacecraft." In: *Science* 274.5286 (1996), p. 394395. ISSN: 1095-9203. DOI: 10.1126/science.274.5286.394.

[23] P.E. Geissler, A.S. McEwen, L. Keszthelyi, R. Lopes-Gautier, J. Granahan, and D.P. Simonelli. "Global Color Variations on Io." In: *Icarus* 140.2 (1999), p. 265282. ISSN: 0019-1035. DOI: 10.1006/icar.1999.6128.

[24] P.E. Geissler and M.T. McMillan. "Galileo observations of volcanic plumes on Io." In: *Icarus* 197.2 (2008), p. 505518. ISSN: 0019-1035. DOI: 10.1016/j.icarus.2008.05.005.

[25] S.-B. Gerig, O. Pinzon-Rodriguez, R. Marschall, J.-S. Wu, and N. Thomas. "Dayside-to-nightside dust coma brightness asymmetry and its implications for nightside activity at Comet 67P/Churyumov-Gerasimenko." In: *Icarus* 351 (2020), p. 113968. ISSN: 0019-1035. DOI: 10.1016/j.icarus.2020.113968.

[26] John Greenwood. "The correct and incorrect generation of a cosine distribution of scattered particles for Monte-Carlo modelling of vacuum systems." In: *Vacuum* 67.2 (2002), p. 217222. ISSN: 0042-207X. DOI: 10.1016/s0042-207x(02)00173-2.

[27] Leo Haser. "Distribution d'intensité dans la tête d'une comète." In: *Bulletin de la Classe des Sciences de l'Académie Royale de Belgique, vol. 43, p. 740-750* (1957).

[28] R.R. Howell, D.P. Cruikshank, and F.P. Fanale. "Sulfur dioxide on Io: Spatial distribution and physical state." In: *Icarus* 57.1 (1984), p. 8392. ISSN: 0019-1035. DOI: 10.1016/0019-1035(84)90010-1.

[29] A Ingersoll. "Io meteorology: How atmospheric pressure is controlled locally by volcanos and surface frosts." In: *Icarus* 81.2 (1989), p. 298313. ISSN: 0019-1035. DOI: 10.1016/0019-1035(89)90055-9.

[30] Andrew P. Ingersoll, Michael E. Summers, and Steve G. Schlipf. "Supersonic meteorology of Io: Sublimation-driven flow of SO2." In: *Icarus* 64.3 (1985), p. 375390. ISSN: 0019-1035. DOI: 10.1016/0019-1035(85)90062-4.

[31] Kandis Lea Jessup and John R. Spencer. "Characterizing Io's Pele, Tvashtar and Pillan plumes: Lessons learned from Hubble." In: *Icarus* 218.1 (2012), p. 378405. ISSN: 0019-1035. DOI: 10.1016/j.icarus.2011.11.013.

[32] Kandis Lea Jessup, John R. Spencer, Gilda E. Ballester, Robert R. Howell, Fred Roesler, Miquela Vigel, and Roger Yelle. "The atmospheric signature of Io's Prometheus plume and anti-jovian hemisphere: evidence for a sublimation atmosphere?" In: *Icarus* 169.1 (2004), p. 197215. ISSN: 0019-1035. DOI: 10.1016/j.icarus.2003.11.015.

[33] Kandis Lea Jessup, John Spencer, and Roger Yelle. "Sulfur volcanism on Io." In: *Icarus* 192.1 (2007), p. 2440. ISSN: 0019-1035. DOI: 10.1016/j.icarus.2007.06.025.

[34] K. Kabin, M.R. Combi, T.I. Gombosi, D.L. DeZeeuw, K.C. Hansen, and K.G. Powell. "Io's magnetospheric interaction: an MHD model with day-night asymmetry." In: *Planetary and Space Science* 49.34 (2001), p. 337344. ISSN: 0032-0633. DOI: 10.1016/s0032-0633(00)00155-0.

[35] H. U. Keller et al. "OSIRIS - The Scientific Camera System Onboard Rosetta." In: *Space Science Reviews* 128.14 (2007), p. 433506. ISSN: 1572-9672. DOI: 10.1007/s11214-006-9128-4.

[36] C. R. Kerton, F. P. Fanale, and J. R. Salvail. "The state of SO2 on Io's surface." In: *Journal of Geophysical Research: Planets* 101.E3 (1996), p. 75557563. ISSN: 0148-0227. DOI: 10.1029/95je03700.

[37]   Margaret G. Kivelson, Krishan K. Khurana, Christopher T. Russell, Steven P. Joy, Martin Volwerk, Raymond J. Walker, Christophe Zimmer, and Jon A. Linker. "Magnetized or unmagnetized: Ambiguity persists following Galileo's encounters with Io in 1999 and 2000." In: *Journal of Geophysical Research: Space Physics* 106.A11 (2001), p. 2612126135. ISSN: 0148-0227. DOI: 10.1029/2000ja002510.

[38]   A.J. Kliore, G. Fjeldbo, B.L. Seidel, D.N. Sweetnam, T.T. Sesplaukis, P.M. Woiceshyn, and S.I. Rasool. "The atmosphere of Io from Pioneer 10 radio occultation measurements." In: *Icarus* 24.4 (1975), p. 407410. ISSN: 0019-1035. DOI: 10.1016/0019-1035(75)90057-3.

[39]   Katsuhisa Koura and Hiroaki Matsumoto. "Variable soft sphere molecular model for inverse-power-law or Lennard-Jones potential." In: *Physics of Fluids A: Fluid Dynamics* 3.10 (1991), p. 24592465. ISSN: 0899-8213. DOI: 10.1063/1.858184.

[40]   Conor Laver and Imke Pater. "The global distribution of sulfur dioxide ice on Io, observed with OSIRIS on the W.M. Keck telescope." In: *Icarus* 201 (2009), pp. 172–181. DOI: 10.1016/j.icarus.2008.12.037.

[41]   Conor Laver and Imke de Pater. "Spatially resolved SO2 ice on Io, observed in the near IR." In: *Icarus* 195.2 (2008), p. 752757. ISSN: 0019-1035. DOI: 10.1016/j.icarus.2007.12.023.

[42]   Emmanuel Lellouch, Michael Belton, Imke De Pater, Gabriel Paubert, Samuel Gulkis, and Therese Encrenaz. "The structure, stability, and global distribution of Io's atmosphere." In: *Icarus* 98.2 (1992), p. 271295. ISSN: 0019-1035. DOI: 10.1016/0019-1035(92)90095-o.

[43]   Emmanuel Lellouch, Michael Belton, Imke de Pater, Samuel Gulkis, and Therese Encrenaz. "Io's atmosphere from microwave detection of SO2." In: *Nature* 346.6285 (1990), p. 639641. ISSN: 1476-4687. DOI: 10.1038/346639a0.

[44]   J. A. Linker, M. G. Kivelson, and R. J. Walker. "A three dimensional MHD simulation of plasma flow past Io." In: *Journal of Geophysical Research: Space Physics* 96.A12 (1991), p. 2103721053. ISSN: 0148-0227. DOI: 10.1029/91ja02132.

[45] Jon A. Linker, Margaret G. Kivelson, and Raymond J. Walker. "An MHD simulation of plasma flow past Io: Alfven and slow mode perturbations." In: *Geophysical Research Letters* 15.11 (1988), p. 13111314. ISSN: 1944-8007. DOI: 10.1029/gl015i011p01311.

[46] Johannes Markkanen and Jessica Agarwal. "Scattering, absorption, and thermal emission by large cometary dust particles: Synoptic numerical solution." In: *Astronomy & Astrophysics* 631 (2019), A164. ISSN: 1432-0746. DOI: 10.1051/0004-6361/201936235.

[47] Johannes Markkanen, Jessica Agarwal, Timo Väisänen, Antti Penttilä, and Karri Muinonen. "Interpretation of the Phase Functions Measured by the OSIRIS Instrument for Comet 67P/Churyumov-Gerasimenko." In: *The Astrophysical Journal* 868.1 (2018), p. L16. ISSN: 2041-8213. DOI: 10.3847/2041-8213/aaee10.

[48] R. Marschall et al. "Modelling observations of the inner gas and dust coma of comet 67P/Churyumov-Gerasimenko using ROSINA/COPS and OSIRIS data: First results." In: *Astronomy & Astrophysics* 589 (2016), A90. ISSN: 1432-0746. DOI: 10.1051/0004-6361/201628085.

[49] William J. McDoniel, David B. Goldstein, Philip L. Varghese, and Laurence M. Trafton. "Three-dimensional simulation of gas and dust in Io's Pele plume." In: *Icarus* 257 (2015), pp. 251 –274. ISSN: 0019-1035. DOI: https://doi.org/10.1016/j.icarus.2015.03.019. URL: http://www.sciencedirect.com/science/article/pii/S0019103515001190.

[50] William J. McDoniel, David B. Goldstein, Philip L. Varghese, and Laurence M. Trafton. "The interaction of Io's plumes and sublimation atmosphere." In: *Icarus* 294 (2017), pp. 81–97. DOI: 10.1016/j.icarus.2017.04.021.

[51] William J. McDoniel, David B. Goldstein, Philip L. Varghese, and Laurence M. Trafton. "Simulation of Io's plumes and Jupiter's plasma torus." In: *Physics of Fluids* 31.7, 077103 (2019), p. 077103. DOI: 10.1063/1.5097961.

[52] J. A. M. McDonnell et al. "The dust distribution within the inner coma of comet P/Halley 1982i: encounter by Giotto's impact detectors." In: *Exploration of Halley's Comet*. Springer Berlin Heidelberg, 1987, p. 719741. DOI: 10.1007/978-3-642-82971-0_127.

[53]   A. S. McEwen et al. "Galileo at Io: Results from High-Resolution Imaging." In: *Science* 288.5469 (2000), p. 11931198. ISSN: 1095-9203. DOI: `10.1126/science.288.5469.1193`.

[54]   Alfred S. McEwen, Torrence V. Johnson, Dennis L. Matson, and Laurence A. Soderblom. "The global distribution, abundance, and stability of SO2 on Io." In: *Icarus* 75.3 (1988), p. 450478. ISSN: 0019-1035. DOI: `10.1016/0019-1035(88)90157-1`.

[55]   Alfred S. McEwen and Laurence A. Soderblom. "Two classes of volcanic plumes on Io." In: *Icarus* 55.2 (1983), p. 191217. ISSN: 0019-1035. DOI: `10.1016/0019-1035(83)90075-1`.

[56]   Melissa McGrath, Michael Belton, John Spencer, and Paola Sartoretti. "Spatially Resolved Spectroscopy of Io's Pele Plume and SO2 Atmosphere." In: *Icarus* 146.2 (2000), p. 476493. ISSN: 0019-1035. DOI: `10.1006/icar.1999.6412`.

[57]   Laszlo P. ; Radebaugh Jani ; Davies Ashley G. ; Turtle Elizabeth P. ; Geissler Paul ; Klaasen Kenneth P. ; Rathbun Julie A. ; McEwen Alfred S. Milazzo Moses P. ; Keszthelyi. "Volcanic activity at Tvashtar Catena, Io." In: *Icarus* 179.1 (2005), p. 235251. ISSN: 0019-1035. DOI: `10.1016/j.icarus.2005.05.013`.

[58]   R. B. Minton. "The red polar caps of Io." In: *Communications of the Lunar and Planetary Laboratory* Volume 10 (1973). Part 1, p.35–39.

[59]   C.H. Moore, D.B. Goldstein, P.L. Varghese, L.M. Trafton, and B. Stewart. "1-D DSMC simulation of Io's atmospheric collapse and reformation during and after eclipse." In: *Icarus* 201.2 (2009), p. 585597. ISSN: 0019-1035. DOI: `10.1016/j.icarus.2009.01.006`.

[60]   S. P. ; Kupferman P. N. ; Collins S. A. Morabito L. A. ; Synnott. "Discovery of Currently Active Extraterrestrial Volcanism." In: *Science* 204.4396 (1979), p. 972972. ISSN: 1095-9203. DOI: `10.1126/science.204.4396.972`.

[61]   Miguel A. Moreno, Gerald Schubert, John Baumgardner, Margaret G. Kivelson, and David A. Paige. "Io's volcanic and sublimation atmospheres." In: *Icarus* 93.1 (1991), p. 6381. ISSN: 0019-1035. DOI: `10.1016/0019-1035(91)90164-o`.

[62]   A. Moullet, E. Lellouch, R. Moreno, M. A. Gurwell, and C. Moore. "First disk-resolved millimeter observations of Io's surface and SO2 atmosphere." In: *Astronomy & Astrophysics* 482.1 (2008), p. 279292. ISSN: 1432-0746. DOI: 10.1051/0004-6361:20078699.

[63]   D. B. Nash, F. P. Fanale, and R. M. Nelson. "SO2 Frost: UV-visible reflectivity and Io surface coverage." In: *Geophysical Research Letters* 7.9 (1980), p. 665668. ISSN: 1944-8007. DOI: 10.1029/gl007i009p00665.

[64]   D.B. Nash and T.V. Johnson. "Albedo distribution on Io's surface." In: *Icarus* 38.1 (1979), p. 6974. ISSN: 0019-1035. DOI: 10.1016/0019-1035(79)90085-x.

[65]   Robert M. Nelson, Arthur L. Lane, Dennis L. Matson, Fraser P. Fanale, Douglas B. Nash, and Torrence V. Johnson. "Io: Longitudinal Distribution of Sulfur Dioxide Frost." In: *Science* 210.4471 (1980), p. 784786. ISSN: 1095-9203. DOI: 10.1126/science.210.4471.784.

[66]   Brian O'Leary and Joseph Veverka. "On the anomalous brightening of Io after eclipse." In: *Icarus* 14.2 (1971), p. 265268. ISSN: 0019-1035. DOI: 10.1016/0019-1035(71)90062-5.

[67]   Milton Ohring. *Materials Science of Thin Films: Depositon and Structure*. Academic Press, 2002.

[68]   Imke de Pater, Katherine de Kleer, and Mate Adamkovics. "High Spatial and Spectral Resolution Observations of the Forbidden 1.707 $\mu m Rovibronic SO Emissions on Io : Evidence for Widespread Stealth Volcanism$." In: *The Planetary Science Journal* 1.2 (2020), p. 29. ISSN: 2632-3338. DOI: 10.3847/psj/ab9eb1.

[69]   J. Pearl, R. Hanel, V. Kunde, W. Maguire, K. Fox, S. Gupta, C. Ponnamperuma, and F. Raulin. "Identification of gaseous SO2 and new upper limits for other gases on Io." In: *Nature* 280.5725 (1979), p. 755758. ISSN: 1476-4687. DOI: 10.1038/280755a0.

[70]   Olga Pinzon Rodriguez. "Modelling of the gas dynamics in the inner-coma and the composition of comet67P Churyumov-Gerasimenko." PhD thesis. University of Bern, 2021.

[71] M. K. Pospieszalska and R. E. Johnson. "Monte Carlo calculations of plasma ion induced sputtering of an atmosphere: SO2 ejected from Io." In: *Journal of Geophysical Research: Planets* 101.E3 (1996), p. 75657573. ISSN: 0148-0227. DOI: 10.1029/95je03650.

[72] H.K. Pulker. *Coatings on Glass*. 2nd Edition. Elsevier, 1999.

[73] H. Masursky R.G. Strom R.J. Terrile and C. Hansen. "Volcanic eruption plumes on Io." In: *Satellites of Jupiter. (A83-16226 04-91) Tucson, AZ, University of Arizona Press, 1982, p. 598-633* (1981).

[74] Jani Radebaugh, Alfred S. McEwen, Moses P. Milazzo, Laszlo P. Keszthelyi, Ashley G. Davies, Elizabeth P. Turtle, and Douglas D. Dawson. "Observations and temperatures of Io's Pele Patera from Cassini and Galileo spacecraft images." In: *Icarus* 169.1 (2004), p. 6579. ISSN: 0019-1035. DOI: 10.1016/j.icarus.2003.10.019.

[75] F. L. Roesler, H. W. Moos, R. J. Oliversen, R. C. Woodward, K. D. Retherford, F. Scherb, M. A. McGrath, W. H. Smyth, P. D. Feldman, and D. F. Strobel. "Far-Ultraviolet Imaging Spectroscopy of Io's Atmosphere with HST/STIS." In: *Science* 283.5400 (1999), p. 353357. ISSN: 1095-9203. DOI: 10.1126/science.283.5400.353.

[76] John Rumble. *CRC Handbook of Chemistry and Physics*. Taylor & Francis, 2020. ISBN: 9780367417246.

[77] Paola Sartoretti, Melissa A. McGrath, and Francesco Paresce. "Disk-Resolved Imaging of Io with the Hubble Space Telescope." In: *Icarus* 108.2 (1994), p. 272284. ISSN: 0019-1035. DOI: 10.1006/icar.1994.1062.

[78] Joachim Saur, Fritz M. Neubauer, Darrell F. Strobel, and Michael E. Summers. "Three dimensional plasma simulation of Io's interaction with the Io plasma torus: Asymmetric plasma flow." In: *Journal of Geophysical Research: Space Physics* 104.A11 (1999), p. 2510525126. ISSN: 0148-0227. DOI: 10.1029/1999ja900304.

[79] Joachim Saur, Fritz M. Neubauer, Darrell F. Strobel, and Michael E. Summers. "Interpretation of Galileo's Io plasma and field observations: Io, I24, and I27 flybys and close polar passes." In: *Journal of Geophysical Research: Space Physics* 107.A12 (2002). ISSN: 0148-0227. DOI: 10.1029/2001ja005067.

[80] Joachim Saur, Fritz Neubauer, J. Connerney, Philippe Zarka, and Margaret Kivelson. "Plasma interaction of Io with its plasma torus." In: *In: Jupiter. The planet, satellites and magnetosphere.* Ed. by Fran Bagenal, Timothy E. Dowling, and William B. McKinnon. Vol. 1. 2004, pp. 5637–560.

[81] Frederick L. Scarf, Donald A. Gurnett, and William S. Kurth. "Jupiter Plasma Wave Observations: An Initial Voyager 1 Overview." In: *Science* 204.4396 (1979), p. 991995. ISSN: 1095-9203. DOI: 10.1126/science.204.4396.991.

[82] J.V. Sengers, Y.-Y. Lin Wang, B. Kamgar-Parsi, and J.R. Dorfman. "Kinetic theory of drag on objects in nearly free molecular flow." In: *Physica A: Statistical Mechanics and its Applications* 413 (2014), p. 409425. ISSN: 0378-4371. DOI: 10.1016/j.physa.2014.06.026.

[83] Bradford A. Smith et al. "The Jupiter System Through the Eyes of Voyager 1." In: *Science* 204.4396 (1979), p. 951972. ISSN: 1095-9203. DOI: 10.1126/science.204.4396.951.

[84] J Spencer, E Lellouch, M Richter, M Lopezvalverde, K Jessup, T Greathouse, and J Flaud. "Mid-infrared detection of large longitudinal asymmetries in Io's SO atmosphere." In: *Icarus* 176.2 (2005), p. 283304. ISSN: 0019-1035. DOI: 10.1016/j.icarus.2005.01.019.

[85] John R. Spencer, Kandis Lea Jessup, Melissa A. McGrath, Gilda E. Ballester, and Roger Yelle. "Discovery of Gaseous S 2 in Io's Pele Plume." In: *Science* 288.5469 (2000), p. 12081210. ISSN: 1095-9203. DOI: 10.1126/science.288.5469.1208.

[86] Darrell F. Strobel, Xun Zhu, and Michael E. Summers. "On the Vertical Thermal Structure of Io's Atmosphere." In: *Icarus* 111.1 (1994), p. 1830. ISSN: 0019-1035. DOI: 10.1006/icar.1994.1130.

[87] Michael E. Summers and Darrell F. Strobel. "Photochemistry and Vertical Transport in Io's Atmosphere and Ionosphere." In: *Icarus* 120.2 (1996), p. 290316. ISSN: 0019-1035. DOI: 10.1006/icar.1996.0051.

[88] Valeriy Tenishev, Michael R. Combi, and Martin Rubin. "Numerical Simulation of Dust in a Cometary Coma: Application to Comet 67P/Churyumov-Gerasimenko." In: *The Astrophysical Journal* 732.2 (2011), p. 104. ISSN: 1538-4357. DOI: 10.1088/0004-637x/732/2/104.

[89] N. Thomas, F. Bagenal, T. W. Hill, and J. K. Wilson. "The Io neutral clouds and plasma torus." In: *In: Jupiter. The planet, satellites and magnetosphere.* Vol. 1. 2004, pp. 561–591.

[90] Nicolas Thomas. *An Introduction to Comets: Post-Rosetta Perspectives.* Springer International Publishing, 2020. ISBN: 9783030505745. DOI: 10.1007/978-3-030-50574-5.

[91] L. M. Trafton, J. J. Caldwell, C. Barnet, and C. C. Cunningham. "The Gaseous Sulfur Dioxide Abundance over Io's Leading and Trailing Hemispheres: HST Spectra of Io's C 1B 2–X 1A 1 Band of SO2 near 2100 Angstrom." In: *The Astrophysical Journal* 456 (1996), p. 384. ISSN: 1538-4357. DOI: 10.1086/176660.

[92] Constantine C. C. Tsang, John R. Spencer, Emmanuel Lellouch, Miguel A. López-Valverde, Matthew J. Richter, and Thomas K. Greathouse. "Io's atmosphere: Constraints on sublimation support from density variations on seasonal timescales using NASA IRTF/TEXES observations from 2001 to 2010." In: *Icarus* 217.1 (2012), pp. 277–296. DOI: 10.1016/j.icarus.2011.11.005.

[93] Andrew C. Walker, Sergey L. Gratiy, David B. Goldstein, Chris H. Moore, Philip L. Varghese, Laurence M. Trafton, Deborah A. Levin, and Bénédicte Stewart. "A comprehensive numerical simulation of Io's sublimation-driven atmosphere." In: *Icarus* 207.1 (2010), pp. 409–432. DOI: 10.1016/j.icarus.2010.01.012.

[94] Andrew C. Walker, Sergey L. Gratiy, Deborah A. Levin, David B. Goldstein, Philip L. Varghese, Laurence M. Trafton, Chris H. Moore, and Benedicte Stewart. "Modeling Io's Sublimation-Driven Atmosphere: Gas Dynamics and Radiation Emission." In: *American Institute of Physics Conference Series.* Ed. by Takashi Abe. Vol. 1084. 2008, pp. 1085–1090. DOI: 10.1063/1.3076443.

[95] Andrew C. Walker, Chris H. Moore, David B. Goldstein, Philip L. Varghese, and Laurence M. Trafton. "A parametric study of Io's thermophysical surface properties and subsequent numerical atmospheric simulations based on the best fit parameters." In: *Icarus* 220.1 (2012), pp. 225–253. DOI: 10.1016/j.icarus.2012.05.001.

[96] J. W. Warwick et al. "Voyager 1 Planetary Radio Astronomy Observations Near Jupiter." In: *Science* 204.4396 (1979), p. 995998. ISSN: 1095-9203. DOI: 10.1126/science.204.4396.995.

[97] Oliver L. White, Paul M. Schenk, Francis Nimmo, and Trudi Hoogenboom. "A new stereo topographic map of Io: Implications for geology from global to local scales." In: *Journal of Geophysical Research: Planets* 119.6 (2014), p. 12761301. ISSN: 2169-9100. DOI: 10.1002/2013je004591.

[98] Dieter A. Wolf-Gladrow, F. M. Neubauer, and M. Lussem. "Io's interaction with the plasma torus: A self consistent model." In: *Journal of Geophysical Research: Space Physics* 92.A9 (1987), p. 99499961. ISSN: 0148-0227. DOI: 10.1029/ja092ia09p09949.

[99] M Wong and William H. Smyth. "Model Calculations for Io's Atmosphere at Eastern and Western Elongations." In: *Icarus* 146.1 (2000), p. 6074. ISSN: 0019-1035. DOI: 10.1006/icar.2000.6362.

[100] Mau C. Wong and Robert E. Johnson. "The Effect of Plasma Heating on Sublimation-Driven Flow in Io's Atmosphere." In: *Icarus* 115.1 (1995), p. 109118. ISSN: 0019-1035. DOI: 10.1006/icar.1995.1082.

[101] Mau C. Wong and Robert E. Johnson. "A three dimensional azimuthally symmetric model atmosphere for Io: 1. Photochemistry and the accumulation of a nightside atmosphere." In: *Journal of Geophysical Research: Planets* 101.E10 (1996), p. 2324323254. ISSN: 0148-0227. DOI: 10.1029/96je02510.

[102] J.-S. Wu and Y.-Y. Lian. "Parallel three-dimensional direct simulation Monte Carlo method and its applications." In: *Computers & Fluids* 32.8 (2003), p. 11331160. ISSN: 0045-7930. DOI: 10.1016/s0045-7930(02)00083-x.

[103] J.-S. Wu and K.-C. Tseng. "Parallel DSMC method using dynamic domain decomposition." In: *International Journal for Numerical Methods in Engineering* 63.1 (2005), p. 3776. ISSN: 1097-0207. DOI: 10.1002/nme.1232.

[104] Jong-Shinn Wu, Kun-Chang Tseng, and Fu-Yuan Wu. "Parallel three-dimensional DSMC method using mesh refinement and variable time-step scheme." In: *Computer Physics Communications* 162.3 (2004), p. 166187. ISSN: 0010-4655. DOI: 10.1016/j.cpc.2004.07.004.

[105]   J. Zhang, D. B. Goldstein, P. L. Varghese, N. E. Gimelshein, S. F. Gimelshein, and D. A. Levin. "Simulation of gas dynamics and radiation in volcanic plumes on Io." In: *Icarus* 163.1 (2003), pp. 182–197. DOI: `10.1016/S0019-1035(03)00050-2`.

[106]   J. Zhang, D.B. Goldstein, P.L. Varghese, L. Trafton, C. Moore, and K. Miki. "Numerical modeling of ionian volcanic plumes with entrained particulates." In: *Icarus* 172.2 (2004), pp. 479 –502. ISSN: 0019-1035. DOI: `10.1016/j.icarus.2004.06.016`.

DECLARATION

on the basis of Article 18 of the PromR Phil.-nat. 2019

Name/First Name:	Klaiber, Lea Meera
Registration Number:	$19 - 131 - 077$
Study program:	PhD Physics with special qualification in Astronomy Dissertation
Title of the thesis:	Three dimensional DSMC modelling of the dynamics of Io's atmosphere.
Supervisor:	Prof. Dr. Nicolas Thomas

I declare herewith that this thesis is my own work and that I have not used any sources other than those stated. I have indicated the adoption of quotations as well as thoughts taken from other authors as such in the thesis. I am aware that the Senate pursuant to Article 36 paragraph 1 letter r of the University Act of September 5th, 1996 and Article 69 of the University Statute of June 7th, 2011 is authorized to revoke the doctoral degree awarded on the basis of this thesis. For the purposes of evaluation and verification of compliance with the declaration of originality and the regulations governing plagiarism, I hereby grant the University of Bern the right to process my personal data and to perform the acts of use this requires, in particular, to reproduce the written thesis and to store it permanently in a database, and to use said database, or to make said database available, to enable comparison with theses submitted by others.

Bern, Switzerland, 27.02.2024

Lea Meera Klaiber